Investigation of Acoustic Softening and its Application in Ultrasonic Assisted Incremental Sheet Forming

by

Randy Cheng

A dissertation submitted in partial fulfillment
of the requirements for the degree of
Doctor of Philosophy
(Material Science and Engineering)
in the University of Michigan
2023

Doctoral Committee:

Professor Alan Taub, Chair
Professor John Allison
Professor Mihaela Banu
Professor Ashwin Shahani

Randy Cheng

randyjfc@umich.edu

ORCID iD: 0000-0002-2473-8611

Acknowledgements

As I write this, I feel an immense level of appreciation for all the people I've met through grad school. They say your 5 closest friends shape who you are as an individual, but I'm blessed to say I had a whole cohort to make an impact on my personal growth.

I must start by acknowledging my advisor, Prof. Alan Taub. I am beyond appreciative for the mentorship you have given me through graduate school. If I'm honest, I struggled at the beginning on how to handle the professional relationship between an advisor and student. But through our many meetings, brainstorming sessions, discussions about career and upbringing, it was easy to see that you were invested in the growth of your students. Your encouragement, enthusiasm, and patience were inspiring and invaluable to my experience in your group.

I would also like to thank my committee members – Professors John Allison, Michaela Banu, and Ashwin Shahani for their support, direction and valuable critique of my dissertation work. I'm grateful to Dr. Tracey Berman, Dr. Qianying Shi, for training, troubleshooting software, and recommendations for sample preparation.

Shout out to the University of Michigan Incremental Sheet Forming team. Special thanks to Prof Banu for your helpful insight and efforts to introduce us to the forming community. Jaekwang Shin, Ankush Bansal, and Maya Nath are some of the best people I've worked with and I am grateful for their advice. Special thanks to Ankush for being a colleague and a friend. There were many times when I needed a second opinion, expertise, or … just raw human strength because those dies were heavy, you were always open to lending an ear/hand.

In addition, I wish to thank our collaborators: Prof Xun Liu and Dr. Jiarui Kang for their extensive work on ultrasonic assisted tension and recommendations on experiments; Brian Martinek and Scott Rose for resources used in this research; Matt Short and Nicholas Wiley for teaching me about the ultrasonic device, its operations, and installment; Prof Jian Cao, Dr. Newell Moser, Dr. Dohyun Leem for the collaborative discussion during the LIFT project. I would like to thank Bobby Kerns for the expertise in microscopy characterization; Prof Bogdan Epureanu for access to your lab; Kent Pruss for your machine skills and training.

The UM materials science department wouldn't be the quality that is without the excellent staff. Thank you, Ellen Kampf, for all your help in coordinating events and all the MSE administration staff: Shelley Fellers, Debra Johnson, Patti Vogel, and Renee Hilgendorf for advising, reimbursement, and procurement. Keith McIntyre, I hope you enjoyed all the odd proposals and challenges I brought to you; I appreciated all your help with lab related topics. To Sahar Farjami and Tim Chambers, thank you for patience every time I asked to get retrained after FOM discontinuous my access.

What drew me in to the Taub group was the amazing people. I cannot express how your individual personalities, openness, and sense of humor has made this journey better. Thanks mates – Dr. Avi Bregman, Dr. Maya Nath, Dr. Wesley Chapkin, Dr. Yipeng He, Dr. Aaron Gladstein, Dr. Anshul Singhal, Dr. Daney Zhang, Kanat Anurakparadorn, Anita Luong, Amy Langhorst, Xingkang She, Jon Goettch, Jiame Coronado, Louise Batta.

Shout out to the MSE 2017 cohort. What a unique set of individuals. I would've never expected that I would bond with a group of friends so closely and especially throughout the entirety of grad school. To Duncan Greeley, Dr. Aaron Gladstein, and Kyle Bushick I couldn't have had any better roommates. To Dr. Juliana Mesa, I am so grateful to have meet you in graduate school. We shared many moments where graduate school felt overwhelming, and work was extremely frustrating. When things got tough, your encouragement and positivity helped me pull through and return my view towards a wider perspective. I look forward to our chapter after graduate school. To my family – Jiayu, Ket, Landyn, Shirley, Jimmy and the little ones Mia and Enzo Korphosy- thank you for all the support, understanding, and pure joy. Our calls through face time always brighten me up.

Finally, I gratefully acknowledge the financial support from LIFT (Lightweight Innovations For Tomorrow) [DOD-ONR N00014-14-20002- LIFT 0007A-4], the National Science Foundation (EAGER award # 1841755 and CMMI # 2018963), and the University of Michigan College of Engineering.

Table of Contents

List of Tables

List of Figures

List of Acronyms and Symbols

AA	Aluminum Alloy
AL	Aluminum
CNC	Computer numerically controlled
DSIF	Double sided incremental forming
EBSD	Electron backscatter diffraction
ECCI	Electron channeling contrast imaging
EWI	Edison Welding Institute
FEA	Finite element analysis
GND	Geometrically necessary dislocations
ND	Normal direction
RD	Rolling direction
RMS	Root mean squared
Sa	Arithmetic roughness
SEM	Scanning electron microscope
SF	Squeeze factor
SF_e	Effective squeeze factor
SF_p	Programmed squeeze factor
Sku	Kurtosis
Sp	Peak Roughness
Sq	Root mean squared roughness
SSD	Statistically stored dislocations
Ssk	Skewness
Sv	Valley roughness
Sz	Peak-valley roughness
TD	Transverse direction
TEM	Transmission electron microscopy
UA	Ultrasonic assisted
UAC	Ultrasonic assisted compression
UAI	Ultrasonic assisted indentation
UA-ISF	Ultrasonic assisted incremental forming
UA-SPIF	Ultrasonic assisted single point incremental forming
UAT	Ultrasonic assisted tension
UA-TPIF	Ultrasonic assisted two-point incremental forming
UM	University of Michigan

Abstract

Agile manufacturing processes are in demand across a variety of sectors and applications. The ability to go from design to prototype to full production in a shorter amount of time and at lower cost represents the goal manufacturing companies set every year. Incremental sheet forming (ISF) is a process that has the potential to satisfy those needs. The process directs a rounded tool along a tool path in the shape of the desired geometry. Through the motion of this tool against the sheet metal, the sheet is deformed in iterative steps until the full geometry is created. There are multiple configurations of ISF; single-point ISF (SPIF) is die-less configuration where the sheet is free-hanging and has no additional support besides the clamps at the periphery. Two-point ISF (TPIF) utilizes a half-die to support the sheet and prevent undesired bending away from the tool contact area. Challenges to ISF include low surface quality from contact mechanics, low machine stiffness resulting in geometric deviations, and stored residual stress created by the bending.

This thesis investigates a variant of ISF that incorporates ultrasonic vibrations to the tool. This ultrasonic-assisted ISF (UA-ISF) process seeks to optimize on two known effects of the vibration. One is reduced friction at the tool sheet interface. The second is flow stress reduction, called acoustic softening, in vibration assisted processes. Truncated cone geometries were produced using UA-SPIF and UA-TPIF on CP aluminum, AA2024-O and AA7075-O. Due to the free hanging nature of the sheet in SPIF, minimal reductions in forming force, up to 5%, was observed and the fracture limit of the variable-angle, funnel geometry was unaffected. Sheet vibrations were minimized when incorporating the support die in UA-TPIF leading to a 27%

reduction in axial forming force with an amplitude of 6μm. The thickness reduction was much greater than the amplitude and supports the theory of acoustic softening. Surface characteristics were improved given the right process parameters. Parametric analysis showed the softening effect was most sensitive to the tool diameter and step size.

In comparison to UA-compression (UAC) tests in literature, UA-ISF has a much lower softening magnitude; the deformation state and contact mechanics are hypothesized to limit the softening magnitude. To gain a better understanding of softening effects, UA compression (UAC) tests were conducted on a variety of sample geometries. From an energy-based perspective, smaller sample volumes exhibited greater effects, up to 67% softening. The relative strain, called amplitude strain, was found to be a better parameter to represent the softening response across different sample dimensions and explains the wide variability reported in literature. In addition, the softening was found to diminish relative to the state of strain of the sample; therefore, it's a function of amplitude strain and sample strain history. The microstructure shows greater subgrain formation and broadening in texture intensity. The reduction in flow stress is hypothesized to be a combination of dislocation consolidation through subgrain formation and dislocation annihilation.

UA-indentation tests were selected to mimic the contact mechanics found in ISF and isolate the deformation mode. The average softening was found to be similar to UA-TPIF results. FE simulations modeled the indentation deformation. Provided with the plastic strain distribution, an effective softening value was calculated. This brought the simulated force closer to experimental observation but further ultrasonic testing on shear-based deformation is recommended.

CHAPTER 1
Introduction

1.1 Motivation

Agile manufacturing processes are in demand across a variety of sectors and applications. The ability to go from design to prototype to full production in a shorter amount of time and at lower cost represents the goal manufacturing companies set every year [1-4]. Especially given the recent events with global supply chains, accessibility and on demand production are heavily valued. Incremental sheet forming (ISF) is a process that has the potential to satisfy those needs. The process directs a rounded tool along a tool path, in the shape of the desired geometry. Through the motion of this tool against the sheet metal, the sheet is deformed in iterative steps until the full geometry is created. The iterative forming increases the time to produce a single part compared to stamping, so ISF is more suitable for low volume production, customized parts, or prototyping. While there is a tradeoff in production volume, ISF provides a significant benefit in capital resources from the flexibility in the forming machine and its configurations. ISF has been demonstrated on CNCs, lathes, and robotic arms; non dedicated machines widen the field of available suppliers. Two configurations of ISF are discussed in this thesis. Single-point ISF (SPIF) is a die-less configuration where the sheet is free-hanging and has no additional support besides the clamps at the periphery. Two-point ISF (TPIF) utilizes a half-die to support the sheet and prevent undesired bending away from the tool contact area [1-4]. The hardness of the support die can be made from lower hardness materials compared to stamping dies which are required to resist high forces [5].

Although a promising technology, several challenges remain. The surface roughness of incrementally formed parts are worse than stamped sheet used for automotive and aerospace applications [6-15]. Automotive grade surfaces are required for formed parts to transition to have desired painted surface quality [5]. In addition to cometic requirements, higher surface roughness increases the probability of crack initiation at the surface, compromising the fatigue life. The deformation in ISF is a combination of bending, stretching and shearing [16-21]. Depending on the configuration and parameters, the deformation can promote a strain gradient through the sheet thickness which manifests into stored residual stresses and springback [22-23]. In addition to springback, the compliance of the tool and machine can lead to geometric deviations that are not dependent on the deformation [24]. ISF using robotic arms are attributed to higher compliance because sheet metal forming was not the initial intended purpose and as such, tool path correction strategies are required [25]. Finally, the formability of low ductility materials, such as magnesium and titanium, require heating of the sheet via joule heating, frictional heating, or synchronize laser heating to hot forming temperatures [26-27].

There are a variety of pathways to address these challenges; A recent introduction of ultrasonic assisted ISF displayed promise [28-30]. The researchers incorporated a vibrating tool in incremental forming of a simple groove shape geometry. They noted several observations: lower surface roughness, less springback, reduced forming force, and an increase in formability. The field of ultrasonic assisted (UA) deformation has gain traction recently, focusing on two unique benefits: softening of the material during deformation [31-44] and reduction of frictional forces [45-54]. The use of vibrations in manufacturing has been demonstrated in extrusion, deep drawing, burnishing, tube-spinning; however, the implementation of UA in incremental forming of full scale, benchmarking parts have yet to be demonstrated. Furthermore, understanding of the

ultrasonic softening (also called acoustoplasticity), its mechanisms and the resulting change in material properties is still in its infancy. Consequently, the primary goals of this research is to demonstrate the application of UA in ISF and the expected outcome of formed parts, and explore the material behavior in ultrasonic assisted compression (UAC).

1.2 Overview of dissertation

This dissertation is organized in to four main chapters. Chapter 2 exapands on the ISF background. The chapter presents an overview of ISF including the setup configurations, advantages/disadvantages to each, and a summary of challenges and proposed solutions. The chapter also discusses the ultrasonic softening and friction related phenomenon; discrepancies and areas requiring further investigation are highlighted. A schematic and description of the ultrasonic device used in this dissertation is also presented.

In Chapter 3, ultrasonic assisted ISF is demonstrated by forming benchmark conical geometries of different wall angles. The chapter presents both SPIF and TPIF configurations with added vibrations. The results suggest UA-TPIF is more suitable to benefit from the softening and changes in friction. Part outcomes were quantified, and a parametric analysis was conducted to identify the correlation to the softening magnitude. The difference in the observed softening for ISF is compared to literature. Microstructural analysis comparing ISF parts with and without UA concludes the chapter.

Chapter 4 is a more fundamental investigation of the ultrasonic softening effect through ultrasonic-assisted compression (UAC) of aluminum alloys 2024-O and 7075-O. Ultrasonic softening discrepancies from literature are highlighted. Common acoustic softening terms were evaluated through a series of compression experiments and a new parameter, amplitude strain, was proposed to better represent the behavior of specimens under ultrasonic excitation. The results of

the chapter highlight the necessity of reporting specimen dimension, amplitude, and the state of strain of the sample.

UA indentation experiments were conducted in Chapter 5. The kinematic aspects of ISF were removed by introducing the quasi-static deformation in indentation. The change in ultrasonic softening behavior between UA compression, indentation, and ISF were attributed to modes of deformation and a distributed amplitude strain hypothesis. The proposed hypothesis was evaluated based on a FE simulation of the indentation strain gradient.

The conclusions of this dissertation are summarized in Chapter 6 and recommendations for future work are outlined.

CHAPTER 2
Background

2.1 Introduction to Incremental sheet forming

Incremental sheet forming (ISF) is an agile manufacturing technology that produces 3D geometries without dedicated tooling. A sheet is clamped between two binders, as shown in **Figure 2-1** [2], and a hemispherical tool travels along a predefined path that resembles the geometry of choice. Through this process, the tool deforms the sheet in small increments until the final geometry is completed. The two constants in this manufacturing process are the binder to fix the sheet and the tool. The machine of choice and setup are entirely flexible and has been demonstrated in computer numerically controlled (CNC) machines, lathes, and robotic arms. The value proposition for ISF technology is its capital efficiency in low volume production, potential for aftermarket accessibility, and fast turnaround periods for prototyping. Some specific applications include aerospace parts, customized prosthetics, and prototype & aftermarket automotive sheets.

There are multiple configurations of ISF which were iterated to address certain shortcomings of each configuration. Single-point ISF (SPIF), Two-point ISF (TPIF) and Double-sided ISF (DSIF) are schematically shown in **Figure 2-1**. SPIF is the most flexible configuration as the processes does not require any support from the bottom of the sheet as shown in **Figure 2-1a**. The lead time is shortened significantly as adjustments to dies and tooling are not required. However, part accuracy in SPIF is inferior to the other configurations and some complex geometries with convex type features and features near the center of the sheet cannot be formed

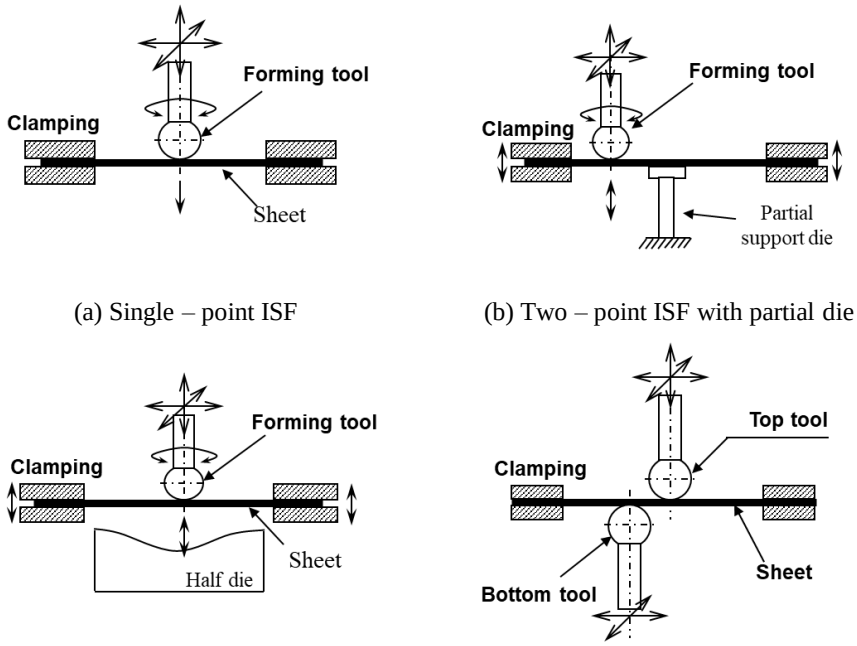

(a) Single – point ISF

(b) Two – point ISF with partial die

(c) Two – point ISF with half die

(d) Double – sided ISF

Figure 2-1 Schematic of incremental sheet metal forming process (Cao et al. [1], Reddy et al. [2])

using SPIF. The undesired bending near the binder-sheet interface, which is occurs just beyond the tool contact area, leads to geometric inaccuracy greater than comparable stamping geometries.

In addition, the surface quality of ISF parts is of great importance if the final application falls into aerospace and automotive vehicles. The tool-sheet interface, which is referred to as the tool contact side, has abrasive and adhesive wear from the tool-sheet interaction. The non-contact side does not suffer from tribological wear however, an orange peel defect has been observed in incremental forming of commercially pure (CP) aluminum, AA2024-O, and AA7075-O. Orange peel is a cosmetic defect where the surface grains of the sheet deform heterogenous based on their slip orientations, which leads to a speckled like pattern shown in **Figure 2-2** [24]. The severity of the orange peel defect can be mitigated through grain size control but using the TPIF & DSIF configurations can also prevent orange peel by pressing the sheet against the die surface. The TPIF configuration utilizes a partial or a half – die present underneath the sheet for local support as

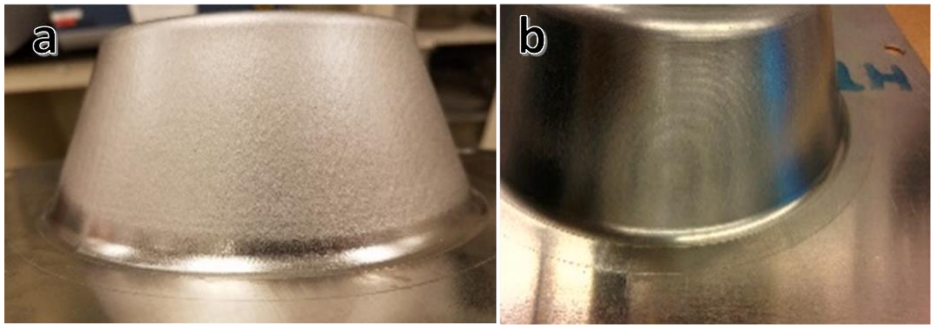

Figure 2-2 7075O alloy formed via SPIF. a) Orange Peel cosmetic defect present. b) Formed with positive squeeze factor. No orange peel defect present. [24]

shown in **Figure 2-1b & c**. The support die significantly reduces unwanted bending. However, it also makes the process less flexible since the partial die can be considered dedicated tool depending on its geometry. Nonetheless, the TPIF configuration still has advantages. The partial die can be designed with a lower hardness material because the deformation is localized around the tool contact area and therefore, the forces are much lower. The sheet can also be pressed against the die surface, **Figure 2-1c**, which is referred to as programmed squeeze, and this effectively changes the through thickness strain distribution to alleviate spring back and prevent the orange peel defect [24]. ISF configuration **Figure 2-1b** also introduces meridional stresses that has proven to reduce the spring back compared to SPIF [55]. From these three configurations of ISF, the DSIF setup requires the most complicated machinery because it requires an additional 3-axis tool, **Figure 2-1d**, but DSIF provides the greatest flexibility out of the three. In the following chapters, SPIF and TPIF configurations are studied in detail.

The process planning for ISF starts with obtaining the part geometry by scanning an existing part/die surface or designing the geometry in a CAD software. Once the surface is created, it can later be segmented into slices and converted into machine readable G-Code. Another method is to create the tool path numerically through a software package like Matlab or Python. Through this route, there are several tool path parameters, as shown in **Figure 2-3** available for modification.

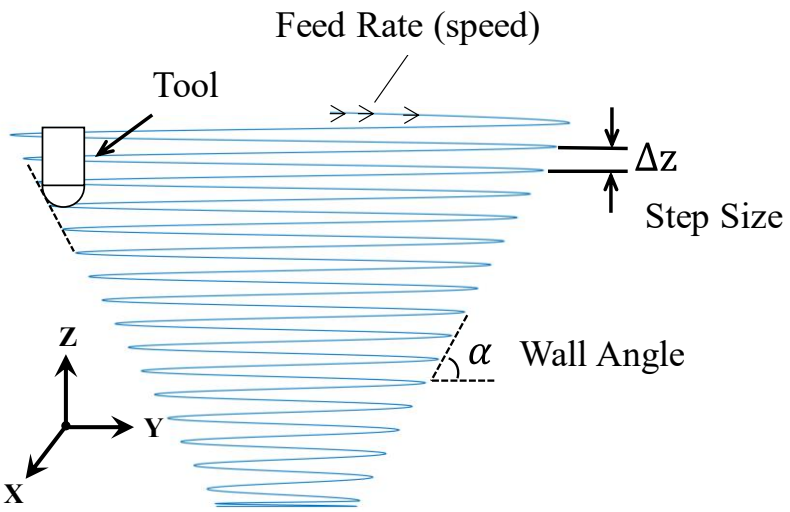

Figure 2-3 Tool path parameters: tool diameter (t_D, mm), feed rate (F, inch/min), step size (Δz, mm), and wall angle (α, degrees).

ISF has several controlled process variables as described below:

(1) The wall angle, α, can vary depending on the desired geometry. Since the sheet is fixed in place, the material is prevented from flowing into the geometry as would be the case for stamping where the binder force is controlled to allow sheet slippage. This limits the maximum angle at which a part can be formed in a single pass. Multipass tool paths have demonstrated the ability to form near 90-degree wall angles equivalent to cup drawing [56]. The final thickness of the formed part can be approximated using the sine law:

$$t_f = t_0 * \sin\left(\frac{\pi}{2} - \alpha\right) \quad (2.1)$$

where t_0 is the initial thickness, t_f is the thickness after forming, and α is the wall angle. The sine law is a simple geometric representation of the deformation where volume is conserved [4,57]. Nath [58] demonstrated the validity of the sine law even when forming funnel geometries where the wall angle progressively increases.

(2) The step size (Δz) parameter represents the plunge of the tool along the Z axis as the tool completes one full revolution of the previous segment as shown in **Figure 2-3**. Depending on

the step size selected, the overlap with the previous pass can contribute to significant strain hardening. If the step size is too small, the material can exhibit chipping without through thickness fracture.

(3) Feed rate (F) is the speed at which the tool travels along the tool path and spindle speed (S) represents the revolutions per minute of the tool.

(4) Squeeze factor, SF, is a parameter unique to the TPIF and DSIF configurations. The presence of the partial die or tool acting as a support allows for squeezing of the sheet between the two surfaces.

SF in TPIF is defined as the distance between the tool contact point and die surface (d) divided by the local formed sheet thickness (t_f). The programmed values of squeeze factor, SF_p, is determined during the tool path processes phase while the effective squeeze factor, SF_{eff}, is calculated based on the measured forces or sheet thickness. The ISF team at University of Michigan demonstrated

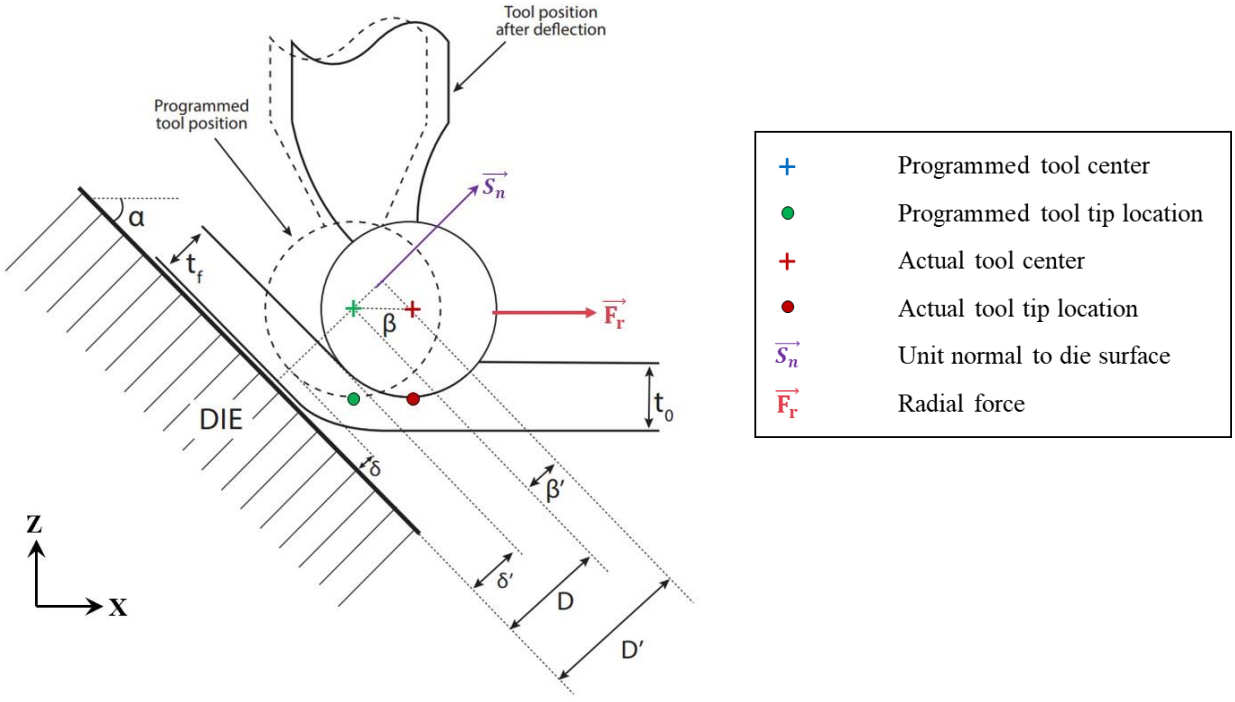

Figure 2-4 Cross-sectional schematic of TPIF part forming process to calculate effective material squeeze factor based on its programmed value [24]

the significant difference between these two variables by considering the compliance coming from both the stiffness of the CNC machine and the bending of the forming tool [59]. As illustrated in **Figure 2-4** [24], the tool experiences a radial force, $\overrightarrow{F_r}$, that caused the tool to deviate from the desired location. The distance between the desired tool contact position and die surface, δ, is now larger, δ'. The nomenclatures used in the **Figure 2-4** for the programmed vs. effective squeeze factor calculations are assumed as below [24]:

- β is the distance between actual and programmed tool center
- β' is the projected β distance along the unit normal $\overrightarrow{S_n}$
- D is the programmed distance between tool and die surface along the unit normal $\overrightarrow{S_n}$
- D' is the actual distance between tool and die surface along the unit normal $\overrightarrow{S_n}$
- δ is the minimum programmed distance between tool and die surface

A step-by-step procedure for determining the effective squeeze using the measured forming force can be found in [24]. In short, the coupled compliance of the tool deflection and machine stiffness is required to approximate the effective squeeze, or it can be measured by taking the final thickness of the formed part, assuming that spring back in the through thickness vector is small relative to the final thickness. When a positive effective squeeze condition is reached, the forming force in TPIF, for the equivalent geometry in SPIF, will be greater and the orange peel defect will no longer be present as shown in **Figure 2-2**. Going forward, the TPIF results presented in this dissertation have been verified as showing positive squeeze.

A brief note on the formability aspects of ISF. Formability characterization in stamping is conducted through series of tensile and bulge test forming where circular grids are measure prior and post forming to obtain the forming limit curve (FLC). The FLC is a major and minor strain

space that represents the strain path (plane strain, biaxial, shear, etc) and limits of a given material. Filice et al. [60] measured the major-minor strains in a variety of SPIF tests and found the strain path to be considerably different than traditional characterization tests. Emmens and van den Boogaard [21] performed a comprehensive analysis on failure mechanism and remarked the through-thickness shearing and cyclic strain hardening are potential reasons for the higher material formability. After combining similar studies [17,19,21], a consensus is formed that traditional FLC is incapable of describing failure in any ISF process and it must be replaced by fracture forming limit (FFL) diagrams. The fracture forming limit has a much higher forming limit than FLC; SPIF of 67° axis symmetric cones reach through thickness strains of 60% in aluminum alloys, much greater than the ductility expected in tensile deformation [61].

2.1.1 Areas of Continued Research in Incremental Sheet Forming

The advantages of ISF presents a novel manufacturing technique that can satisfy a variety of manufacturing products and industries. However, challenges surrounding surface finish, residual stress and compliance requires continued investigation.

Surface finish investigations throughout the literature often modify one or multiple processing parameters and record the resulting surface finish characteristics. Radu et al. [62] performed a sensitivity study and observed the step size parameter, Δz, has a more significant effect on surface finish. Echrif et al. [6] performed ANOVA analysis and found the combination of a larger tool diameter and smaller step size to provide the best surface finish. Using a smaller step size minimizes the wavy features, called scallops, that is created when the tool locally deforms the sheet. It is important to note that decreasing the step size can lead to significant strain hardening and result in chipping of the sheet surface [24]; Therefore, the optimal tool diameter and step size has a local maxima/minimum for the best results. The selectivity of lubricants also plays a critical

role in the final surface finish [7-15]. Azevedo et al. [7] demonstrated how changes in lubricant viscosity impact the surface finish of ISF parts. Lower viscosity lubricants were appropriate for hard materials such as DP 780 steel, whereas high viscosity lubricants provided better surface finish in soft materials like aluminum. Based on our previous work, a moly-sulfide grease (MoS2) was found to be the optimal lubricant of choice for incremental forming of aluminum alloys and was the used for the experiments presented in this dissertation.

Residual stress and geometric accuracy are often associated with one another when considering the outcome of formed sheet products. The geometries and methods of sheet forming can create through thickness strains that are inhomogeneous and therefore creates a distribution of stored residual stress. Specifically, the SPIF configuration creates high tensile strains on the outer, non-contact surface of the sheet during forming [22,62]. Cutting the sheet post-forming shows a 'negative' spring back moment as shown in **Figure 2-5** Residual stress relief of CP titanium formed into a pyramid geometry [26]. Tanaka et al. [22] demonstrated a method to prevent the inhomogeneous distribution of strain using the secondary tool, in DSIF configuration, as a support and thus, alleviated the severity of spring back. Other strategies such as varying the tool diameter, step size, increasing the spindle rotation speed to create frictional heating [62], and applying a tensile stress on the blank during forming [63] can assist in minimizing residual bending stresses.

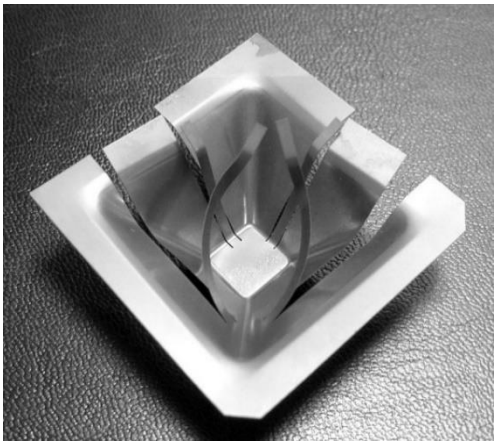

Figure 2-5 Residual stress relief of CP titanium formed into a pyramid geometry [26]

Most sheets that are formed are in O-temper or annealed conditions and require additional heat treatment to bring forth the strength benefits from precipitation hardening. A high storage of residual stress can cause additional deformation during the precipitation heat treatment process if the sheet is clamped and minor geometric deviations if the sheet is free.

Non dedicated machinery allows for flexible and agile manufacturing in ISF. However, the absence of highly stiff machines and excessive tool bending (compliance issues) result in geometric deviation. Bansal et al. [59] showed that TPIF and DSIF experiments were incorrectly labeling their squeeze conditions because of the machine compliances that were not considered. This is exacerbated when forming high strength materials like steels and titanium alloys. Proposed solutions from literature includes compliance corrected tool path (pre-forming) [24], camera aided feedback loop for real time collection of geometric information [25], and laser heating of sheet to lower the forming force and residual stress [26].

2.2 Ultrasonic Metal Forming

Ultrasonic metal forming consists of high frequency, greater than 20kHz, vibrations applied to a variety of forming processes: drawing [45], tube bending [46], punching [33], equal channel angular pressing [64], and incremental forming [28]. The purpose of adding ultrasonic vibrations to a process is to achieve increased production speeds, less tool wear, reduced forming forces, and better surface finish. The beneficial outcomes of adding ultrasonic vibrations are often separated into 1) frictional effects and 2) bulk or plasticity effects. This section reflects on the contributions in literature on these two topic areas.

2.2.1 Ultrasonic Friction Reduction

One of the simplest experimental setups to represent friction conditions against two surfaces is a sliding test as shown in **Figure 2-6**. A normal force is applied on the block and the block is pulled across the surface of the plate. In this diagram, the ultrasonic vibrations can be applied in the three orthogonal directions: normal to the plate surface, transverse to the pulled direction, and longitudinal (parallel) to the pull direction. Littmann et al. [48] applied the vibrations parallel to the pulling direction. They measured force reductions up to 70% and found that friction reduction decreases as the pulling velocity increases. Kumar and Hutchings [49] studied the difference in parallel and perpendicular vibrations relative to the pull direction and found parallel vibrations are more effective in reducing frictional forces. Teidelt et al. [50] observed a 60% reduction in friction force when the vibration was applied normal to the sliding plane; they concluded that the amplitude influences the static friction the most in this vibration configuration. Dong et al. [39] also replicated this pin on disk experiment using vibrations parallel to the pin axis or normal to the revolving disk; they expanded the angular velocity and amplitude window and observed an inverse and direct correlation, respectively, in the measured force reduction. Daud et al. [37] calibrated a finite element model using the experimentally measured stress-strain curves

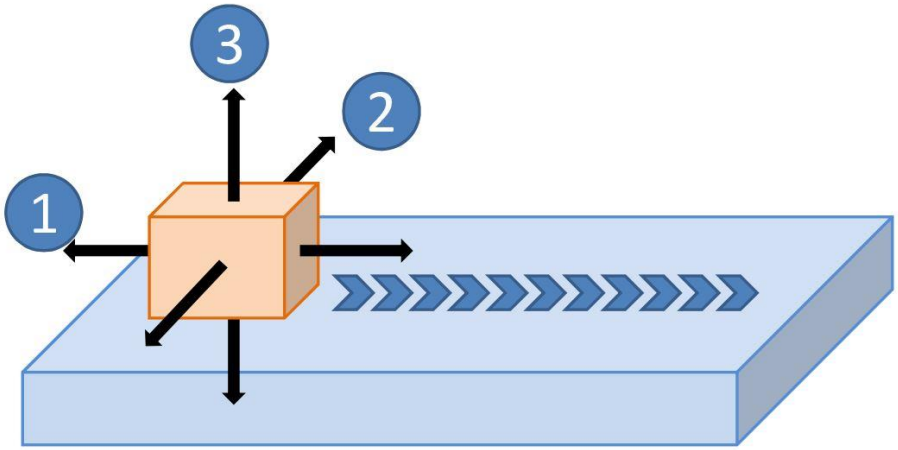

Figure 2-6 Different vibration directions 1) longitudinal or parallel to pull axis, 2) transverse 3) normal to slide plane. The pull direction is indicated by the stripped arrow proceeding from left to right. [48]

from ultrasonic assisted tensile and compression tests; their results suggest a real change in the coefficient of friction along with material softening which is discussed in the next section. These examples best represent the forthcoming work in this dissertation as the vibration motion will be normal to the sheet surface or tilted slightly to 45°-67° from the normal vector. In summary, extensive experimental research [53-54] have demonstrated how ultrasonic vibrations influences the coefficient of friction and the significance of the frictional force reduction depends on experimental conditions: ultrasonic amplitude, forming speed, contact pressure, viscosity of the lubricant, and vibration frequency. Utilizing ultrasonic friction reduction effects in ISF can serve to achieve optimal surface finish and minimize the susceptibility to early fatigue failure, a desired characteristic in automotive and aerospace industries.

2.2.2 Ultrasonic Softening (Acoustoplasticity Effect)

The acoustoplasticity effect (APE), or more commonly referred to as ultrasonic softening, was first observed by Blaha and Langenecker [65] during tensile testing of zinc single crystals. The material exhibited a large flow stress reduction in response to a minor vibration and the relative benefit in reduced work was calculated to be more efficient than joule heating. The proposed driving mechanism was a localization of acoustic energy at defect sites, such as dislocations, which lowers the critical energy required for slip. Others have argued that this effect instead driven by material heating or simply the retracement along the modulus during unloading, termed stress superposition, as shown in **Figure 2-7**. Since this initial finding, ultrasonic softening has been demonstrated in a variety of metals and their alloys including aluminum, copper, magnesium, titanium, and steel [40-41,52,66-67]. Multiple studies have reported that the increase in specimen temperatures is well below the requirement for hot forming [68] and that stress superposition

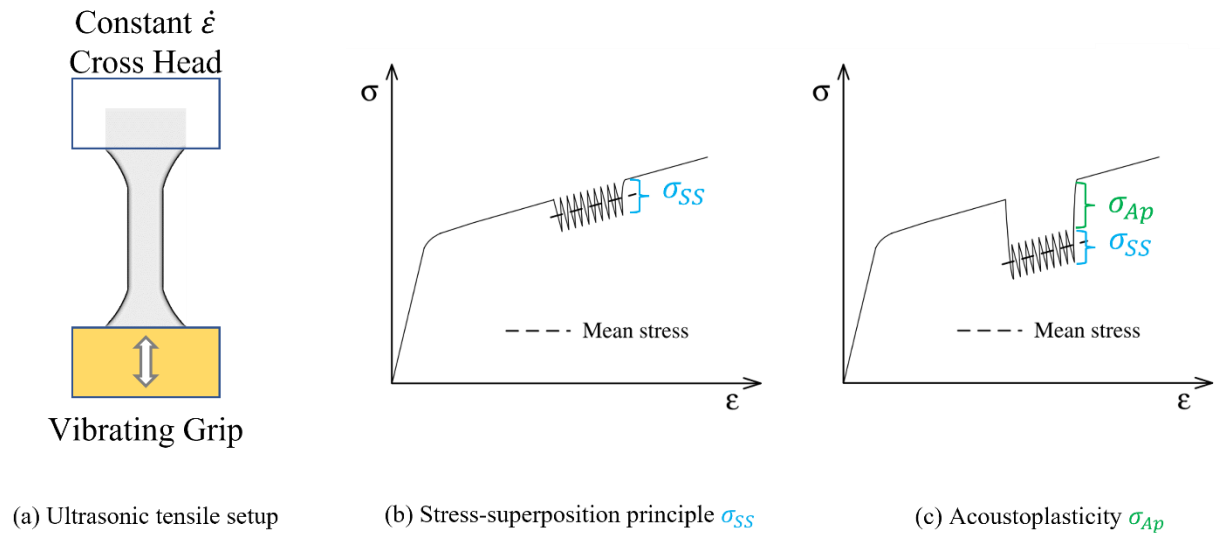

(a) Ultrasonic tensile setup (b) Stress-superposition principle σ_{SS} (c) Acoustoplasticity σ_{Ap}

Figure 2-7 Schematic representation of vibration excitation on tensile specimen(a); stress-superposition principle observed on a stress-strain curve (b); acoustoplastic phenomenon in stress-strain curve (c)

cannot fully account for the reduction in flow stress [38]. The ultrasonic vibration is often applied during the plastic regime for a short duration or for a finite amount of strain and the change in flow stress can be represented by:

$$\sigma_f = \frac{\sigma_{UA}}{\sigma_{Control}} \tag{2.2}$$

$$\Delta\sigma = \frac{\sigma_{Control} - \sigma_{UA}}{\sigma_{Control}} \cdot 100 \tag{2.3}$$

where the softening fraction, σ_f, is the ratio of the flow stress for the ultrasonic assisted (UA) sample divided by the flow stress of the quasi-static loaded or control sample. $\Delta\sigma$ is the softening magnitude which is the percent change in stress relative to the control sample. Acoustic variables such as acoustic energy density, intensity, and stress have been used to correlate $\Delta\sigma$ and are represented by these equations [66-69]:

$$E = \frac{\sigma_{acoustic}\,\omega\lambda}{c} = \rho\omega^2\lambda^2 \qquad \left[\frac{J}{m^3}\right] \tag{2.4}$$

$$I = \rho c\omega^2\lambda^2 \qquad \left[\frac{W}{m^2}\right] \tag{2.5}$$

$$\sigma_{acoustic} = \omega\lambda\sqrt{\rho E_{mod}} \qquad [MPa] \quad (2.6)$$

E, I, σ are the acoustic energy, intensity, and stress terms respectively. ρ is the density of the sample, ω is the angular frequency of the ultrasonic horn, λ is the applied amplitude, c is the maximum speed of sound in the sample, and E_{mod} is the elastic modulus. Acoustics are typically represented as a function of time and position in first principles. These equations are modified to represent the simple translation of a surface and its associate energy. The material sound velocity, density, and elastic modulus terms remain a constant. The frequency can fluctuate slightly when using piezo-ceramic driven transducers given the load; these transducers are design to operate within a specific frequency window such as 20kHz ± 1k. Alternatively, magneto-restrictive transducers can be set to different frequencies as the excitation is driven by a magnetic disk instead of piezoceramics. However, piezoceramic transducers are the material of choice due to their efficiency and their ability to maintain high amplitudes. Therefore, amplitude (λ) is the main variable for most of the experiments reported in literature. Acoustic stress is linearly proportional to λ while acoustic energy density and intensity are correlated to λ^2. There is no consensus for reporting acoustic energy, intensity or stress in the literature and results have been mixed. Deshphande et al. [39-40] performed ultrasonic assisted compression (UAC) on aluminum wire and found correlations to energy density. Wang et al. [69] observed a linear relationship to amplitude in ultrasonic assistance to tensile tests (UAT) of copper foils. Yao et al. [70] conducted UAC tests on commercially pure aluminum and reported a linear relationship between amplitude and flow stress.

In addition, the magnitude of softening reported for the same alloy can vary significantly. Several examples of UAC on commercially pure aluminum are taken from literature. Daud et al. [38] observed a softening effect of 38% when using an amplitude of 10μm. Zhou et al. [66]

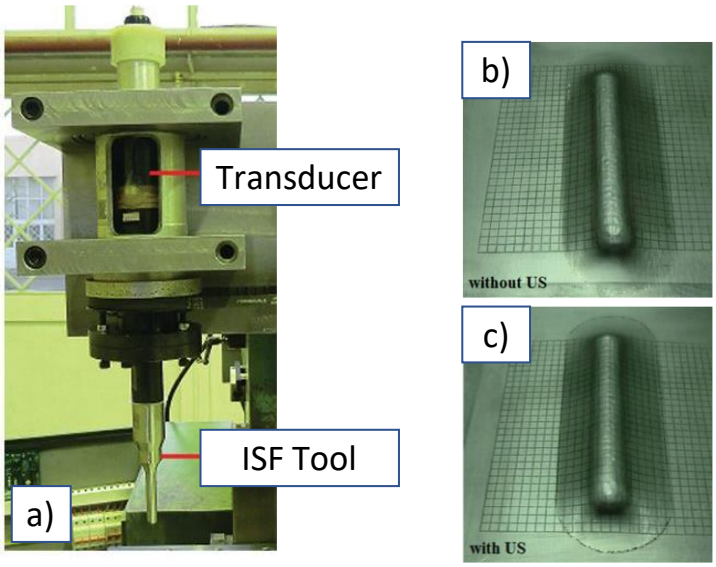

Figure 2-8 Ultrasonic ISF setup. a) ISF tool coupled to transducer stack on CNC machine, b) formed groove without vibrations and c) with vibrations. [34]

achieved 37% softening with just a 4µm amplitude. Yao et al. [70] found a softening effect of 35% with only a 2µm vibration amplitude. Possible reasons for these differences include variability in experimental setup and differences in material microstructure. Ahmadi et al. [64] conducted ultrasonic assisted equal channel angular press on commercially pure aluminum with grain sizes ranging from 109µm to 1µm and discovered a direct correlation between softening and grain size. Kang et al. [71] found that the sample texture has a direct relationship in differences of softening response when a copper tensile specimen is pulled parallel or perpendicular to the rolled direction.

APE has been tested on a variety of practical manufacturing techniques as mentioned in **Section 1.3.1** However, the use of ultrasonic vibrations in ISF has been limited. Vahdati et al. [28] included a vibrating tool in single point incremental forming of straight groves, **Figure 2-8**; the acoustic softening effect led to a lower forming force, greater strains and minimized the surface roughness. Li et al. [30] simulated a point forming process in LS-DYNA with superimposed vibrations on the tool. They concluded the change in forming force is proportional to the vibration amplitude. Sedaghat et al. [72] performed ultrasonic assisted ISF (UA-SPIF) on Aluminum 1050 with a vibration amplitude of 15µm; they observed a consistent 12.5% reduction. Further research

on the successful implementation of ultrasonic vibration in ISF to achieve optimal part outcomes is needed. This dissertation presents the first experimental implementation of ultrasonic assisted TPIF.

The methods for modeling ultrasonic softening are diverse. Ultrasonic softening has been phenomenologically modeled using Kock-Mecking empirical dislocation model [70], mixed thermal-crystal plasticity model [73], crystal plasticity model [71], John-Cook model [74], and a hybrid model [35]. When translating ultrasonic softening effect from compression/tension to a more complex deformation process, the softening effect is not a one-to-one direct correlation. An example can be taken from the work of Aziz and Lucas [75]; they demonstrated using ultrasonic vibrations in the press forming and showed a reduction of 22% with an applied amplitude of 20μm. Sedaghat et al. [72] modeled this upsetting process using Kocks-Mecking empirical model where they lowered the activation energy for dislocations to overcome barriers. However, they needed to introduce two fitting constants: effect coefficient and active volume parameter. The first coefficient accounts for the inefficient transfer of energy from the transducer to the workpiece and the latter adjusts the active volume of material participating in slip. These coefficients are determined through experimental fitting and are always less than 1, implying some loss in the ultrasonic softening phenomenon. These assumptions have yet to be confirmed through experimental design and testing.

2.2.3 Microstructure

The change in microstructure has been a key argument for the acoustoplasticity effect. Zhou et al. [66] performed a series of UAC on commercially pure aluminum and found a greater fraction of low-angle grain boundaries (LAGBs) and refinement of grains. Siu et al. added ultrasonic vibrations to a Vickers indentation test and reported sub-grain formation. Deshpande et

al. [40] compressed aluminum wire using UAC and observed an increase in grain size at high ultrasonic amplitudes; they attributed this finding to UA induced dynamic recovery.

The microstructure of other material systems has also demonstrated significant change. Dutta et al. [41] recorded lower GNDs in grain interiors and an absence of sub-grain formation in UAT of DC04 steel; they later found a bimodal distribution of grain sizes and suggested the mechanism to be UA induced grain rotation and dynamic recrystallization. Kang et al. [68] reported a reduction in the fraction of annealing twins in UAT of copper. Meng et al. [76] noted an initial increasing in LAGBs and then a reduction when the amplitude was increased from 1.66μm to 3.18μm in UAT of a thin Inconel 718.; they also measured a higher fraction of twin boundaries correlating to an increase in vibration amplitude.

The reports of ultrasonic assisted deformation have been generally in agreement for aluminum samples: greater formation of subgrain boundaries. The leading theory in the acoustoplasticity phenomenon is the reversed dislocation motion during the unloading portion of the vibration; Cheng et al. [34] proposed the reversed dislocation motion increases the attempt frequency of statistically stored dislocation (SSD) annihilation and the process may be further enhanced when cross slip occurs. The resulting microstructure would leave GNDs which accommodate local grain rotation and are observed via EBSD as local misorientations. The reduction in SSD density is observed as macro softening; load or displacement control experiments should result in greater strain and strain control experiments should measure lower flow stresses under this theory.

2.4 Ultrasonic transducer operation & amplitude measurement

An ultrasonic stack is the holistic term encompassing the integration of a traducer, horn, and sonotrode. One type of transducer is piezoceramic transducers (PZT) which converts electric energy into mechanical energy and is commonly referred to as the converter. The booster is an optional component, and it functions, as the name suggests, to increase the vibration amplitude. The sonotrode is the component that makes contact with the workpiece. The ultrasonic stack shown in **Figure 2-9** was acquired from the Edison Welding Institute (EWI) located in Columbus, Ohio, and is used for all the experiments shown in the dissertation. The intended purpose was for ultrasonic assisted drilling; however, with the help from Matt Short and Nicholas Wiley, this product was easily accommodated for UA-ISF. The schematic shown in **Figure 2-9b** illustrates the components which are similar to standard ultrasonic stacks. The piezoceramic disks is the converter; the taper around the spring collet focuses the acoustic energy like a booster; the tool functions as the sonotrode.

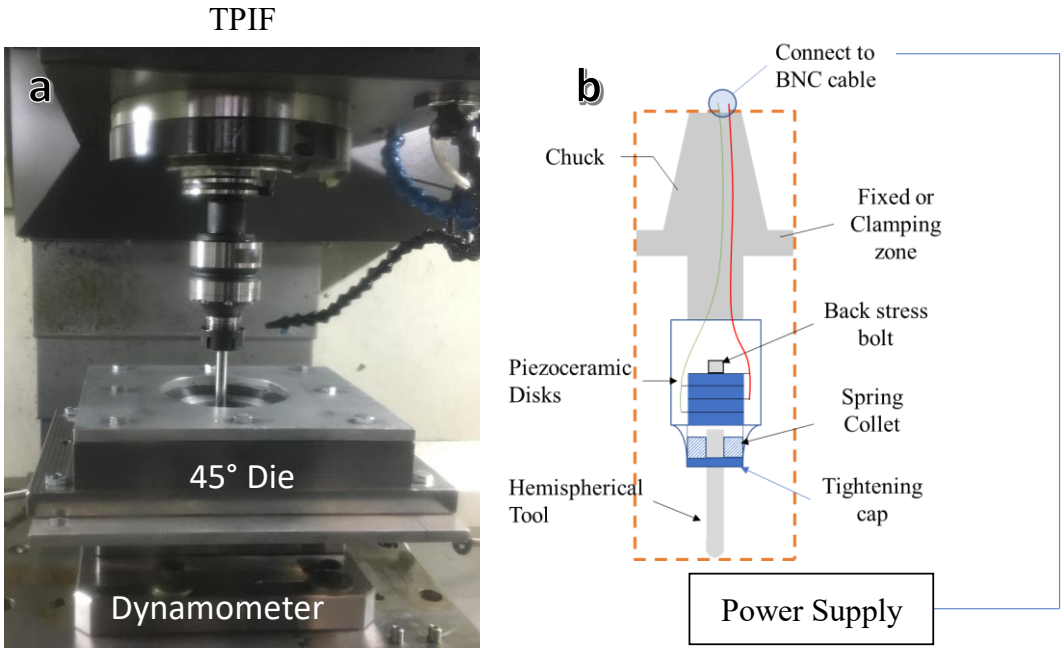

Figure 2-9 TPIF experimental setup with the ultrasonic transducer fitted in the chuck holder; b) schematic of transducer and its internals.

The tool fitting operates like any other CNC chuck. The tool is slid into the spring collet and the tightening cap is torqued down to apply a compressive force on the tool. The transducer was design to operate at 20kHz and requires a specific tool hanging length of roughly 127mm or 5 inches. The entirety of the tool is design to operate at a specific frequency and as such, the operating frequency cannot be easily change without redesigning the entire transducer. The ultrasonic transducer shown in **Figure 2-9** is powered by a commercial Dukane generator, model # 20VB480-2L. The internal control has a function for scanning the stack. During the scan process, the generator sweeps through the max operating range (19kHz-21kHz) and measures the current draw. At resonant frequency, the current and AC voltage input are in-phase, and the current draw is maximum. Loading the transducer will shorten the length of the horn and as such, the current and input frequency deviates from the initial resonant frequency. The programmed controller sweeps the frequency, in a short amount of time, and identifies the new operating frequency with the higher current draw.

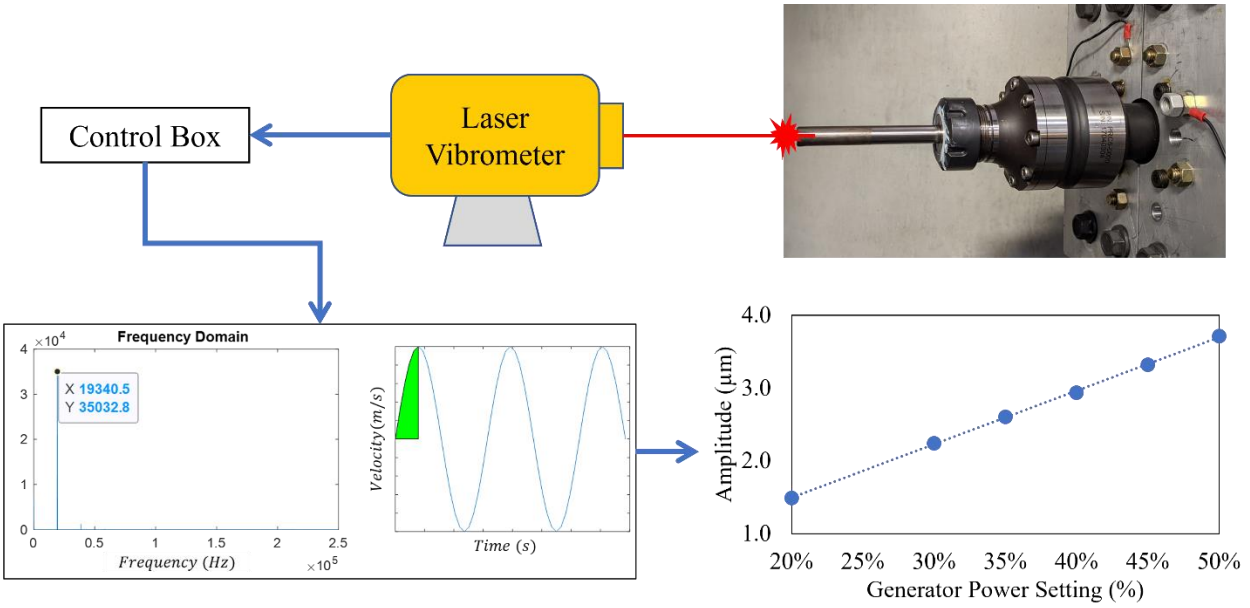

Figure 2-10 Amplitude measurement process flow chart

Here we'll show the process of measuring the amplitude and the amplitude under load. (**Note**: These setup images differ from **Figure 2-9** as the ultrasonic stack was later installed at the WU Center (UM) where the amplitude measurements were conducted). A laser vibrometer was used to measure the velocity as shown in **Figure 2-10**. The collected signal can be converted into the frequency domain to confirm the resonant frequency in real time. The tool amplitude was calculated by integrating velocity relative to time and the results showed a linear relationship between generator power input and vibration amplitude. In ISF, the tool used for forming experience orthogonal forces; the Z-axis force is along the length of the tool, **Figure 2-11a** while the resultant X&Y forces load perpendicular to the tool, **Figure 2-11b**. To measure the vibration amplitude under Z-axial load, a tapered hole was machined into a 0.375" plate and the tool was pressed against the taper at controlled force increments. The stack was subsequently flipped on to measure the vibration amplitude, **Figure 2-12**a. The amplitude is shown to increases at the lower load conditions and stabilized at the higher load conditions. The lower amplitude shift could be due to the plate-tool interactions where the controller identifies the plate as an effective extension of the ultrasonic stack. Ultimately, the necessary requirements are consistency between different

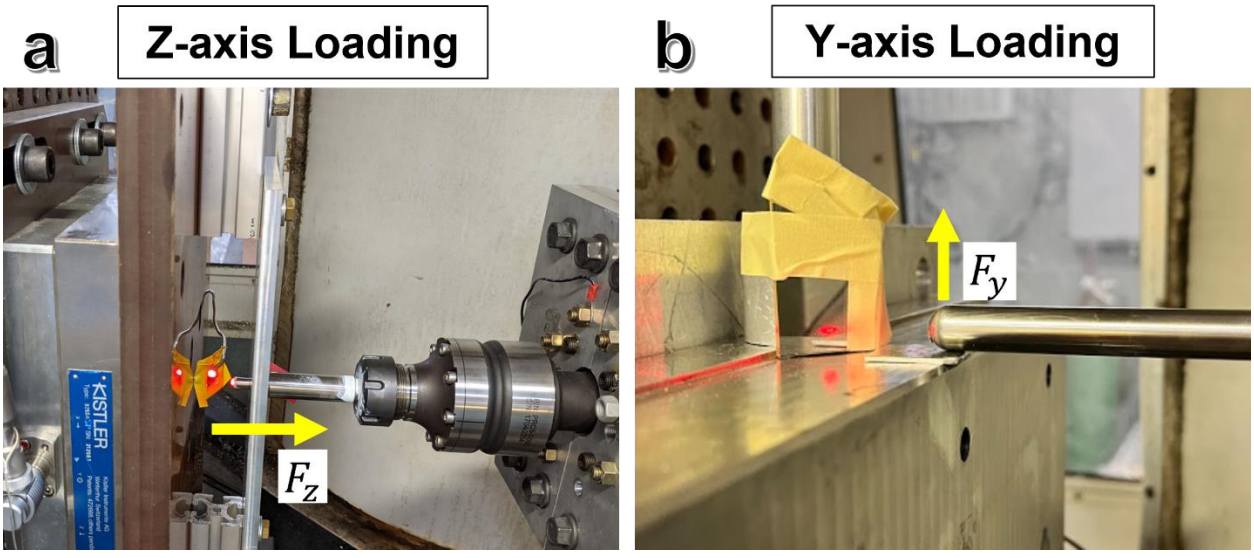

Figure 2-11 Incremental forming tool under a) Z-axis (axial) loading and b) Y-axis (planar) loading

amplitudes and low variability under load. Based on **Figure 2-12**a, the amplitude curves show a consistent shape and the Z-axial load window for these ISF experiments fall within the 1400-1700N which has low variability. The measured Y-axis load vs amplitude, **Figure 2-12**b, shows an even lower variability. Therefore, the operation of this ultrasonic stack is suitable for UA-ISF experiments.

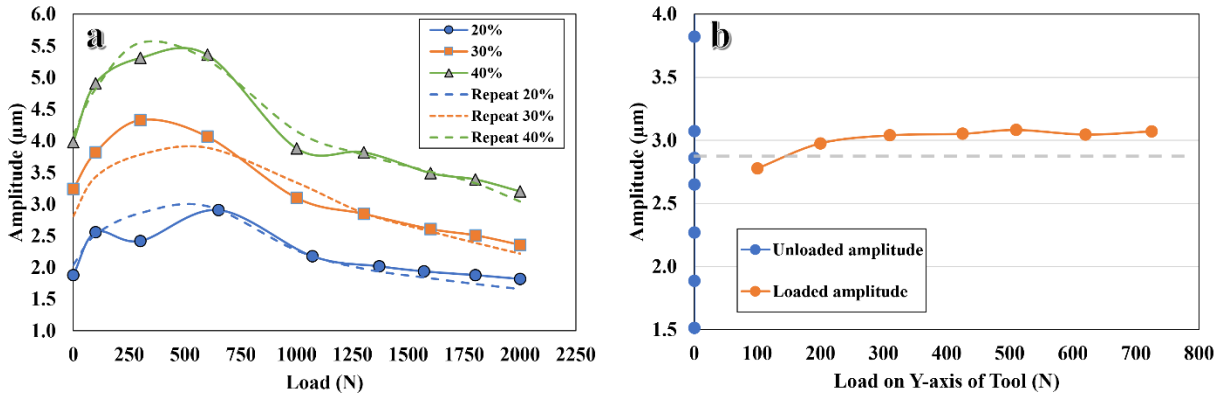

Figure 2-12 Vibration amplitude under a) Z-axis (axial) load and b) Y-axis (planar) load

2.5 Background Summary

In summary, the areas requiring further improvement in ISF includes surface finish, residual stress, and compliance/geometric accuracy. The introduction of ultrasonic vibrations in manufacturing can be beneficial in minimizing friction conditions and lower the forming force of a particular material and process. The current breadth of literature is limited in implementing ultrasonic vibrations in incremental forming and its impact on sheet characteristic; a similar statement can be made on how the unique contact mechanics and deformation modes in ISF might influence the observed softening magnitude. This dissertation presents the first known implementation of the APE on TPIF configuration and fundamental studies on ultrasonic assisted compression and indentation experiment.

CHAPTER 3
Experimental Investigation of Ultrasonic-Assisted Incremental Sheet Forming

Note: Portions of this chapter have been adapted from Cheng et al. [59,85] publications.

3.1 Introduction

Introduction of smart manufacturing techniques to address common concerns of spring back, surface finish, and geometric accuracy have provided additional resources to improve the manufacturing readiness of incremental forming (ISF) [24-26]. This chapter explores an alternative ISF method by adding ultrasonic vibrations to the process, called: ultrasonic assisted incremental forming (UA-ISF). At the time of the experimental work presented in this chapter, the reported literature on UA-ISF had been limited to forming a simple linear groove [28] and single point press simulation [30]. However, the initial work from Vahdati et al. [28] indicated significant promise. It is hypothesized that the ultrasonic metal forming characteristics, such as reduction in flow stresses and coefficient of friction, can serve to improve part outcomes of full scale ISF geometries.

The investigations presented in this chapter seeks to answer the following questions: 1) does UA-SPIF and -TPIF achieve similar ultrasonic metal forming characteristics? 2) If so, how might the force reduction and friction conditions evolve relative to selected ISF process parameters and transducer parameters? This chapter represents the one of the first examples of UA-SPIF and the first demonstration of UA-TPIF process. UA-SPIF experiments were performed at the EWI facility and only later did we acquire the ultrasonic transducer and integrate it with our Cincinnati machine

located in the Wu Center at University of Michigan. A design of experiments was introduced to investigation the forming force sensitivity, in UA-TPIF, to available tool path and amplitude parameters. Parts were sectioned and characterized using secondary electron microscopy (SEM), electron back-scatter diffraction (EBSD), and optical profilometry to investigate the change in tribological features, microstructure, and surface finish respectively. To conclude the chapter, the observed experimental results were compared to UAC/UAT and similar complex forming processes with integrated ultrasonic vibrations.

3.2 Ultrasonic-assisted single-point ISF (UA-SPIF)

This section explores UA-SPIF. The following questions for this experiment are: 1) is ultrasonic softening present in UA-SPIF and 2) can ultrasonic softening increase the formability limit? Axis symmetric cones with wall angles α = 45° and 67° were formed. A funnel geometry that has an increasing wall angle from 25°-83° was formed to test the formability of the process. SPIF experiments were performed at Edison Welding Institute.

3.2.1 Experimental setup & Methods

A schematic illustration of the ultrasonically assisted SPIF system is shown in **Figure 3-1**. The incremental forming tool, 12.7mm in diameter, vibrates longitudinally and is made of a tool steel A2 material. The tool protrusion length was measured to be 127mm and coupled with the transducer to achieve a resonant frequency of 20kHz. The vibration amplitude was measured using a laser vibrometer on the unloaded tool under different levels of power output from the ultrasonic generator. The vibration amplitude reported is that of the unloaded tool. A Kistler dynamometer, 9255A is mounted below the blank holder to measure the forming force during the process.

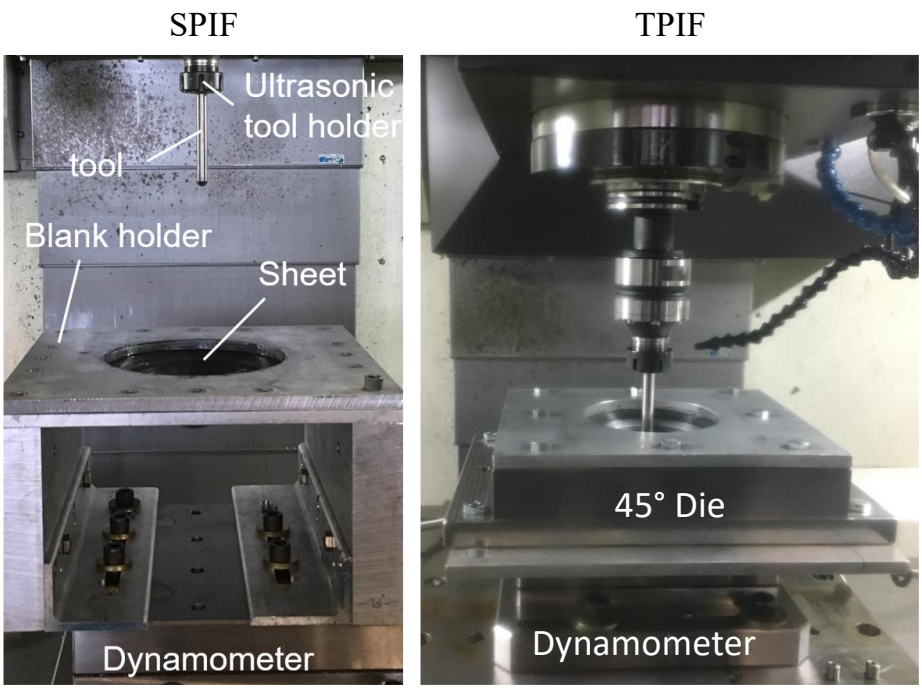

Figure 3-1 Single-point and two-point ISF setups at EWI

The sheet material is Al 7075-O with a thickness t_0 = 1.57mm. A layer of MoS_2 grease was spread across the tool-sheet interface only once prior to forming. As compared to our prior work [24,61] which used a freely rotating spindle, the CNC used in this study used a minimum spindle rotation speed of 15 revolutions per minute (rpm). The step size was set to 0.5mm. Both 45° and 67° axisymmetric cones were formed to a depth of 50mm, and a funnel geometry was formed to a depth of 68.5mm starting at a 25° angle and ending at 84°. The diameter of the binder opening was measured to be 159mm. The standard dynamometer sampling frequency in the tests was 10Hz. The ultrasonic softening percent was calculated using Equation x. The axial force refers to the Z axis and the planar force is the resultant of the X and Y forces defined by:

$$F_r = \sqrt{F_x^2 + F_y^2} \tag{3.1}$$

3.2.2 Results and discussion

Starting with the funnel geometry, a control sample along with three ultrasonic vibrated samples were formed and their forming forces are plotted in **Figure 3-2a**. The ultrasonic assisted samples show a lower axial force compared to the control sample and the calculated average reduction is summarized in **Figure 3-2d**. Based on these results, there are three distinct observations. First, the wall angle at failure did not change when adding the ultrasonic vibrations in this amplitude range. The calculated wall angle at failure was initially determined to be between 80-84° [78] however, the part was later scanned using a laser profilometer and the actual wall angle at failure was 73-74°. This coincides with forming limits reported in literature for aluminum alloys. Second, the softening effect was quite small relative to compression experiments reported in literature. This UA-SPIF process reaches a maximum of 5% reduction in forming force while Yao et al. [70] reported a 35% reduction in flow stress in compression of a 2mm thick specimen with a 2µm amplitude. Third, periodic dips in the axial force appear throughout the forming of the funnel geometry. The periods in time are consisted along all three vibrated samples while the control sample has no visible dip in force. To investigate this irregularity, wall angles of 67° and 45°were selected and formed using a constant wall angle tool path.

Figure 3-2b shows the forming force for the 67° cone geometry with constant wall angle. The forming forces shown were smoothed using a moving mean function with a 10-data point sliding window to better distinguish between samples. The dip in axial force between 200-400s is due to a thinning band that is commonly observed in forming of the 67° axis symmetric cone [61]. This thinning is due to a local instability during SPIF forming. At these high wall angles, bending occurs away from the tool contact area and at the binder-sheet interface. As such, the wall angle is

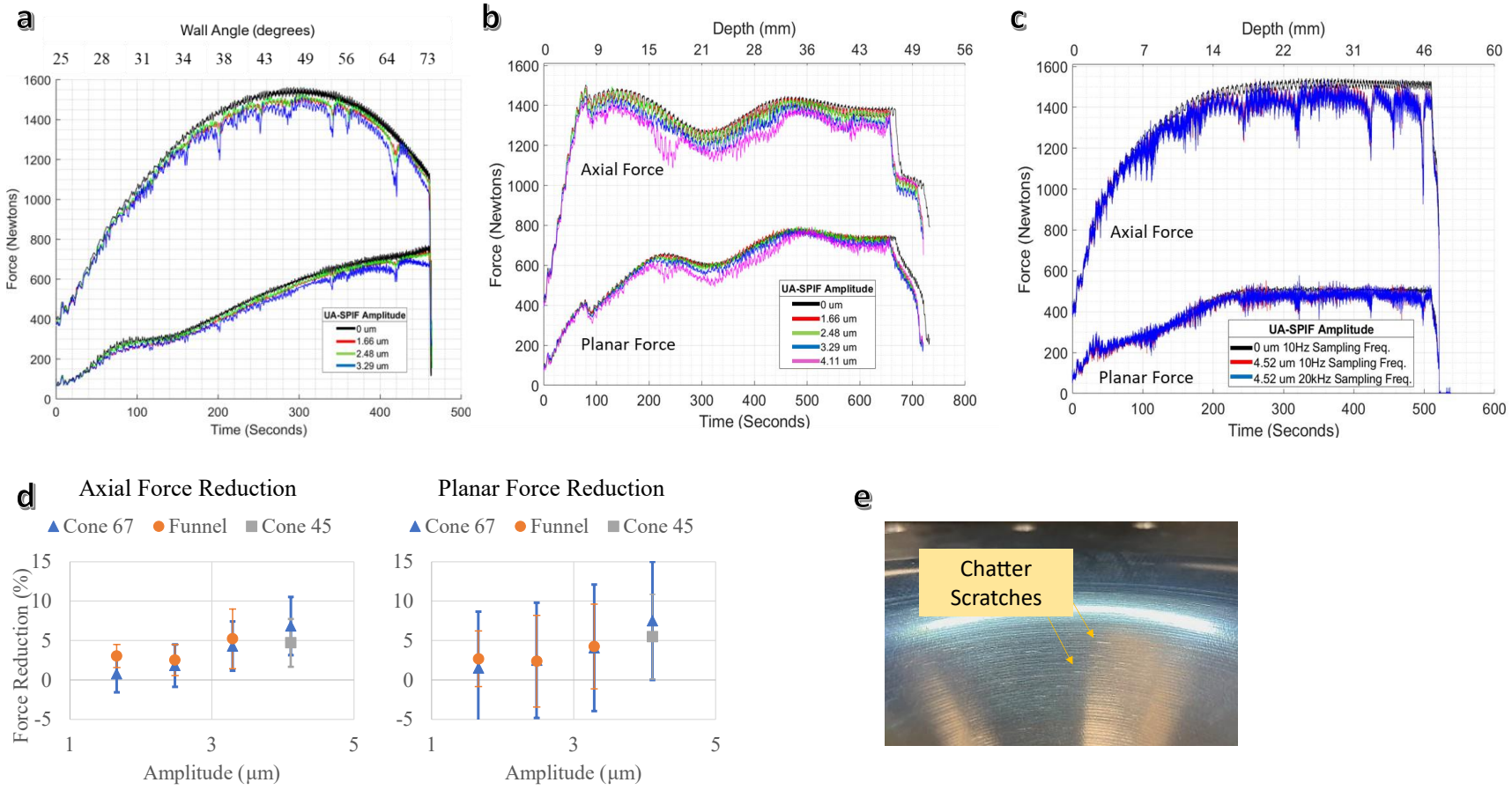

Figure 3-2 Ultrasonic-assisted single-point ISF (UA-SPIF). UA-SPIF of a) variable wall-angle funnel geometry, b) 67° constant wall-angle cone, and c) 45 ° constant wall-angle cone; d) average reductions in axial and planar force directions of each UA-SPIF geometry

greater than the programmed tool path of 67° and leans towards a punching deformation mode where the sheet stretches more [77]. This stretching thins the sheet locally, but the strain hardening prevents that sheet from fracturing or tearing. The force reductions are evenly spread throughout the axial forming force; the planar force shows a distinct benefit near the thinning band region. When considering the mean force reductions plotted in **Figure 3-2d**, the 4.11µm vibrated sample is the only non-negative planar force condition when considering the spread in the standard deviation. Dips in forming force appear twice in the 67° cone at 220s and 600s.

Finally, the 45° cone was formed without vibration as the control case and with a vibration amplitude of 4.52µm, **Figure 3-2c**. The mean force reduction in the axial and planar directions was calculated to be 4.7% and 5.5% respectively. The axial force shows significant force dips throughout the process. The sampling frequency for these experiments was set to 10Hz. A hypothesis was made that the sampling frequency might be too small and leaves out intermediate information. Therefore, the 45° cone was replicated using 20kHz sampling frequency, matching the operating frequency of the transducer. As shown in **Figure 3-2c**, the forming forces for both 10Hz and 20kHz samples are identical. This, along with the results from the 67° cone, suggests that the force dips do not represent an optimal forming angle with ultrasonic softening. Experimental observations of a high pitching noise occurring periodically through UA-SPIF suggests local instabilities in contact. Audible pitching noises represent a local resonance of the sheet; the vibrating nature of the free hanging sheet is a plausible explanation a short period drop in the recorded force.

To conclude, the results from UA-SPIF shows very minor reductions in forming force within this amplitude window. The formability in SPIF is not enhanced when super-imposing ultrasonic vibrations as shown by the consistent fracture between the control and vibrated funnel

geometry. The free hanging nature of the sheet creates an inefficient transfer of acoustic energy or vibration energy towards plastic deformation and instead elicits elastic vibrations of the sheet itself. Counter to this finding, other researchers have demonstrated successful implementation of UA-SPIF with greater softening effects [35,73]. The conditions of sheet opening, sheet thickness, tool size, and vibration amplitude are hypothesized to be contributing factors to the success of UA-SPIF. The ability to predict the likelihood of resonance for a particular geometry will prove to be challenging; a modal analysis of the part at each incremental in time is required to predict resonance. In addition, the elastic vibrations create cosmetic defects called chatter marks illustrated in **Figure 3-2e**. These conditions make UA-SPIF a challenge and thus, the next section investigates UA-TPIF.

3.3 Ultrasonic-assisted two-point ISF (UA-TPIF)

This section seeks to answer the following: 1) does a partial die prevent excessive elastic vibration of the sheet, 2) is the ultrasonic softening effect greater than the initial observations from UA-SPIF, 3) is there a change in surface finish present in UA-TPIF, and 4) how does a reduction in forming force affect the movement of material? Material movement is analogous to material flow caused by plastic deformation in rolling and extrusion; a fixed point on the material is displaced via plastic deformation and not rotations. Material movement has been documented by the UM team [24,77] in high squeeze factor TPIF conditions and is measurable through a combination of thickness measurements and surface characterization.

Initial UA-TPIF experimental results collected at the Edison Welding Institute (EWI) are presented in this chapter. The transducer device was later acquired and brought in house to the Wu Center at UM where a design of experiments was performed to gain better understanding of UA-TPIF conditions.

3.3.1 Experimental Setup & Methods – preliminary study

A schematic illustration of the TPIF setup is shown in **Figure 3-1b**. The tool diameter remained the same, t_d = 12.7mm, and again vibrates longitudinally. The notable difference between the TPIF and SPIF setup is the negative 45° die placed below the binder to provide support. The "negative die" nomenclature implies that the sheet is deformed into the mold like the schematic in **Figure 2-1**. The vibration frequency and dynamometer sampling rate remain the same at 20kHz and 10Hz respectively. MoS_2 grease was applied on both the tool-sheet and sheet-die surfaces to prevent sticking and excessive wear. The die material was machined from a tool steel material.

45° cones with different step sizes, 0.25mm and 0.5mm, were initially formed in the SPIF configuration to determine the steady-state axial force. The tool paths were later modified to increase the programmed squeeze and allow for squeezing of the sheet against the die. Increasing the programmed squeeze simply implies increasing the diameter of the tool path at each Δz step. The successful implementation of SF was observed when the TPIF F_z > SPIF F_z. After forming, the parts were scanned using a non-contact, coordinate measuring machine (CMM): Romer Absolute Arm with Integrated Scanner (Hexagon-7525SI). The thickness of the part was calculated using the Polyworks software and a 3D thickness color map is presented for these two tool path

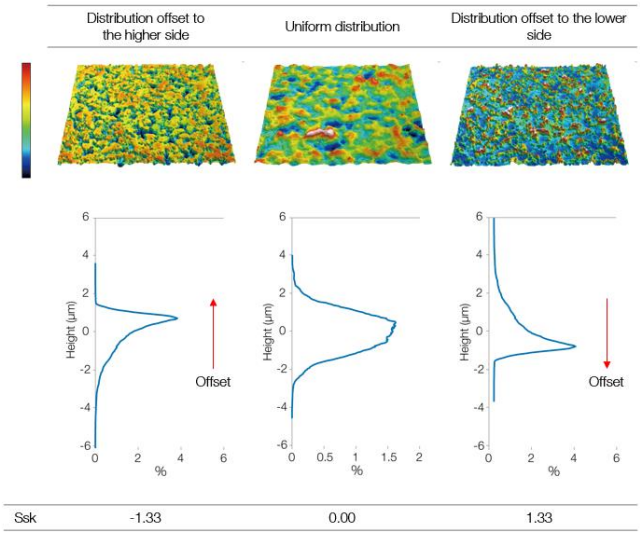

Figure 3-3 Diagrams representing the skewness of a surface [79]

conditions. The scanned 3D mesh required a thickness calibration; the two surfaces, tool-sheet and sheet-die, were manually shifted to calibrate the undeformed region of the part to the measured initial thickness. The surface roughness was quantified using a white light optical profilometer: DSX 510 from Olympus. S_q, S_a, S_p, S_v, S_z corresponds to the root mean square roughness, the arithmetic mean roughness, peak height of asperities, valley depth of asperities, and max valley-peak distance respectively. S_{sk} & S_{ku} is the skewness and kurtosis parameters and their corresponding surface profiles are illustrated in **Figure 3-3**. Scanning areas of 400µm x 400µm were sampled in 5 separate areas in the UA and non-UA regions.

3.3.2 Forming forces with and without ultrasonic assistance

Figure 3-4a demonstrates the transition from a SPIF conditions to a TPIF condition with positive squeeze. The SPIF and degenerative TPIF conditions both have an identical steady state axial force; thus, the sheet in the degenerative TPIF does not make use of the die support. The positive squeeze TPIF reaches a steady state axial force of 1700N, representing a 13.3% increase. A vibration amplitude of 3.29µm was switched on at 380 seconds into the forming process. The axial force shows a distinct drop at 380s and asymptotes to a mean force lower than the 1700N steady

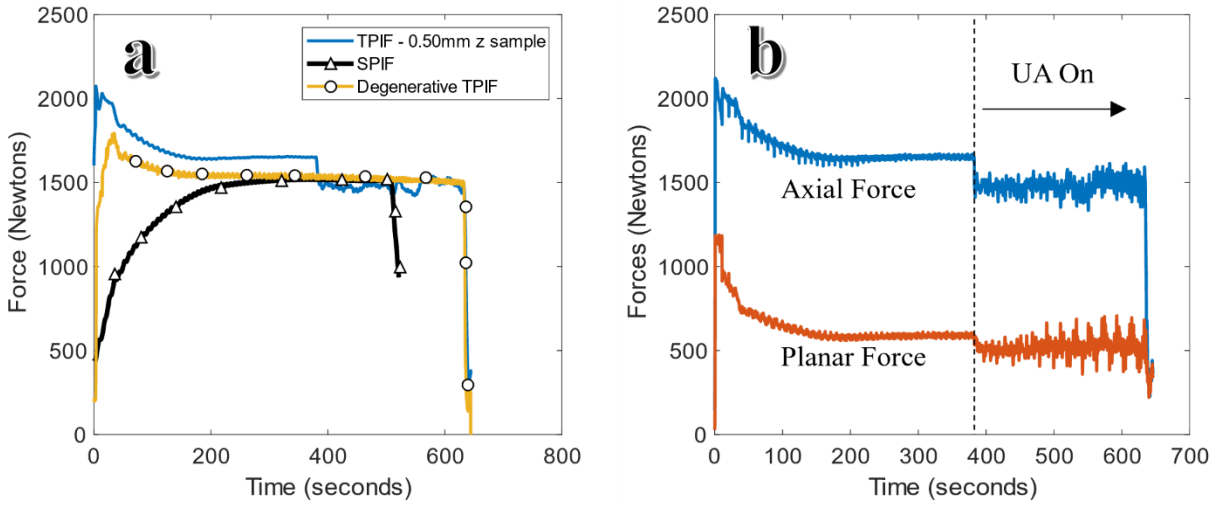

Figure 3-4 ISF of 45° cones. (Left) SPIF, Degenerative SPIF, and TPIF samples for the 0.50mm tool path. (Right) UA-TPIF sample with an applied amplitude of 3.29µm.

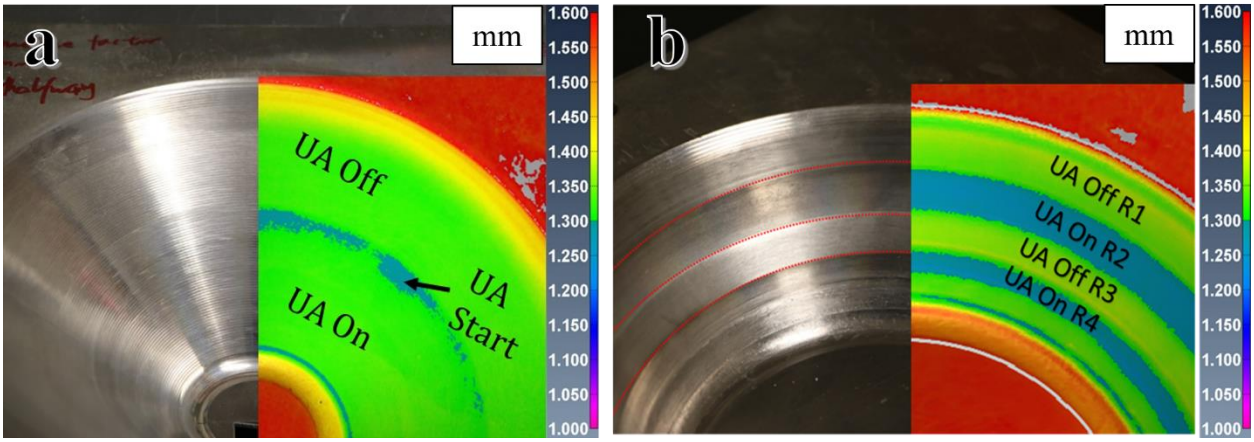

Figure 3-5 3D thickness color map (mm) overlaid on macro images of a) 0.50mm and b) 0.25mm 45° cones.

state and slightly below the 1500N steady state region of the SPIF part. The forces for the ultrasonic assisted sample are plotted in **Figure 3-4b** and the mean force reduction was calculated to be 11% and 15% in the axial and planar directions respectively. The recorded drop in force is immediate and affirms the observations of ultrasonic assisted compression and tension tests in literature [66]. A drop in flow stress corresponds to greater strain as shown in ultrasonic indentation of aluminum from Siu et al. [80] and ultrasonic soldering of gold from Lum et al. [81].

A thickness color map is presented in **Figure 3-5**a. An initial thickness transient occurs when the vibration was first switched on. However, as the forming progresses, the thickness returns to a similar thickness as the conventionally formed region. Therefore, a net zero material movement is observed for these conditions. Looking more closely at the surface profiles of the scallops, **Figure 3-6**, the ultrasonic and conventionally formed regions are not identical. The larger depth of the ultrasonic assisted region implies a greater strain and area of deformation. However, the 0.5mm step size likely pushes some of the material into the previous Δz pass instead of a net forward movement. Under the same vibration amplitude and smaller Δz, a net flow of material towards to sheet center is possible.

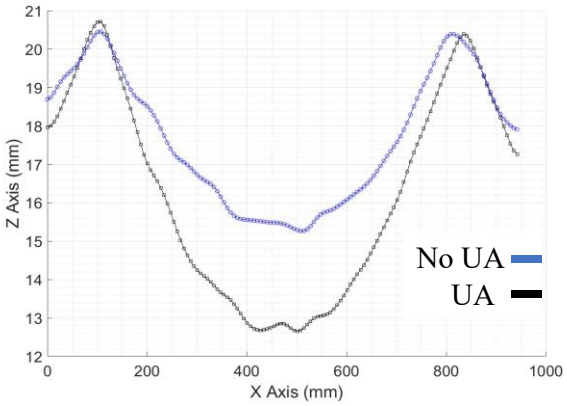

Figure 3-6 Surface profile comparing the no-UA and UA regions of the 0.50mm sample.

Figure 3-7 shows the forming force for the 0.25mm step size. In this example, the vibration was switch on at two separate periods at indicated by regions R2 and R4; the other divided regions, R1, R3, and R5 are not vibrated. The purpose was to observe how the material behaves after ultrasonic vibration. The 0.25mm sample shows similar immediate drops in axial force and a more gradual response in the planar force. The mean force reduction in R1 was calculated to be 18% and 16% for the axial and planar force respectively. In both regions after switching the vibrations off, R3 and R5, the axial forming force increases slightly. Residual hardening has been reported in UA compression test in literature and was the initial hypothesis to the change in axial force. However,

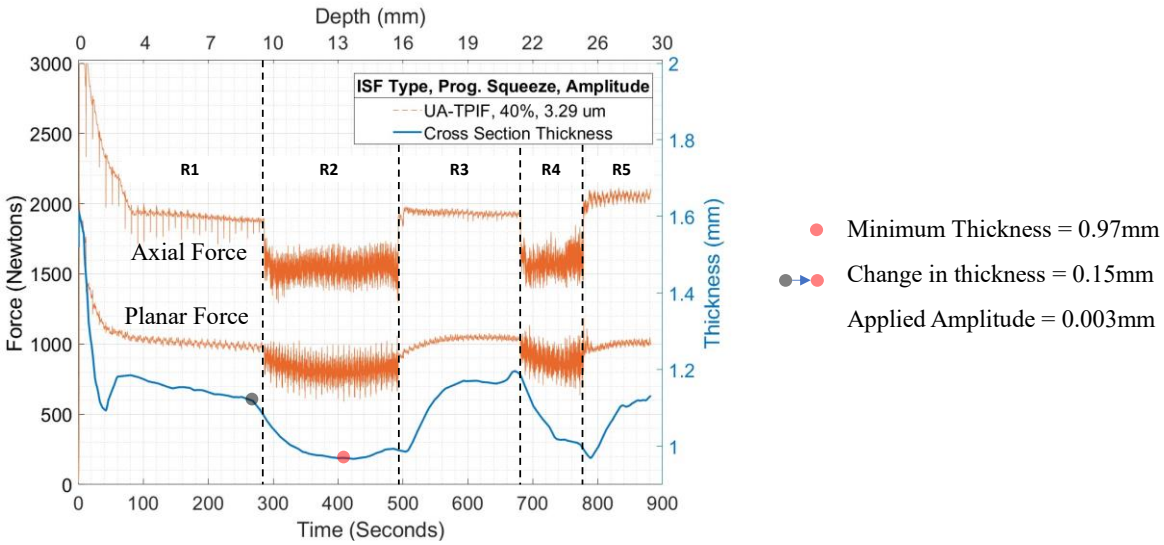

Figure 3-7 Axial and planar forming force for 0.25mm cone sample. Regions R2 and R3 are ultrasonic-assisted regions. A cross section extracted from the CMM scan is plotted along the right axis in units of mm.

the cross-sectional thickness taken from the 3D scan shows a large change in thickness during UA and post-UA. The measured drop in thickness from the beginning of R2 to the minimal point in R2 was 150µm, two orders of magnitude larger than the applied amplitude, 3.29µm. This finding was the first indication that UA-TPIF exhibits similar ultrasonic metal forming characteristics and the significant change in thickness is evidence to confirm the acoustoplasticity effect. Further observation of the thickness map, **Figure 3-5b**, shows a sustained thickness reduction during the UA regions indicated by the blue banded area in.

3.3.3 Surface quality

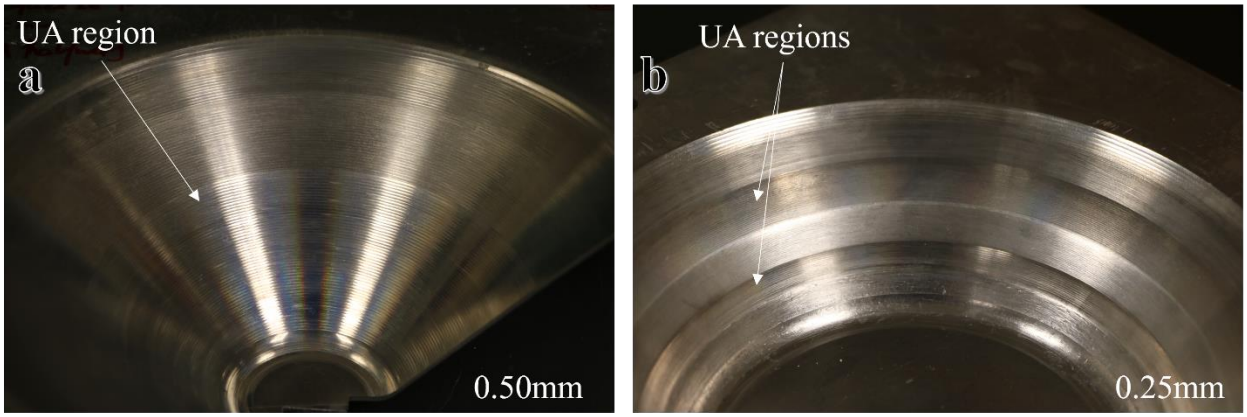

Figure 3-8 Macro images of a) 0.50mm and b) 0.25mm samples.

Figure 3-8 shows macro images for the 0.50mm and 0.25mm samples. One distinct indication of ultrasonic assistance is the rainbow-like reflection on the tool-sheet surface. This is discussed briefly later in the section. Starting with lower SEM magnifications in **Figure 3-9**, there are clear differences in the tribological characteristic of non-UA and UA regions. In conventionally formed ISF, the surface appears to have tearing and dragging of aluminum created from the combination of bending on unbending and high contact pressures. The ultrasonic vibrations have lessened the density of tearing considerably. At higher magnification, the ultrasonic assisted has unique track-like markings across the sample surface. In measuring the spacing of those track marks, the length corresponds to the feed rate, F, of the tool divided by the vibrational frequency, f. A spacing of

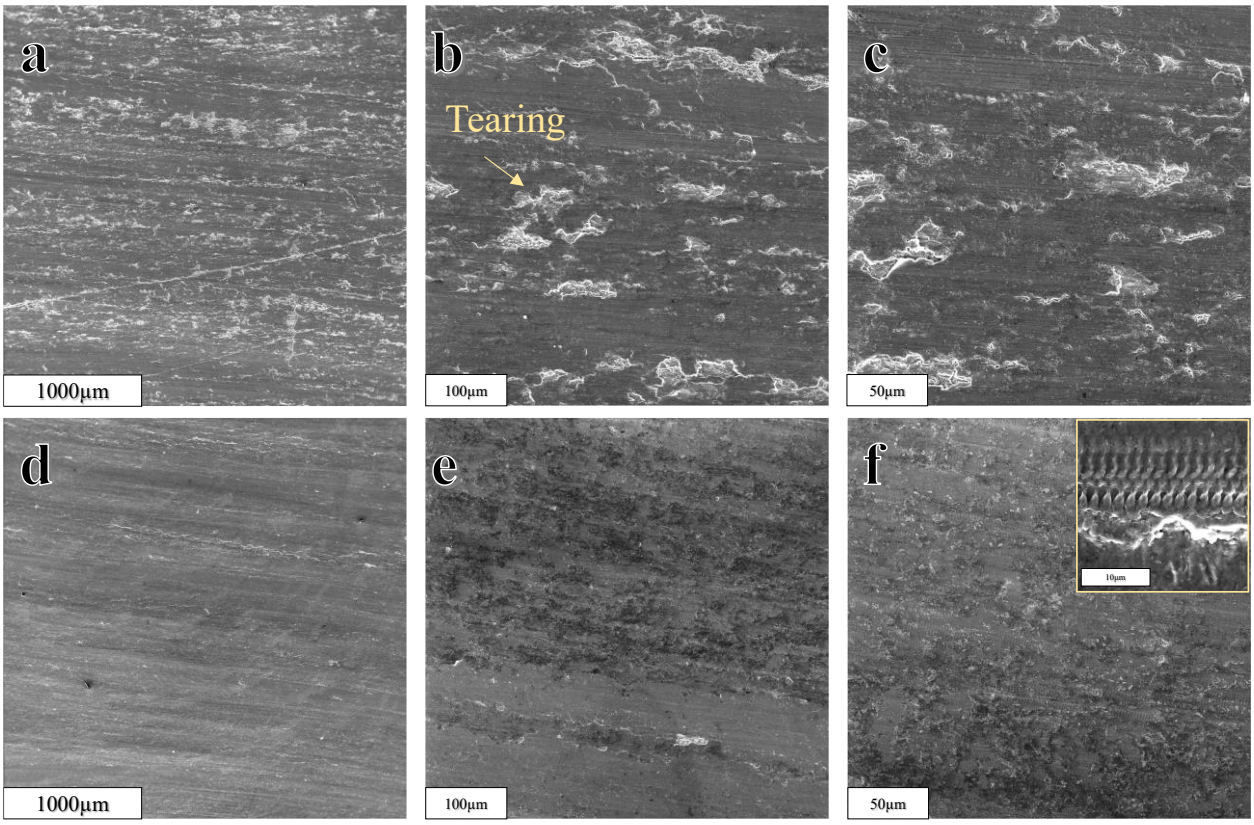

Figure 3-9 SEM images of the tool-sheet interface for the 0.50mm sample. (Top row) Increasing magnification SEM images showing tribological features in the non-UA region. (Bottom) Increasing magnification in the UA region

roughly 2µm. We hypothesize the presence of these track marks may be causing the rainbow-like reflectance but future work in this area is required to confirm. Let's consider the quantitative evaluation of surface roughness for the 0.5mm UA-TPIF sample, **Figure 3-11**. S_q & S_a indicate a slight improvement in surface roughness when adding vibrations to the process. S_p, S_v, S_z show significant improvements as well. These results confirm the initial findings from Vahdati et al. [28] where they formed a linear groove with incremental Δz steps to a depth of 5mm. The skewness S_{sk} was reported to be -0.81 ± 0.31 for the non-UA region and 0.06 ± 0.04 for the UA region. A negative S_{sk} implies sliding abrasion leading to a more pitted surface characteristic. A negatively skewed surface is typically good for holding lubricants. The UA region has a skewness close to 0 which implies a uniform representation of peaks and valleys. The kurtosis S_{ku} represents presence of inordinately high peaks/ deep valleys when $S_{ku} > 3$ and a lack thereof when $S_{ku} < 3$. The non-

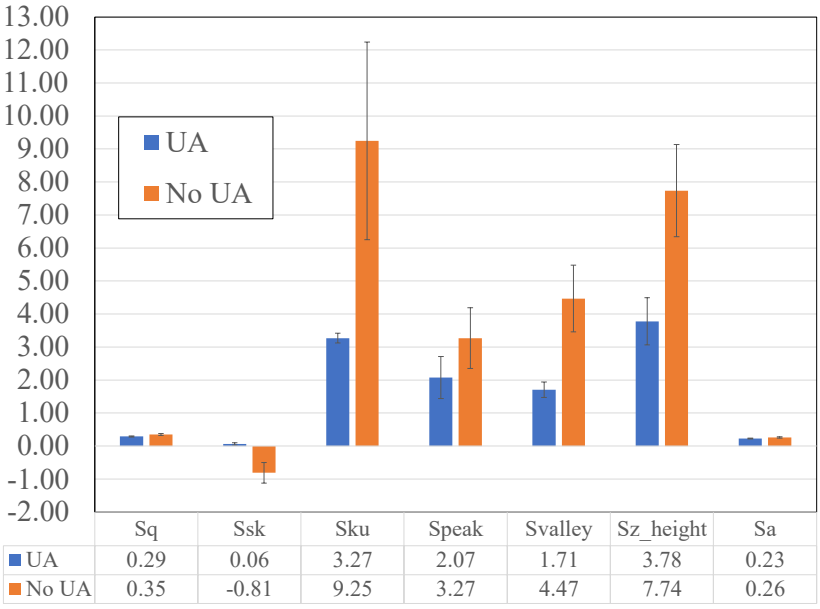

	Sq	Ssk	Sku	Speak	Svalley	Sz_height	Sa
UA	0.29	0.06	3.27	2.07	1.71	3.78	0.23
No UA	0.35	-0.81	9.25	3.27	4.47	7.74	0.26

Figure 3-10 Quantitative surface roughness parameters collected from the non-UA and UA regions of the 0.50mm sample

UA region has a kurtosis value 9.29 ± 3 and the UA region recorded a kurtosis value of 3.27 ± 0.15. Therefore, the addition of ultrasonic vibrations creates a normal distribution of surface asperities and valleys. The 0.25mm part roughness was not characterized here as the change in part thickness creates a difficult region to region comparison. Qualitatively, surface fractures or chipping is observed at the bottom of the geometry, **Figure 3-8b**. Based on previous tests conducted by the UM team, chipping and surface fracturing was observed when forming with a 4mm tool diameter. At small radii of curvature, the shear stress intensifies and can lead to cracking along the surface. For the 0.25mm sample, the cracking instead occurs with high degrees of strain hardening. Material is continuously pushed ahead of the tool and is worked multiple times. Whereas the 0.5mm sample has a net zero material movement and does not experience excess strain hardening.

In summary, UA-TPIF exhibits a much greater ultrasonic softening effect compared to UA-SPIF. The added die support removes experiment artifacts arising from sheet resonant vibration. The achieved force reduction for these two tool paths at a wall angle of 45° ranged between 11-

18% for the axial force and 15-16% for the planar force. Compared to the UA formed groove [34], the groove forming experiments exhibited 24-26% force reductions. There are two differences between these two setups. First, the deformation mode of the straight groove test differs from the cone geometry. Filice et al. [60] formed a cone geometry in SPIF and measured the expansion of electrolytically etch grids on the non-contact side. In first few spirals in the tool path, the diameter of the cone is large relative to t_d and as the forming progresses, this ratio decreases. The corresponding major-minor strains measured on the grid start with a plain strain condition and progresses to a more biaxial condition. The tool diameter in Vahdati's setup is large relative to the curvature of the groove and thus, the through thickness strain is likely more biaxial than the UA-TPIF conditions shown here. Amini et al. [29] performed a similar UA groove experiment and the measured major-minor strains fall in the positive quadrant, close to a slope of 1 which is a biaxial condition. Second, the same material in the groove geometry is continually stretched under ultrasonic softening effects. Although the overlap percentage in ISF is high, new material is continuous deformed. Based on these findings, a parametric analysis of vibration parameters and tool path parameters are required to correlate to material softening in ISF.

The addition of ultrasonic vibrations can eliminate abrasive wear between the hard tool and soft workpiece. The tearing features are minimized with UA and the skewness and kurtosis support a more normalized surface. However, a net flow of material into the center of the sheet can lead to significant work hardening and eventual cracking and chipping on the tool-sheet interface.

3.4 UA-TPIF - Influence of ISF parameters and amplitude on ultrasonic softening

This section further explores the use of ultrasonic assistance in TPIF with the goal of understanding how amplitude and tool path parameters affect the softening response. Reports of UA-ISF has been limited to UA-SPIF forming of straight groves which has limited variables and

a different deformation mode compared to UA-TPIF of cones. Vahdati et al. [28] formed the groove geometry with only one vibration amplitude. Yanle et al. [30] formed a straight groove with increasing vibration amplitude and observed a linear softening trend. Recently, Cheng et al. [35] expanded the parametric window of UA-SPIF of a pyramid geometry. There is no extensive review of how tool path parameters like feed rate (F), squeeze factor (SF), and step size (Δz) would impact the magnitude of softening in UA-TPIF. In this chapter, commercial aluminum alloys 2024-O and 7075-O were formed using UA-TPIF conditions. The softening response was recorded relative to ISF variables. These results are later compared to the softening response of aluminum in ultrasonic compression tests in literature. At the point, the ultrasonic device was acquired and move to the Wu Center at University of Michigan.

3.4.1 Experimental setup and methods

Conical, 45° wall angle, geometry was formed using two-point incremental forming. **Figure 3-11** shows the experimental setup located in a Cincinnati HMC 400 EP CNC machine. In this machine, the bed is vertically hanging as opposed to typical horizonal beds. On the bed, a Kistler 9255A sits between the die and the bed and measures the forming forces using a set of signal amplifiers and a data acquisition (DAQ) system. The sampling frequency of the DAQ system was set to 40Hz for all experiments. A binder was used to fix the sheet at the center of the die. Because the ultrasonic device taper did not match the chuck holder of the CNC, an adapter was created to fix the tool in place. Therefore, the tool rotation remains fixed. The transducer fixture was loaded against the die and the compliance was measured. The compliance was shown be linear and did not deviate under the loads typically observed in incremental forming therefore,

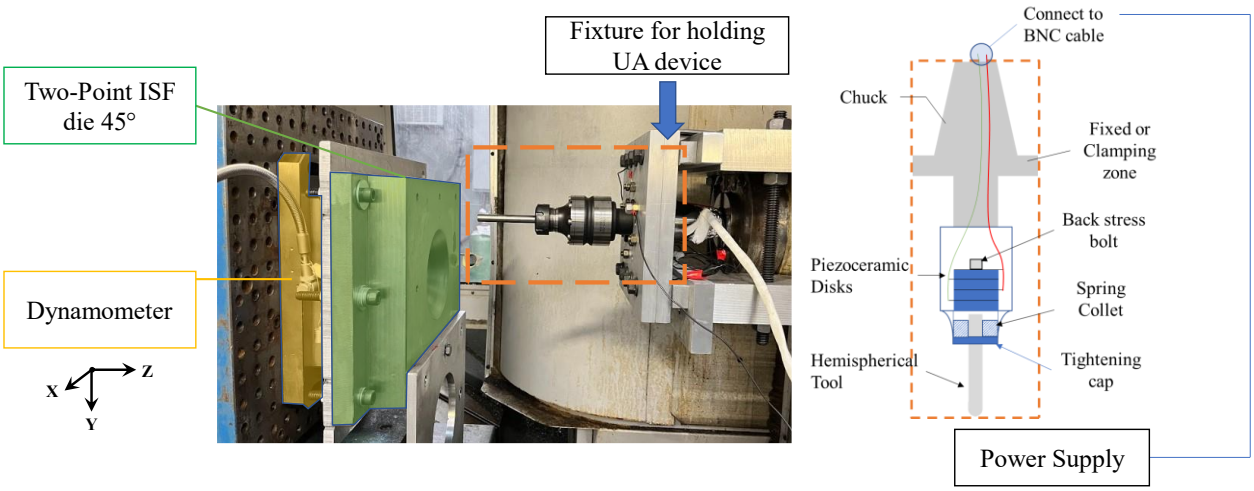

Figure 3-11 Ultrasonic-assisted ISF (UA-ISF) setup located in the Wu Center of University of Michigan.

it was deemed that the structural rigidity of the fixture was sufficient. A Dukane generator powered the ultrasonic transducer. The transducer operated at a frequency of 20kHz, and the highest amplitude used in this study was 6μm. Incremental forming parameters are listed in **Table 3-1**. Both AA2024-O and AA7075-O sheets have initial thicknesses of 1.6mm and were cut into 203mm x 203mm squares. A moly di-sulfide grease acted as the lubricant during the forming process.

Table 3-1 Description of independent and dependent process parameters for each study

	Constants			
Variable	Feed rate (F)	Squeeze (SF_p)	Step Size (Δz)	Tool diameter (t_d)
Feed rate (F)	--	55%	0.25mm	12.7mm
Squeeze (SF_p)	42mm/s	--	0.25mm	12.7mm
Step Size (Δz)	42mm/s	50-60%	--	12.7mm, 8.0mm

3.4.2 Results and discussion

This section focuses on varying process parameters: feed rate, programmed squeeze, step size, and tool diameter. The ultrasonic vibration was applied intermittently during incremental forming for

roughly 10 steps (Δz). For both the programmed squeeze and feed rate studies, a 12.7mm tool diameter and 3.16µm were used. Averages were taken from the ultrasonic assisted and control portions of the measured forming force.

3.4.2.1 Feed rate

As shown in **Figure 3-12a**, the feed rate was varied from 42mm/s to 10mm/s during ultrasonic assisted incremental forming. Progressively lower feed rates increased the softening response by 1.5%. The change in softening is minor and can be justified by considering the sinusoidal nature of the tool. With increasing feed rate, the horizontal distance traveled by the tool tip after 1 vibration cycle equals the feed rate divided by the tool frequency: $x(t) = \frac{F}{f}$. Changing the feed rate from 42mm/s to 10mm/s, narrows the horizontal tool tip displacement from 2.1µm to 0.5µm. The difference of 1.7µm has a minor effect on the strain gradient underneath the tool.

3.4.2.2 Programmed Squeeze

Another parameter that is specific to two-point incremental forming is programmed squeeze. By increasing the programmed squeeze during tool path planning, the tool presses the sheet against the die in ever greater increments. This reduces the distance between the tool contact point and the

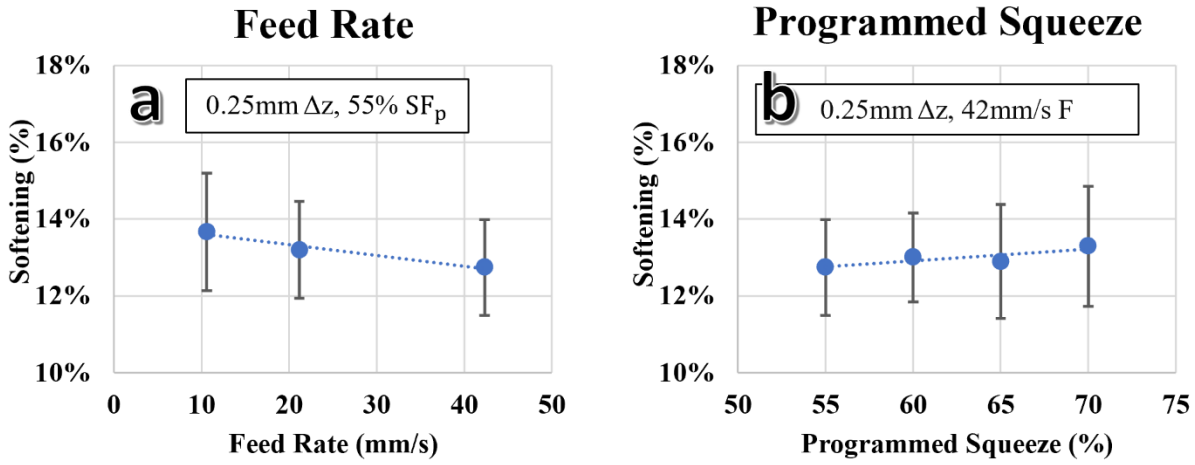

Figure 3-12 Change in softening effect relative to process parameters a) feed rate F and b) squeeze factor SF_p

die surface and effectively applies a greater strain through thickness. **Figure 3-12b** plots the softening response relative to the programmed squeeze. An increase in programmed squeeze from 55% to 70% lead to an improvement of 1%. Similar to feed rate, the programmed squeeze has an insignificant effect on the acoustic softening response within this range of squeeze. The positive trend however does suggest at higher compressive force elicits a greater softening effect.

3.4.2.3 Step Size

The step size refers the incremental plunge along the depth axis of the geometry. Increasing step size is known to increase the forming forces as the tool contact area is larger. In these experiments, both aluminum alloy grades were formed with step sizes of 0.25mm and 0.40mm as shown in **Figure 3-13**. The max softening achieved with this experimental setup was 27.2% at an amplitude of 5.9µm. A minimum softening effect of 5.6% was record at an amplitude of 2.7µm. Aluminum alloys 2024-O and 7075-O show no significant difference in acoustic softening response when formed using similar step sizes. The softening response appears to be linear which correlates well

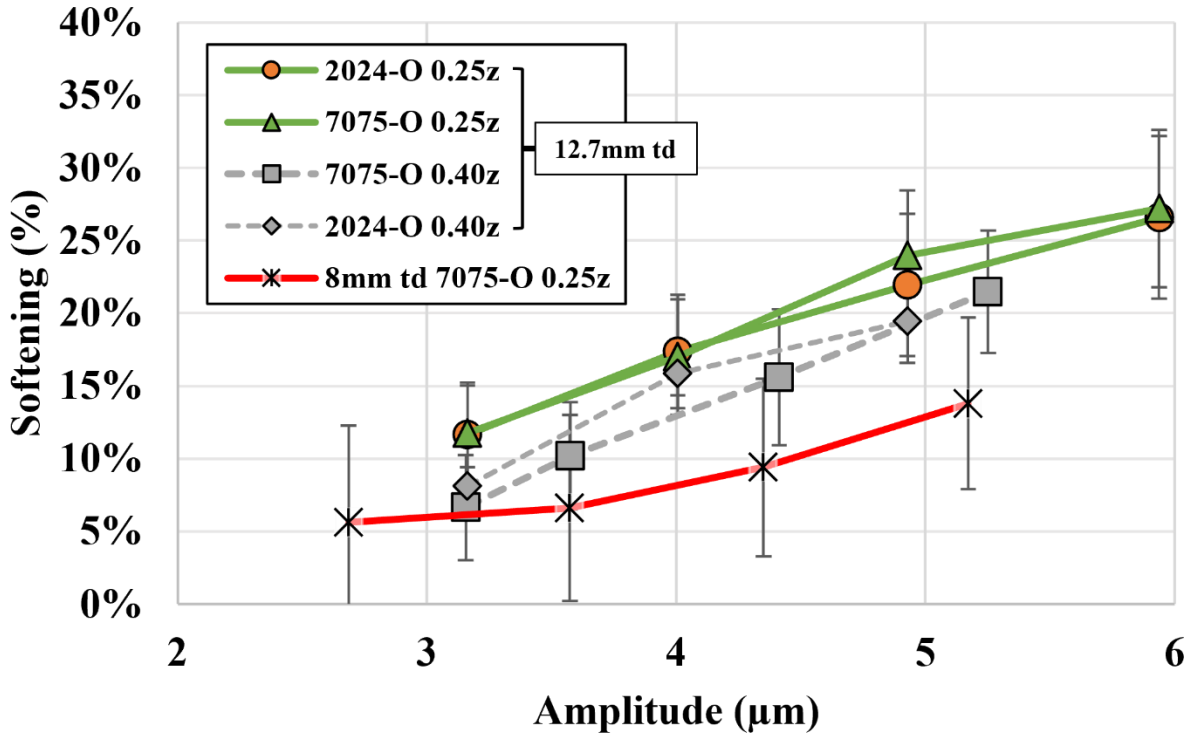

Figure 3-13 Softening effect relative to a change in step size for 12.7mm and 8.0mm tool diameters (td)

with literature when using UA-compression and UA-tension tests [38,66]. An increase in step size led to a 4-5% lowered softening response. The distance from the trough of the prior step to the current step can be determine using simple trigonometry as shown in Equation x:

$$h = \frac{\Delta z}{\sin(90 - \alpha)} \tag{3.2}$$

Where Δz is the step size, α is the wall angle, and h is the distance between the trough of the previous and current step. h was calculated to be 0.35mm and 0.57mm for 0.25mm and 0.40mm step sizes respectively. Another method is to consider the contact length and contact area overlap percent from the work of Bansal et al. [82]. As shown in **Figure 3-14**, the overlap length decreases by 2.6% and contact area increases by 10.4% when the step size increases. Therefore, the contact area is the more significant factor in the change in softening response. Considering this finding, the 12.7mm tool was replaced by a smaller 8.0mm tool. The contact area is roughly 45% percent

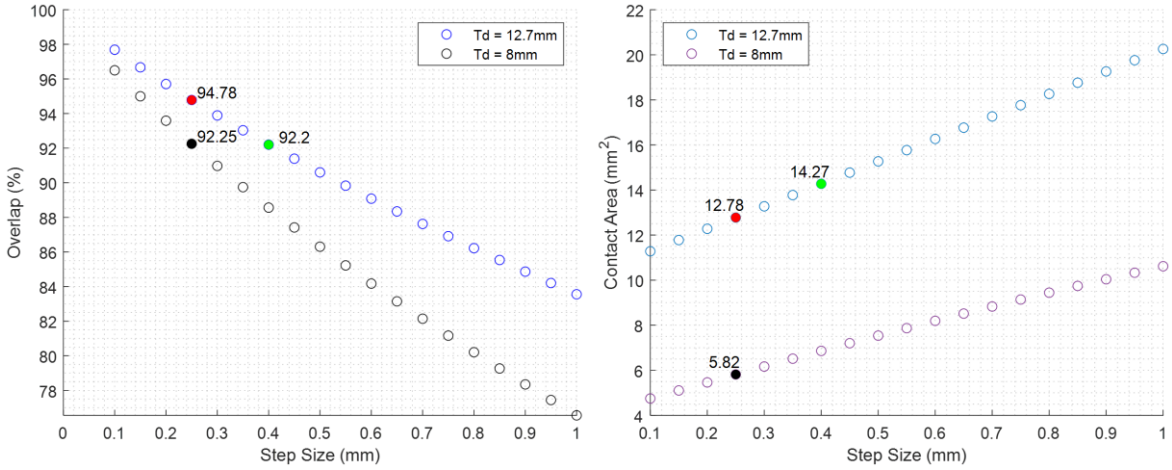

Figure 3-14 Analytical calculation of overlap percentage and contact area for 12.7mm and 8.0mm tool diameters. Calculated for a 45° constant wall-angle cone based on [66].

of the 12.7mm tool based on **Figure 3-14**. The average acoustic softening results are plotted in **Figure 3-13**. Under the same amplitude window, the 8.0mm tool displayed a smaller softening effect. This is contradictory to the previous finding where high overlap and small contact area is beneficial. We present a few hypotheses. One possible explanation is regarding the change in deformation mode. The smaller tool radius elicits higher localized strain, shear strain along the tool motion direction, and a larger strain gradient through thickness as the sheet is required to conform around a smaller tool. The increases in step size for the 12.7mm tool can promote greater bending-under tension deformation. Second, the distribution of the vibration vector has changed. In ultrasonic compression tests, the full sample gauge length is aligned with the vibration axis. In ISF, a rounded contact interface implies resultant vectors orientated normal to the curvature of the tool. Third, indentation deformation leads to higher participation of geometrically necessary dislocations (GNDs). GNDs along with statistically stored dislocations (SSDs) participate in material strain hardening. The dimensions of indentation size effects are typically on the order of nanometer to micron length scale which make this an unlikely hypothesis; however, Siu & Ngan [63] performed ultrasonic assisted indentation experiments (at the micron scale) and observed a

greater formation of sub-grain boundaries. The distributed vibration vector hypothesis is further discussed in **Chapter 5**.

3.5 Material movement in UA-TPIF

Geometric deviations in ISF arise from strain gradients through the thickness of the sheet. Another accuracy defect found in TPIF operations [24,77] is called a bulge defect as shown in **Figure 3-15**. Isidore et al. [83] proposed compressive stresses near the bottom bend are significant enough to cause the bulge defect. Later, Shin et al. [84] proposed a material flow model for TPIF conditions and concluded that a minor flow of material, pushed towards the center of the part, can lead to the formation of a bulge defect. This bulge defect can also be found in SPIF forming but to a more minor degree. Knowing the ultrasonic vibrations can soften the sheet metal, this section seeks to quantify the change in material movement in conventional TPIF and UA-TPIF conditions.

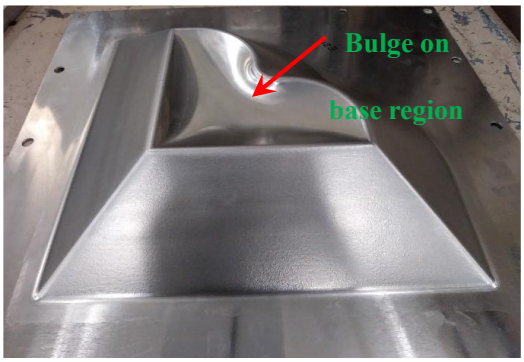

Figure 3-15 Heart shaped benchmark geometry with a geometric bulge defect. The sheet-die surface is shown

3.5.1 Experimental setup and methods

The TPIF forming parameters are listed in **Table 3-2**. AA7075-O sheets of 200mm x 200mm in size were selected for these experiments. The sheets were clamped onto the 45° die as shown in **Figure 3-11.** A think MoS_2 was applied to both tool-sheet and sheet-die surfaces. The tool path selected for this process is illustrated in Figure x. A two SF_p zone of 25% and 30% was created to characterize the material flow in each section. A $SF_p = 0\%$ or SPIF condition was place

in between the two zone to prevent material overflow. The parts were scanned using the non-contact, coordinate measuring machine (CMM): Romer Absolute Arm with Integrated Scanner (Hexagon-7525SI). The cross-sectional profiles were extracted from the Polyworks software and the bulge height between the ultrasonic-assisted and conventional parts are quantified. The surface was characterized qualitatively using SEM and quantitatively using an Olympus DSX 510 white light profilometer.

Table 3-2 ISF Process parameters - Material movement study

ISF Process Parameters	
Lubricant	Molybdenum Disulfide (MoS2)
Tool Diameter	8 mm
Blank Thickness	1.63 mm
Resonant Frequency	20,200 Hz
Feed Rate	42.3 mm/s
Step Size	0.25 mm
Spindle Rotation	Locked

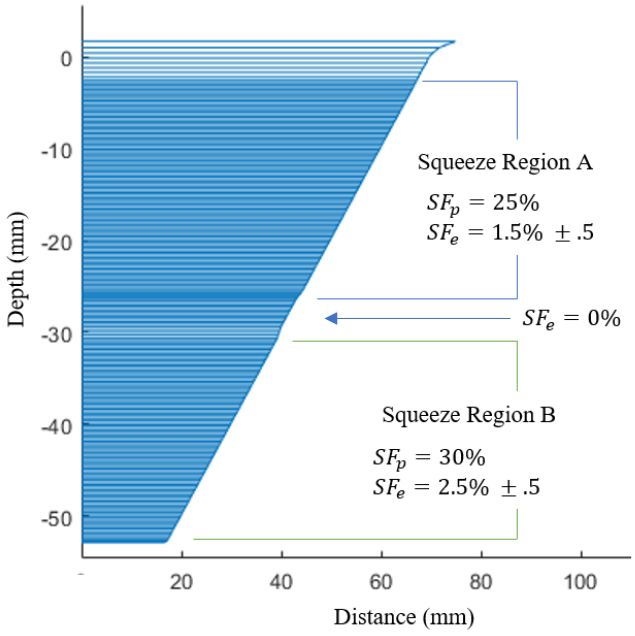

Figure 3-16 Tool path design for two zone SF_p regions

3.5.2 Results and discussion

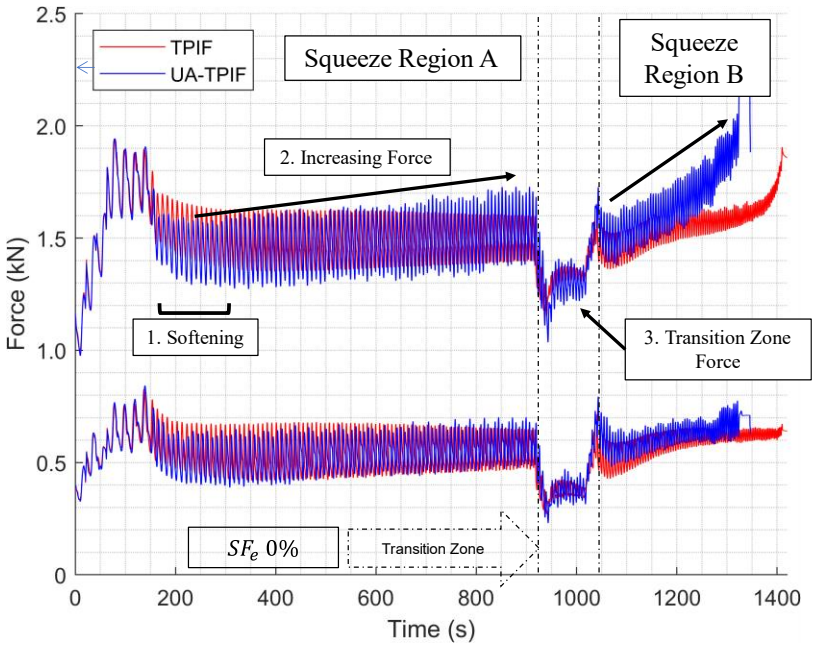

Figure 3-17 Forming force for TPIF and UA-TPIF samples.

The axial and planar forces are presented in **Figure 3-17.** A small softening effect is observed between 175s-450s. As the forming progresses, both axial and planar forces gradually increase for the UA-TPIF sample. As shown earlier in **Figure 3-7,** increases in forming force can be correlated to a change in sheet thickness and greater material flow. The TPIF sample shows a steady state forming force during squeeze region A and only when transitioning to squeeze region B do the forming forces increase significantly. The significant jump in axial force for each sample suggests a bulge defect has likely formed. The UA-TPIF forming was stopped prematurely to avoid engaging the machine overload condition. A better indicator of the bulge defect is shown by the macro images and cross-sectional profile in **Figure 3-18**. Both parts show a clean surface finish that resemble the surface of the die. A small orange peel band is observed in the TPIF sample, **Figure 3-18a**; this indicates that the sheet-die surface was not in contact during the transition zone. The UA-TPIF sample**, Figure 3-18b**, shows only a minor surface peel effect which implies the

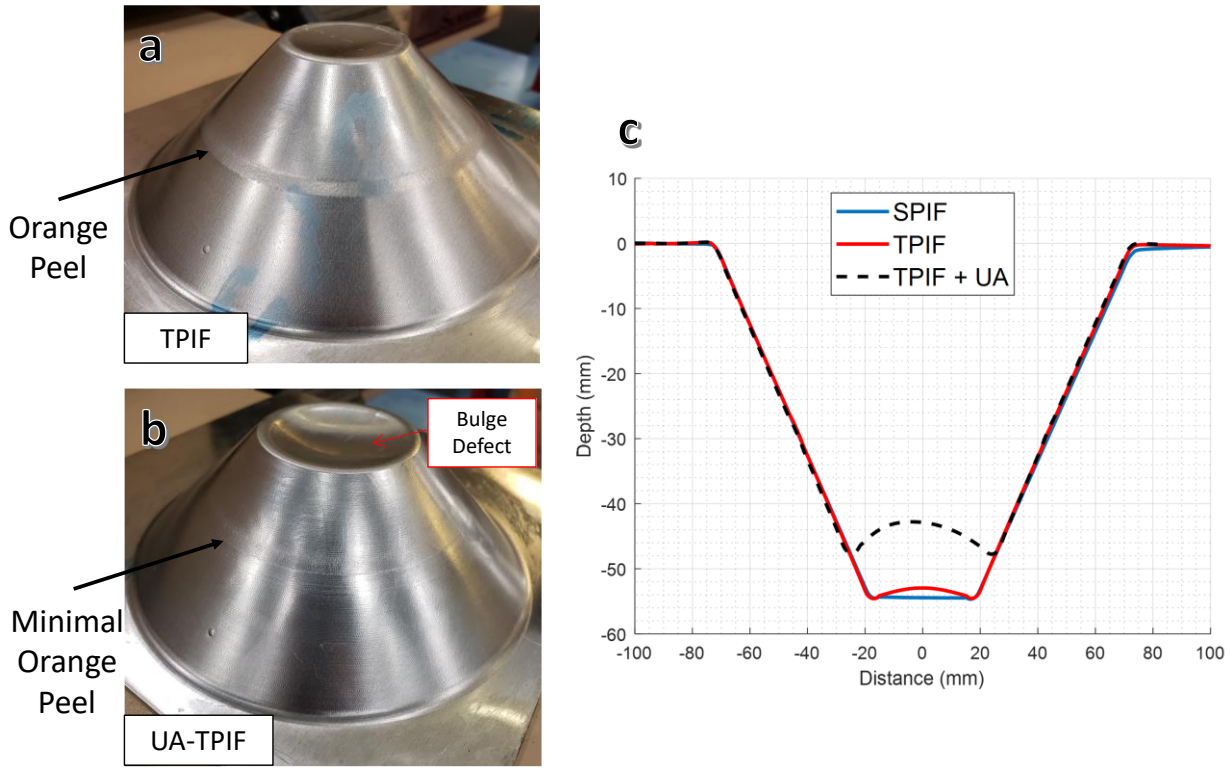

Figure 3-18 Macro images of a) the TPIF and b) UA-TPIF parts. The surface shown is the sheet-die surface. c) the top surface, cross-sectional profiles of the TPIF, UA-TPIF, and a SPIF equivalent.

material movement overflowed into the transition zone; a slightly thicker sheet reduces the programmed squeeze required for the two surfaces to touch. Both parts indicate a bulge defect; however, the bulge height is clearly larger in the ultrasonic assisted sample as indicated by the cross-sectional profile in **Figure 3-18c.** The material movement can be quantified by measuring the differences in scallop profiles [77,85-86]. The TPIF and UA-TPIF scallop profiles are plotted in **Figure 3-19a**. A conservative approximation is to assume the thickness at the scallop peaks are equivalent; the ultrasonic assisted sample clearly shows a greater depth and therefore, more material movement. The accumulation of the material movement for the respective squeeze regions in **Figure 3-19b** agrees with the hypothesis as an indicator for bulge formation. A more accurate methodology would be to measure the full thickness in addition to the surface profile. Once the material accumulated area is known, the area can be distributed into the starting sheet thickness and be treated as a beam bending condition as described in [77]; the beam bending was

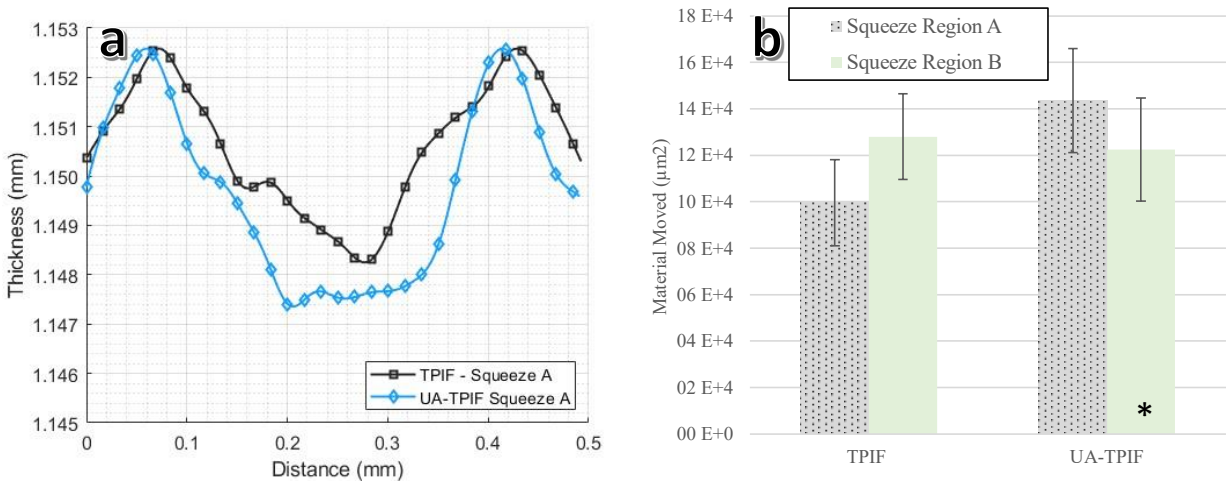

Figure 3-19 Surface profile of TPIF and UA-TPIF parts in squeeze region A (left). The accumulated area below the scallop peaks in their respective parts and squeeze regions. *the UA-TPIF part was stopped prematurely.

treated as a sine wave and the height of the bulge is approximated numerically by fitting sine wave parameters to solve for the amplitude of the wave. Further details of the process can be found in [77]. The sheet profiles and thickness distribution near the last tool contact position are shown in **Figure 3-20**. The ultrasonic assisted condition shows a smaller thickness prior to the tool contact region and an increase in thickness within the tool contact region. The results support the notion of greater material pushed towards the center of the part. Given the high amount of material accumulation and therefore strain hardening, the surface quality is of concern. The SPIF and TPIF

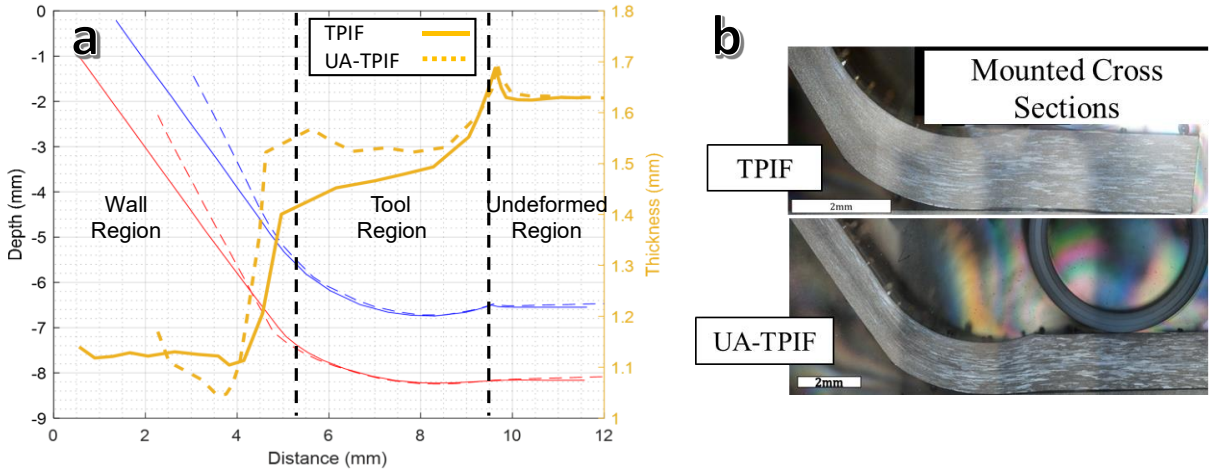

Figure 3-20 a) Sheet profiles and corresponding thickness; b) cross-sectional image near the bottom of the sheet or the last tool contact position.

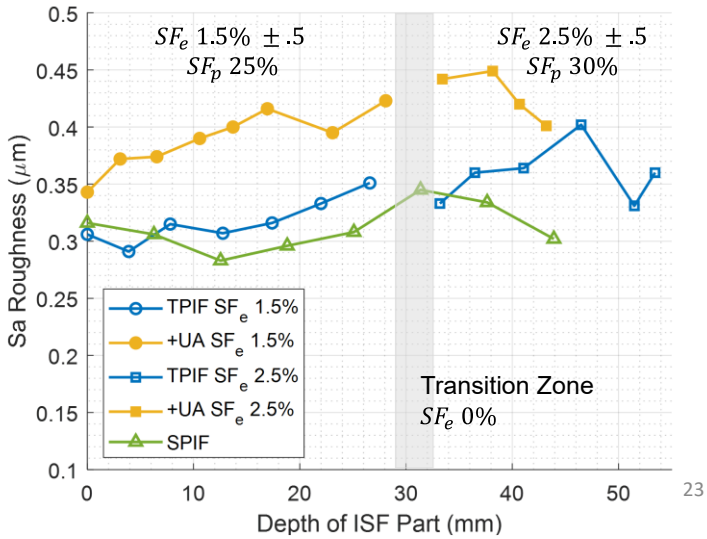

Figure 3-21 Surface roughness as a function of part depth

sample roughness, **Figure 3-21**, are similar and increases as the forming progress. The UA-TPIF sample shows a high roughness value from the beginning of the process and is elevated compared to the TPIF sample. High amounts of material movement lead to greater surface roughness.

In summary, the combination of programmed squeeze and ultrasonic vibrations can exacerbate the conditions required for a bulge defect to form. The material accumulation can be conservatively approximated by measuring the area bellow the scallop peaks and multiplying that area by the number of steps, Δz, in the tool path. The greater sheet thickness at the last tool position supports the initial suggestion by Shin et al. [77]. Increasing forming force is a simple indicator for material being push forward and large material accumulation leads to higher surface roughness.

3.6 Characterization of UA-TPIF microstructure

The resulting microstructure of ultrasonic assisted deformation for aluminum has been documented in a variety of tests in literature. Siu et al. [80] performed UA indentation tests using a Vickers's indenter and noted a larger deformed area and greater sub-grain formation. Zhou et al. [66] conducted UAC on commercially pure aluminum and found a higher fraction of low-angle grain boundaries near the specimen-platen interface. Deshpande and Hsu [39] compressed

commercially pure aluminum wire using increasingly higher amplitudes; their microstructural analysis shows higher sub-grain size which the authors attributed to dynamic recrystallization. A more recent study from Cheng et al. [35] also confirmed an increase in grain size after UA-ISF of commercially pure aluminum. This section aims to characterize the microstructure after UA-TPIF.

3.6.1 Experimental setup and methods

Initial efforts were to characterize the AA2024-O samples after TPIF; however, due to the significant density of precipitates and large grain structure, the microstructure gathered using EBSD method struggled with confidence index (CI) distortion near precipitates and grain size evolution was impractical at a low scanning step size required to quantify low angle misorientation information with high fidelity. Therefore, commercially pure AL 1100-O series purchased from McMaster Carr was formed using UA-TPIF. The experimental parameters are listed as follows: $t_0 = 1.60mm$, $\alpha = 45°$, $t_d = 12.7mm$, $F = 42mm/s$, $\Delta z = 0.25mm$, $SF_p = 25\%$, and vibration amplitude $\lambda = 2.8\mu m$.

EBSD technique was used to characterize the aluminum microstructure in the undeformed, no UA, and UA regions. Cross sections were cut using an electric discharge machine (EDM). The cut surface corresponds to the transverse and normal directions ($TD \perp ND$) relative to the rolled texture. To prep the surface for EBSD, the samples were mounted in epoxy, ground from P800, P1200, P2400, P4000 European grits, and polished using 3µm and 1µm diamond suspensions. Final polish was performed using MasterMet2 colloidal silica, 0.02 µm particle solution in the vibratory polisher for 30mins. A Tescan Mira equipped with a EDAX Velocity collector was used to acquired microstructural information. The operating voltage and working distance were set to 25kV and 25mm and the step size was set to 0.5µm. The collected data was later processed in OIM v8 EDAX software using the neighbor pattern averaging and reindexing (NPAR) function. A post

dilation clean-up function was used to associate precipitate pixels to the neighboring grain; this clean up function alters less than 7% of points. Low angle grain boundaries (LAB) were defined as the misorientation between pixels of $2° < \theta < 15°$. High angle grain boundaries included pixels with misorientations $15° < \theta < 180°$.

3.6.2 Results and discussion

SPIF and TPIF forming force of the AL 1100-O sheet material is plotted in **Figure 3-22**. The TPIF

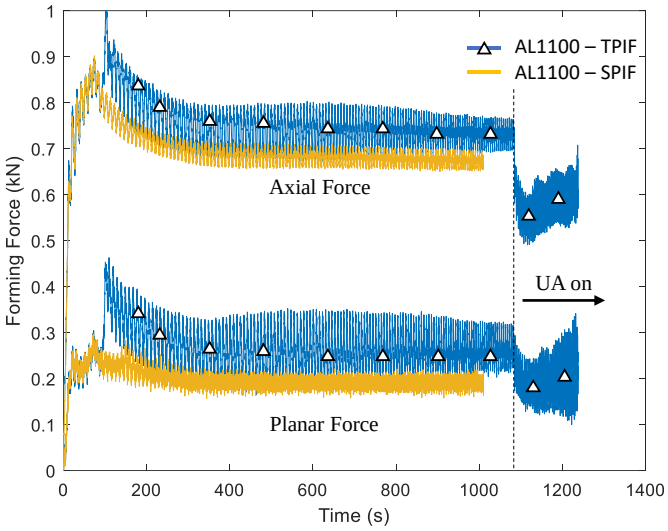

Figure 3-22 UA-TPIF forming force for Al 1100-O sheets.

sample has a slightly higher forming force in both axial and planar direction because the sheet is being squeezed. At the 1075s mark, a vibration amplitude of 2.8μm was switched on. The comparing the mining force in the UA region with the steady state axial force prior to 1075s, the ultrasonic softening was calculated to be 25.0%. The average softening within the UA window is 18.7%. The initial microstructure begins with equiaxed grains in ($TD \perp ND$) interface as shown in **Figure 3-23a**. Incremental forming compresses the grains the in through thickness axis and stretches the grains in the TD axis (which is the meridional direction or forming direction in ISF) as shown in **Figure 3-23c**; the ultrasonic assisted region shows a similar microstructure and does

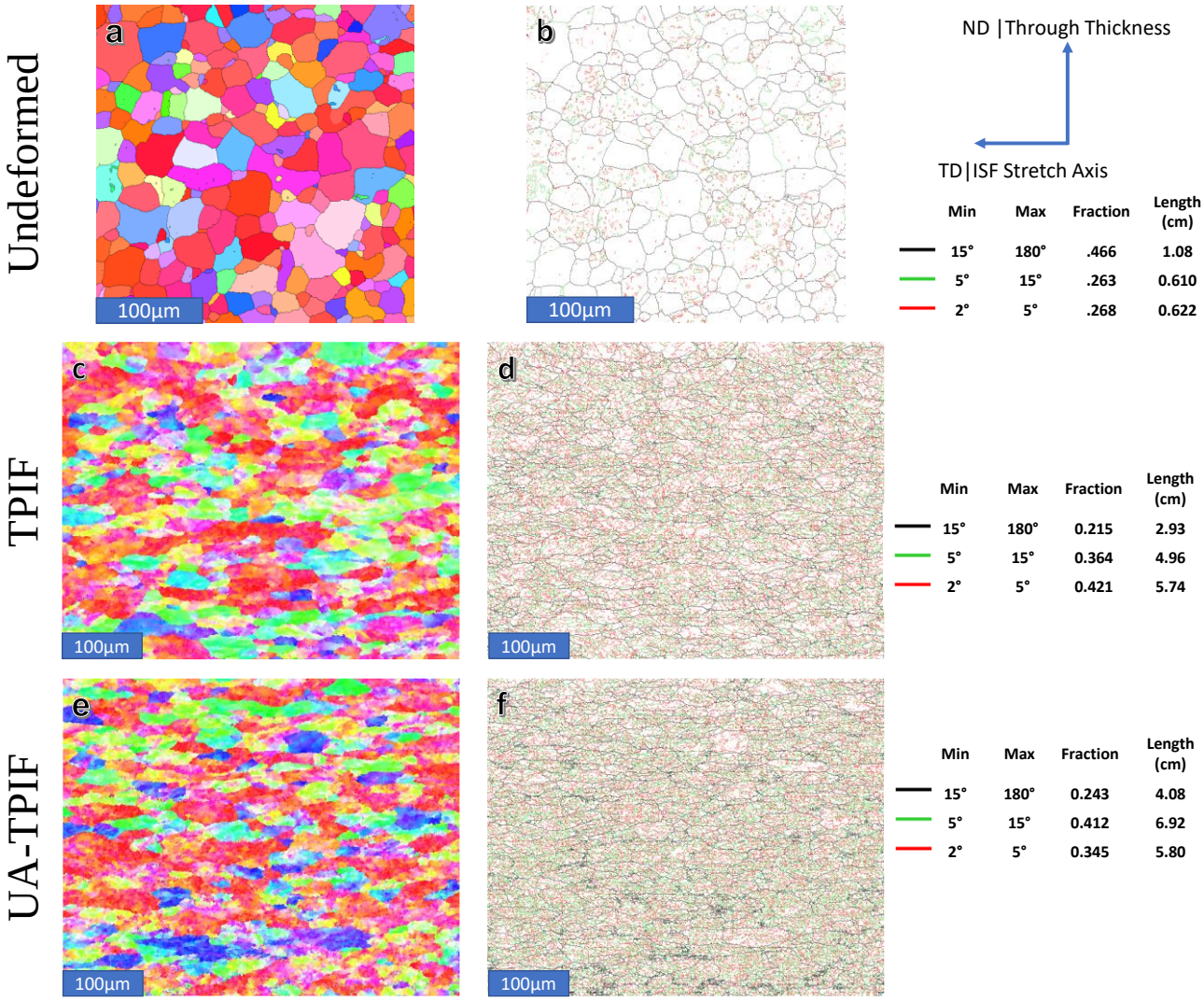

Figure 3-23 Microstructure of undeformed (top row), TPIF (middle row), and UA-TPIF (bottom row) samples. a,c,e) IPF maps and b,d,f) rotation angle misorientation maps of each sample respectively

not appear to have significant grain growth mode of dynamic recrystallization as reported by [49]. The misorientation map in **Figure 3-23b** indicates minimal low-angle grains boundaries (LAGB) in the undeformed sample. As the material is deformed, LAGB fraction increases to reduce the stored strain energy by grouping geometrically necessary dislocations (GNDs). The total length scale measured between $2° < \theta < 15°$ is greater in the UA-TPIF sample compared to the TPIF sample. This confirms the reports found in literature for aluminum alloys. The grain size reported in **Figure 3-24a** indicates a slightly higher number fraction of smaller grains; there is a potential to pinch off smaller grains from the high strain of the ISF process. The misorientation angle used

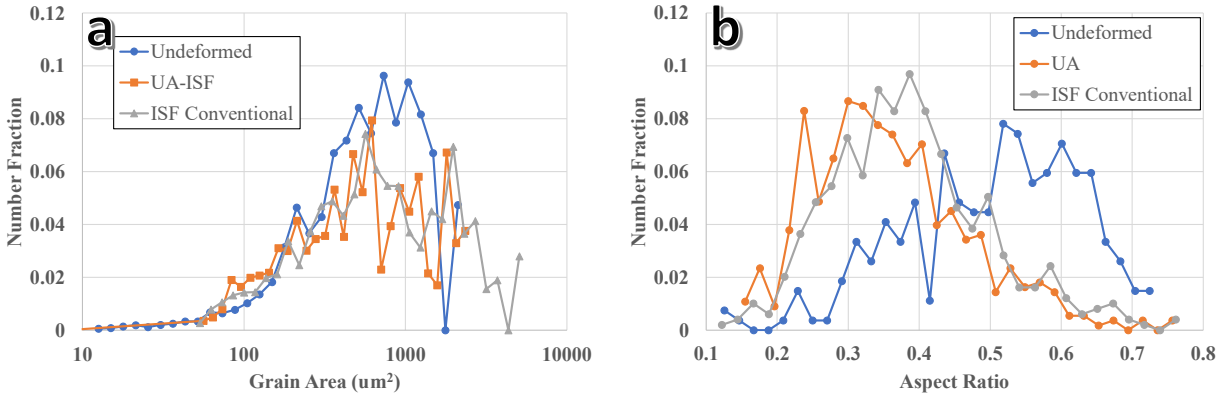

Figure 3-24 Microstructural characteristics of ISF samples. a) grain area and b) grain aspect ratio

for these calculations was 7°; based on the initial microstructure, the 7° criteria was determined to be the most appropriate to segment the low misorientation angled but distinct grains. Analysis was also conducted at higher misorientation criteria of 15° but the trend remained the same; no distinct recrystallization or grain growth was observed in either UA or non-UA ISF conditions. The grain aspect ratio, shown in **Figure 3-24b**, is indicative of the higher elongation and thus low aspect ratio in ISF [58].

Figure 3-25 shows pole figures for each sample. In all samples, a heavy cube texture $(001)[0\bar{1}0]$ is present. The ultrasonic softening effect did not change the texturing significantly; although the texture intensity for the UA-TPIF sample, **Figure 3-25c**, appears to be weaker than the undeformed and TPIF samples. A better representation of texture is found in the ODF maps in **Figure 3-26** and reference textures for rolled aluminum in **Figure 3-26.** The cubic structure represented by the Euler Bunge angles $(\varphi_1, \phi, \varphi_2)$ are located at (45,0,45) for all three samples. Adding UA appears to retain the shear texture at (0,0,45) and increase in intensity near other shear texture points (0,60,45) & (90,55,45). These shear textures were not present in the conventionally formed ISF condition. In all conditions, S, Brass, and Copper textures were absent.

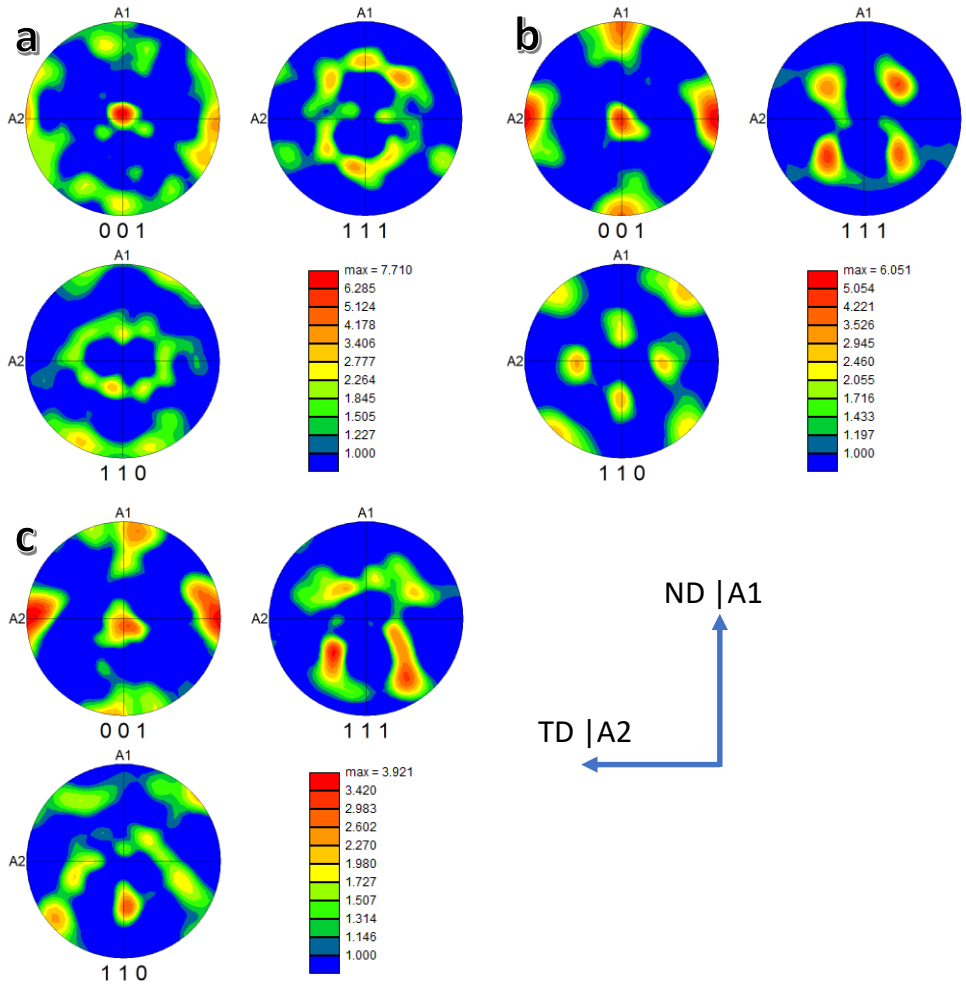

Figure 3-25 Pole figure textures for a) undeformed, b) TPIF, and c) UA-TPIF samples

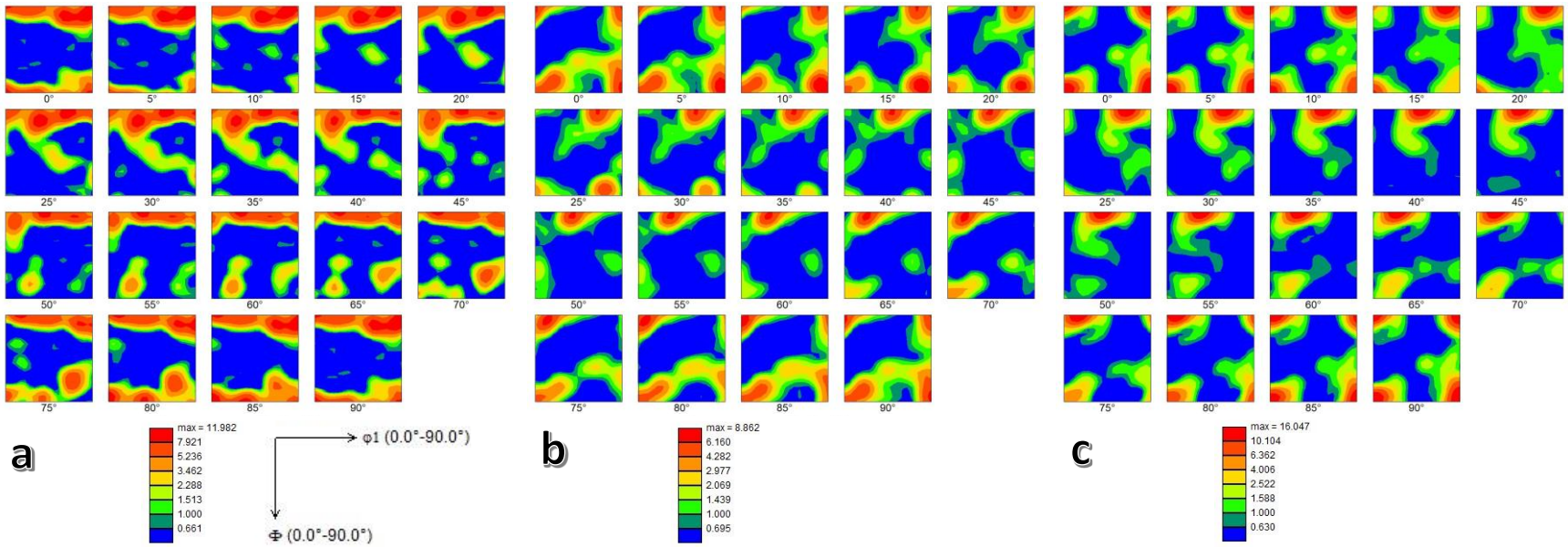

Figure 3-26 Orientation distribution function (ODF) representation of texture. a) undeformed Al 1100-O, b) UA compressed, c) equivalent strain no-UA compressed sample.

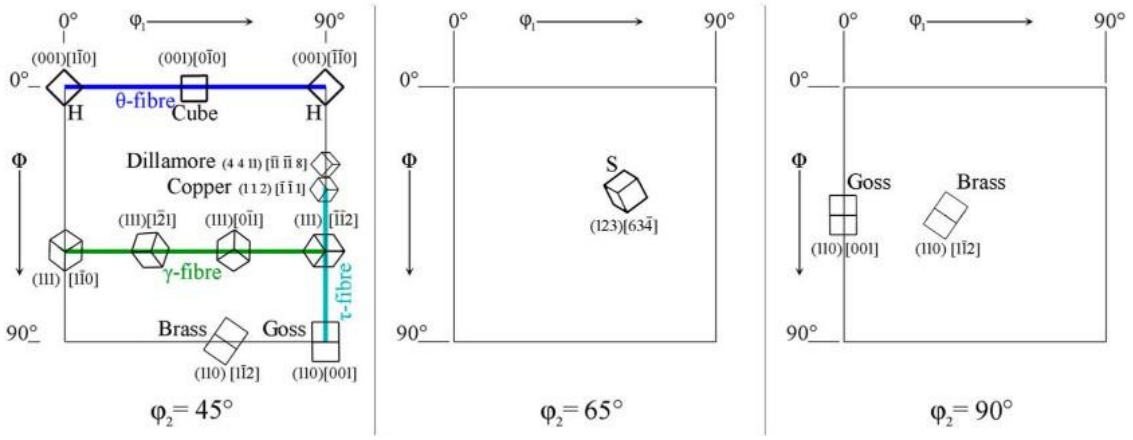

Figure 3-27 ODF reference of common rolling textures found in FCC metals

3.7 Summary and conclusions

The incorporation of ultrasonic vibration in ISF reported in this section. Ultrasonic metal forming in the literature noted both beneficial softening and reduced friction conditions in a variety of ultrasonic assisted processes. Both softening and reduced friction was observed in UA-SPIF and UA-TPIF configurations. The minor softening effect in UA-SPIF was attributed to excessive elastic vibrations due to the free hanging sheet and setup parameters such as binder opening diameter and geometry. These conditions make UA-SPIF challenging as each unique geometry and setup requires modal analysis. UA-TPIF results showed greater promise with initial experiments having an average softening of 11-18% in the axial force and 15-16% in the planar force. With parametric analysis of tool path parameters and amplitude, the largest achieve softening rate was increased to ~27%. Feed rate and programmed squeeze had minor effects on the ultrasonic softening magnitude; the ultrasonic softening magnitude was instead more sensitive to changes in step size and tool diameter. A change from 0.25mm step size to 0.40mm step size led to a decrease of 4-5% in AA2024-O and AA7075-O alloys. The lower step size of 0.25mm resulted in a greater softening effect. The hypothesis of smaller contact area and higher energy density input was debunked by the observation of the 8.0mm tool diameter; the 0.25mm step size

and 8.0mm tool diameter part showed the lowest ultrasonic softening effect. We hypothesized the change in deformation mode, distribution of amplitude due to the curvature of the tool, and size effect as potential causes; these hypotheses are addressed in Chapter 5. Under certain step size, programmed squeeze, and amplitude conditions, high material movement or flow into the center of the sheet is observed; this can create a geometric defect called a bulge and worsen the surface roughness. On the other hand, at a net zero material movement condition, the surface roughness can be improved with ultrasonic assistance. The microstructural analysis of Al 1100-O confirmed reports of greater LAGB fractions by formation of sub-grain boundaries but the significant grain growth from dynamic crystallization route was not observed. After TPIF and UA-ISF of Al1100-O samples, the texture remained a cube texture and the difference between the non-UA and UA samples were minor.

CHAPTER 4
Application of Acoustoplasticity in Compression Tests

4.1 Introduction

The previous chapter demonstrated the capabilities of using ultrasonic softening in a multi deformation state process like incremental forming. However, the literature lacks information on the commercial alloys AA2024-O and AA7075-O; thus, **Figure 4-1** compares the UA-TPIF results to ultrasonic assisted compression results from [38,66,70]. The reported softening effect varies significantly relative to the applied amplitude and the maximum reported softening effect reaches well into the 60% range. This poses a few questions: 1) why are the softening effects so broad even when the alloy grade is the same commercially pure aluminum (1xxx), 2) what is expected softening capabilities for commercial grade aluminum alloys, and 3) is UA-TPIF confined into its range due to the nature of the forming process? The work presented in this chapter seeks to provide some answers to these questions.

This chapter begins with establishing the amplitude softening response for aluminum alloys 2024-O and 7075-O and comparing them to UA-TPIF. Afterwards, we conduct a critical analysis of the experimental conditions reported in literature; we investigate the dependence of sample

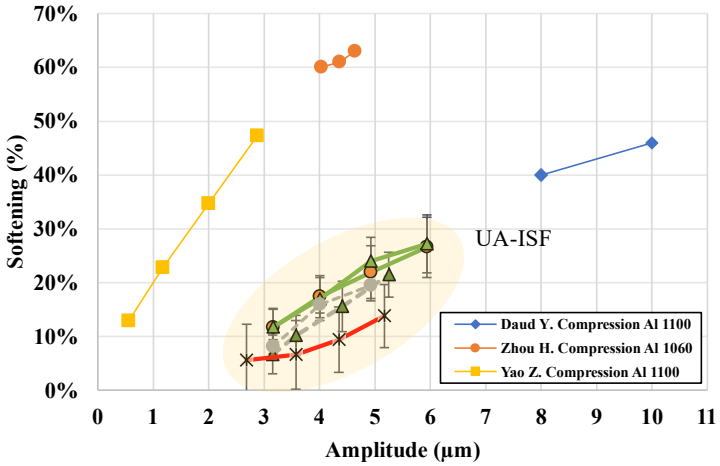

Figure 4-1 Comparison of reported softening in literature and UA-TPIF softening

volume to common acoustic terms like acoustic stress, energy, and intensity. A new parameter, amplitude strain, is introduced as the key corollary to the softening trend as opposed to existing acoustic terms. A comparison of microstructure follows; a UA and control sample of equal plastic strain are compared using EBSD technique. The chapter concludes with an analysis of the implications for contact dependent deformation processes where non-uniformity in strain is present.

4.2 Ultrasonic assisted compression (UAC)

The motivation of this section is to understand the degree of softening for precipitation hardenable aluminum alloys: AA2024-O and 7075-O. Under the O-temper condition, the sheet material has been annealed to remove storage of strain energy from cold rolling operations. In this state, the precipitates do not contribute significantly to the strength of the material due to their size and particle spacing; however, it is unknown how the presence non-strengthening precipitates may influence the ultrasonic softening effect, if at all.

4.2.1 Experimental setup and methods

4.2.1.1 Materials

Two aluminum alloys, 2024-O and 7075-O were supplied by The Boeing Company for this work. No additional heat treatment was performed as the material was already annealed. The starting sheet thickness is 1.60mm and 3.18mm for the 2024-O and 7075-O materials respectively. An electric discharge machine (EDM) was used to cut the samples into their appropriate dimensions listed in **Table 4-1**.

4.2.1.2 Experimental setup

The experimental setup was performed inside a Cincinnati CNC machine using displacement control. A Kistler dynamometer 9255A was used to measure the compressive forces during loading at a sampling rate of 40Hz. The ultrasonic horn operated at a frequency of 20kHz and is powered by a Dukane generator. A Polytec OFV 3001 vibrometer controller & OFV-3038 laser was used to measure the vibration amplitude of the horn. The compliance of the setup was measured before compression experiments by loading the flat too against the Kistler dynamometer. Engineering strain calculations within this work are compliance corrected.

4.2.1.3 Ultrasonic-assisted Compression – Transient test

To provide a basis for the expected softening effect for these alloys, a transient ultrasonic application was first tested. AA2024-O samples with dimensions of 2.27mm and 1.60mm in diameter and height, respectively, were compressed using a constant cross head speed of 0.007mm/s. At roughly 0.04mm platen travel, the vibrations were switched on for the remainder of the test. The total displacement was set to 1.02mm. Samples were compressed with increasing

ultrasonic amplitudes ranging from 0.63um to 5.36um. The final specimen height was measured after unloading and the plastic strain was calculated accordingly.

Table 4-1 Compression specimen dimensions

Aluminum Alloy	Test(s)	Diameter (mm)	Height (mm)	Amplitude (um)	Volume (mm^3)
7075-O	Volume Effect & Amplitude Strain	2.27	3.18	2.99	12.85
		2.27	3.18	2.99	12.85
		2.27	1.87	2.99	7.57
		2.27	1.87	2.99	7.57
		2.27	0.88	2.99	3.56
		3.18	1.62	3.22	12.85
		3.18	1.62	3.22	12.85
		3.18	1.62	3.22	12.85
		3.18	0.96	3.22	7.61
		3.18	0.96	3.22	7.61
2024-O	Volume Effect & Amplitude Strain	2.27	1.6	0.63	6.48
				2.99	6.48
				4.87	6.48
		3		0.63	11.31
				2.99	11.31
				4.87	11.31
	Intermittent application of ultrasonic vibrations	2.27	1.6	0.63	6.48
				1.95	6.48
				2.36	6.48
				2.77	6.48
				2.99	6.48
				3.58	6.48
				3.99	6.48
				4.41	6.48
				4.87	6.48
				5.36	6.48

4.2.1.4 Ultrasonic-assisted Compression – Full UA

Ultrasonic vibrations were applied for the full compression loading of AA2024-O and AA7075-O samples listed in **Table 4-1**. Samples are first loaded to roughly 200-250N and then vibrations were switched on for the remainder of the compression test. The acquired compression force is converted to engineering stress and strain and compliance corrected. Results for the softening magnitude were taken from a strain of 0.15. The displacement rate of 0.007mm/s maintained for this set of experiments as well. The strain hardening rate was calculated for full UA compression tests defined by:

$$\theta = \frac{d\sigma}{d\varepsilon} \tag{4.1}$$

4.2.1.5 Full application of ultrasonic vibrations – modified specimen dimensions

Samples of AA2024-O and AA7075-O dimensions were varied according to **Table 4-1**. Ultrasonic vibrations were switched on at a similar compression force of 200-250N and allowed to run for the remainder of the test. The results are plotted in terms of engineering stress and strain. Acoustic softening results presented in this work were calculated at an engineering strain of 0.15 unless stated otherwise.

4.2.2 Results and Discussion

4.2.2.1 Transient application of vibrations

The stress strain curve during the transient application of ultrasonic vibrations on AA2024-O specimens is shown in **Figure 4-2**. The initial loading period up to 0.20 strain is the quasi-static loading without any ultrasonic assistance. Once the specimens reached 0.20 strain, the transducer was activated, and an immediate softening response is observed. The vibration was switched off during the unloading portion of the test. As the amplitude increases from 0.63um to 5.36um, the softening magnitude increases from 14.4% to 66.1% respectively. The softening magnitude is commonly compared to the applied vibration amplitude as shown in **Figure 4-3a**. A linear relationship to the applied amplitude was found for AA2024-O material. The unloaded specimen

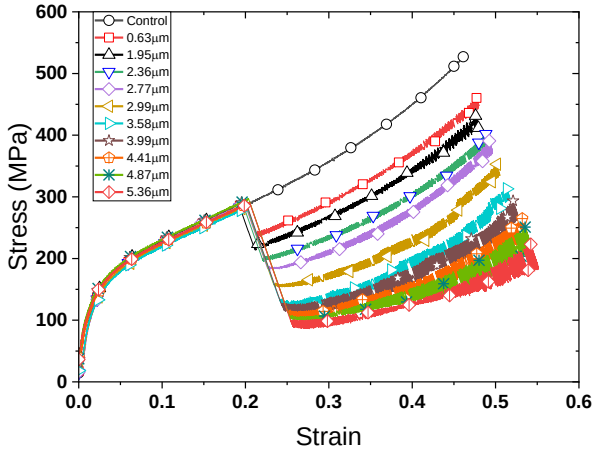

Figure 4-2 Compression of AA2024-O coupons at various ultrasonic vibration amplitudes

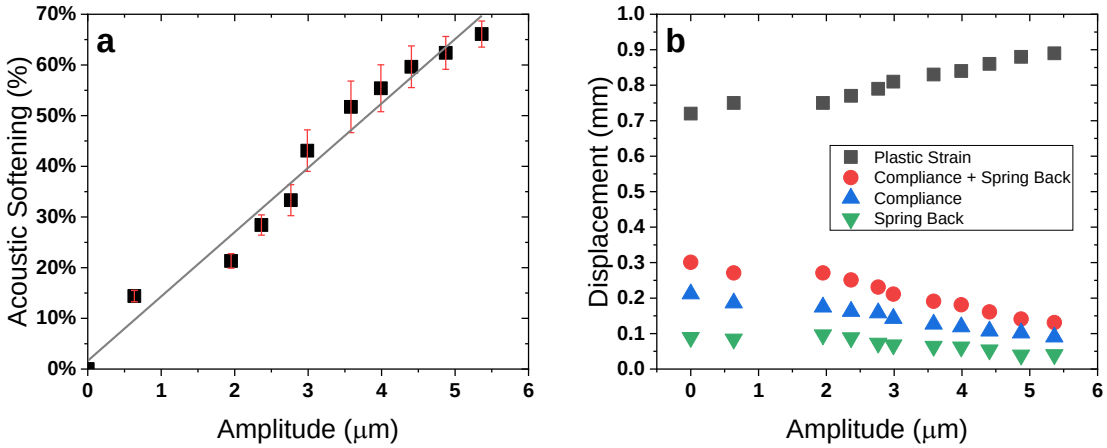

Figure 4-3 a) Acoustic softening calculated from compression testing of AA2024-O coupons. b) System compliance, plastic deformation, and sample springback compared to the applied amplitude

height was measured to characterize the plastic strain. The results, in **Figure 4-3b**, indicates higher plastic deformation of compressed samples with an increase amplitude. The results can be compared to similar load or displacement-controlled experiments in literature. Siu conducted load control indentation tests and found larger deformation areas when adding ultrasonic assistance [80]. Lum performed load and displacement-controlled ball bonding of gold and found higher plastic strains with increasing amplitudes [81]. Given the known compliance of the system and cross head travel, the sample spring back was calculated and shown to decreases with increasing amplitude. This coincides with the proposed dislocation annihilation mechanism in acoustic softening leading to a reduction in stored defect energy and thus, less resistance to slip. This effect can be observed right at the start of adding the vibrations. The drop in stress lowers the compliance of the system and deflection of the platen which would imply an immediate increase in the strain of the sample.

4.2.2.2 Full application of ultrasonic vibrations

AA2024-O specimens were first loaded to an applied force of 200-250N from which vibrations were applied for the remainder of the test. The engineering stress and strain are plotted

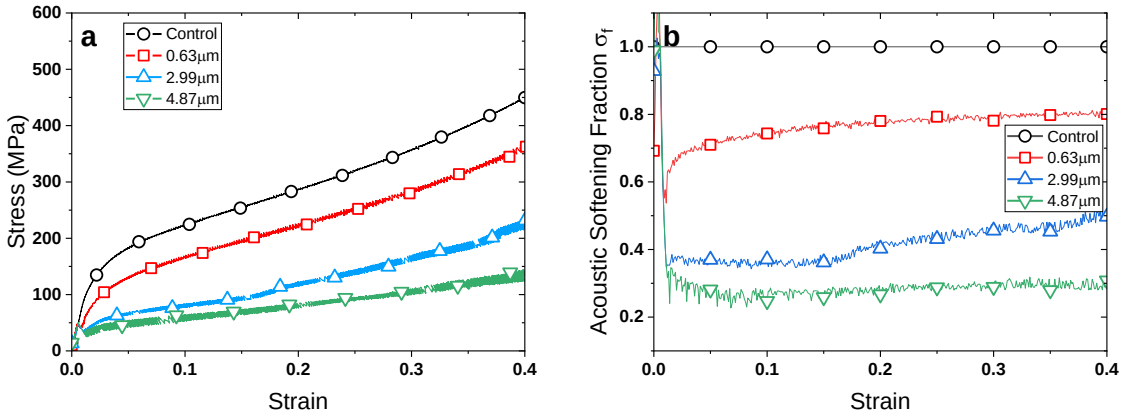

Figure 4-4 Full ultrasonic assisted compression of AA2024-O. a) Stress-strain curve and b) the corresponding acoustic softening fraction at those amplitudes

in **Figure 4-4a** for vibrations amplitudes of 0.63µm, 2.99µm, and 4.87µm. Like the transient application of UA, the softening effect has a positive correlation to amplitude. The softening ratio plotted in **Figure 4-4b**. At initial strains, the softening effect is maximum and decreases as the sample is strained further. Since acoustoplasticity is known to change the resulting microstructure, potentially leaving a residual hardening or softening effect, a similar argument can be made about the specimen state of strain influencing the softening magnitude. During the early stages of strain, the material deforms through multi-slip and resembles a dislocation forest like defect structure. At higher strains, these dislocations coalesce into lower energy defect structures such as subgrains which has been documented in the deformation of aluminum using UA [80]. The results suggest the internal defect structure at higher strains benefits less from the acoustic softening phenomenon or possibly impeding the effect because of higher attenuation.

The strain hardening rate, **Figure 4-5**, of the control sample and 0.63µm sample are similar. Raising the amplitude to 2.99µm shows a slight decrease in the strain hardening rate and an even greater decrease with the 4.87µm sample. Most literature reports do not specify the strain hardening rate during UA, however, the work of Zhou et al. [66] provides insight into residual effects after turning vibrations off. Zhou performed UA compression tests on commercially pure

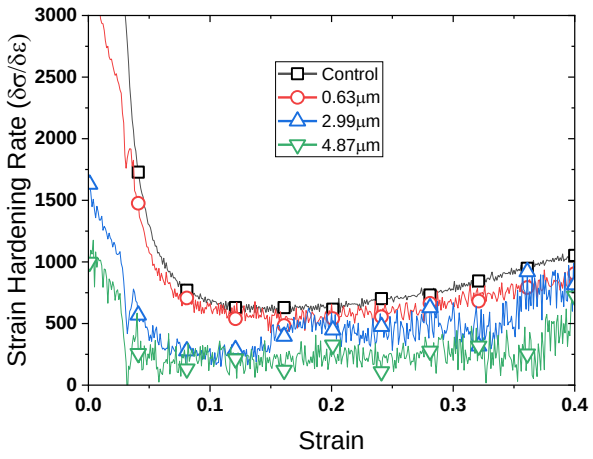

Figure 4-5 Strain hardening rate of full ultrasonic assisted compression specimens.

aluminum with an amplitude of 4.65μm for different time and strain durations. Their work showed residual hardening is possible after 24s or roughly 0.093 strain. Shorter times with UA excitation showed no changes in residual hardening and longer times led to greater hardening effects. Therefore, depending on either the time duration or strain under UA, the internal defect structure becomes distinct from the quasi-static loading sample. From this work, the 4.87μm applied amplitude led to permanent changes in internal defect structure leading to a significant change in strain hardening behavior. Changes in strain hardening rate might be a precursor to residual hardening effects which are commonly reported for commercially pure aluminum after high ultrasonic input [70].

4.2.2.3 Effect of specimen volume on acoustic softening

AA2024-O and AA7075-O compression specimens were cut to a variety of dimensions listed in **Table 4-1**. Full UA application was implemented for these tests. The acoustic softening magnitude, $\Delta\sigma$, was calculated at a strain of 0.15 and plotted in **Figure 4-6** for comparison. In all cases, a reduction in specimen volume resulted in a greater softening response. This reaffirms the initial report by Zhou [66]. Increasing the vibration amplitude from 2.99um to 3.22um, increased the softening effect for the same volume as expected.

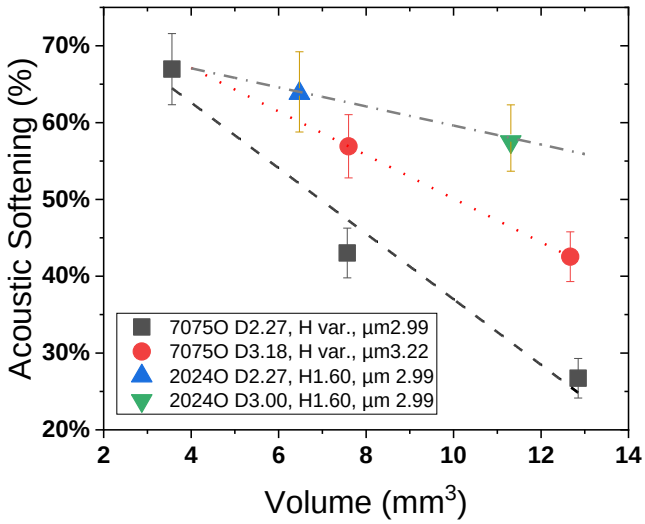

Figure 4-6 Ultrasonic assisted compression of AA2024O and AA7075O alloys grouped by their dimensions and volumes

Given the influence vibrations have on friction conditions, termed surface effects, the results for the 3.18mm diameter AA7075-O sample could be exhibiting greater softening due to lower friction conditions [39]. To demonstrate the impact of a change in diameter, two AA2024-O samples of the same height and different diameters were tested. The larger diameter sample showed a smaller softening magnitude. Thus, the higher softening response for the 3.22um data set are primarily driven by softening in the bulk of the sample.

Based on the trendline from **Figure 4-3a**, increasing the vibration amplitude from 2.99µm to 3.22µm should improve the softening effect by roughly 5.0%. When comparing the response for the 7075-O alloy in **Figure 4-6**, the softening improved 15.8% under equivalent sample volume of 12.5mm^3. As the sample volume decreases, the trendlines between the 2.99µm and 3.22µm data sets appear to converge instead of being equidistant. From an energy perspective, as the sample volume decreases, the acoustic energy density reaches a critical point which defines an upper limit of acoustoplasticity. The softening response of these sample sets are plotted relative to common acoustic parameters such as acoustic energy, intensity, or stress based on Eq. 2.4-6. The acoustic energy density and acoustic stress, **Figure 4-7a** and **Figure 4-7b** respectively, are invariant to the

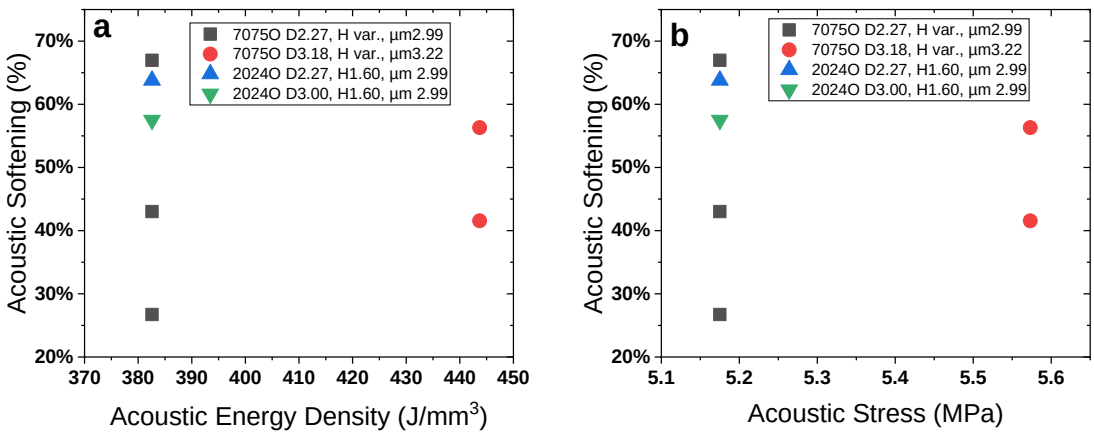

Figure 4-7 Acoustic softening of AA2024-O and AA7075-O specimens at 0.15 strain. a) acoustic energy density (refer to Eq. 3) and b) acoustic stress (refer to Eq. 5).

changes in sample dimensions as indicated by a vertical trend. The acoustic intensity was not plotted here because the results would be similar to acoustic energy density as $I \propto \lambda^2$.This is a possible explanation for large variations in acoustic softening reported in literature. For example, Yao observed softening percentages up to 35% with a 2µm amplitude while Aziz required an amplitude of 20µm to achieve 32% softening [70]. Their commercially pure aluminum sample heights were 2mm and 8mm for Yao and Aziz experiments respectively [32,70]. Although their samples may differ in microstructure, the sample set presented in this work were machined from the same sheet. The main difference that delineates a greater response is the sample dimensions. Here, we propose a parameter called amplitude strain which accounts for changes in the specimen height during compression testing. The amplitude strain is represented as:

$$\tilde{\lambda}_{\varepsilon} = \frac{\lambda}{\mathrm{h}_{\varepsilon}} \tag{4.2}$$

where the amplitude strain $\tilde{\lambda}_{\varepsilon}$, is the applied amplitude λ, divided by the height of the specimen h_{ε}, at a given strain. The $\tilde{\lambda}_{\varepsilon}$ parameter, calculated at a specimen strain of 0.15, was plotted in **Figure 4-8** and showed a linear fit across sample sets of different dimensions. The results were further divided into their respective alloys in **Figure 4-9a** and still maintained a close correlation.

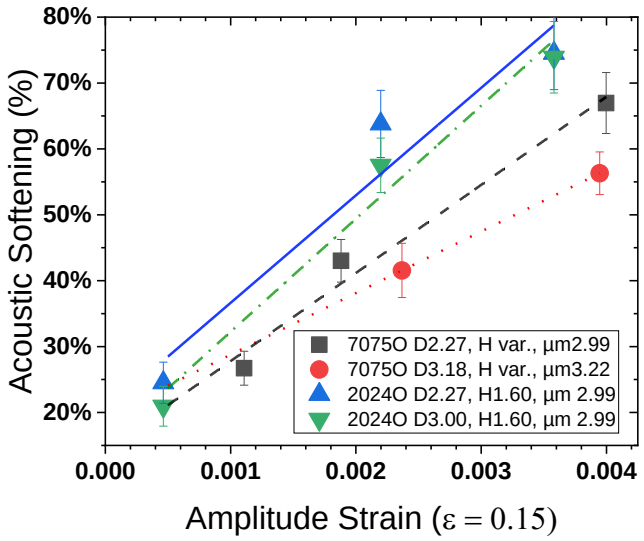

Figure 4-8 Acoustic softening response compared to the amplitude strain parameter

Incorporating the strain of the specimen is necessary based on **Figure 4-9b**. As the material stores more internal defects, the microstructure hinders the beneficial effects of acoustoplasticity. This trend was found to be true for the 0.63um and 4.87um samples as well however, the spread in response was not as large as the 9% difference in **Figure 4-9b**. AA2024-O samples with 0.63um and 4.87um applied amplitudes both showed a spread of ~5% comparing values at 0.15 and 0.35 strain. An interesting aspect to note is the non-zero Y-intercept when extrapolating the results in **Figure 4-9**. This a deviation from the trend in **Figure 4-3a**. One distinction between these data

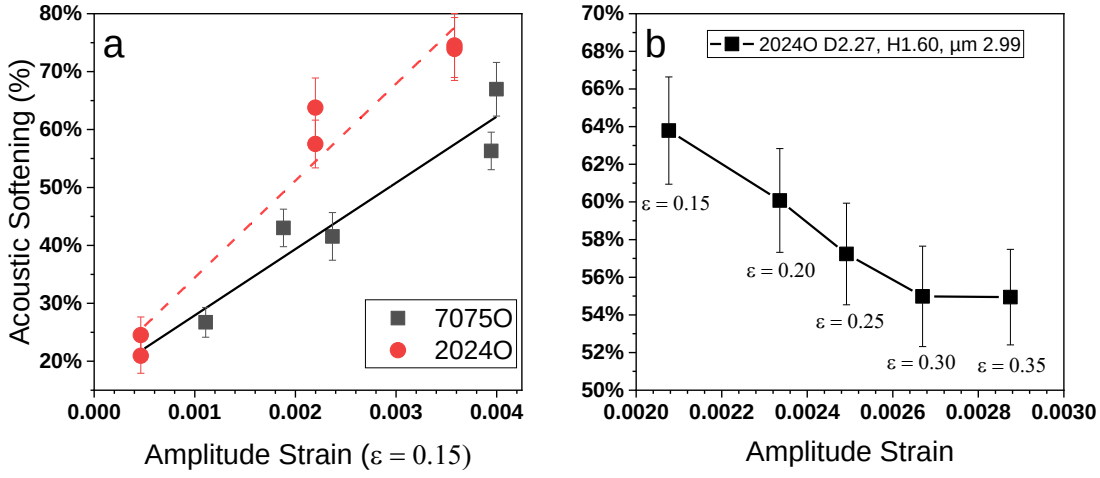

Figure 4-9 Ultrasonic assisted compression of AA2024O and AA7075O alloys. a) grouping based on alloy type. b) acoustic softening percent calculated at different engineering strains from a AA2024-O full ultrasonic assisted compression test.

sets is that the full UA samples are subjected to microstructure changes throughout the compression process while **Figure 4-3a** is the immediate response at the strain state. Addition points were calculated from the full UA sample set and shown in **Figure 4-10**.

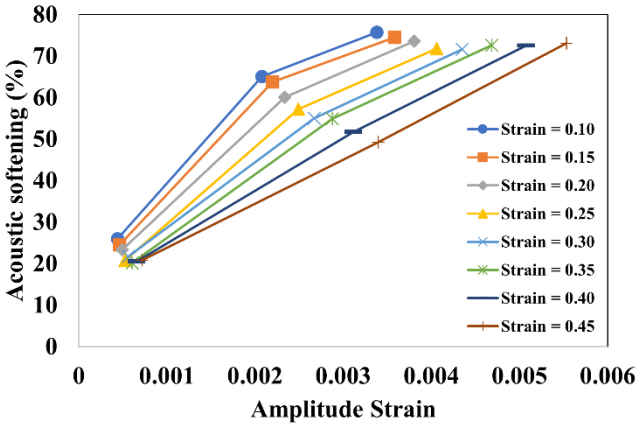

Figure 4-10 Amplitude strain point collected from full UA sample set

At all states of strain, a linear fit would result in a non-zero intercept. However, a simple argument would be that the real trend is not linear but a 3D surface correlating the amplitude strain and strain state. Increasing the sample set is recommended as future work. The samples would not need to be polish down to certain heights; instead, the amplitude would be the variable.

4.2.2.4 Incorporating amplitude strain in existing acoustoplasticity models

Results from **Figure 4-6** supports the notion of higher acoustic energy input leading to greater softening effects. However, the invariance in acoustic energy density and stress terms imply that the terms are not representative, and that softening is driven by another experimental factor: amplitude strain $\tilde{\lambda}_{\varepsilon}$. This new finding provides some clarity on the wide range of softening responses reported in literature and can be incorporated in crystal plasticity and dislocation evolution models commonly used in the community. Yao used a dislocation density model and introduced a stress reduction ratio $\Delta\lambda$ [70]:

$$\Delta\lambda = -\beta\left(\frac{E}{\hat{\tau}}\right)^{m} \tag{4.3}$$

where $\hat{\tau}$ is the critical resolved shear stress required for slip, E is the acoustic energy density (Eq. 2.4), and β and m are experimental fitted parameters. Based on their UAC experiments, a value of 0.5 was fitted for m which suggests a linear correlation to amplitude. To obtain the shear stress under ultrasonic assisted conditions:

$$\tau_{UA} = \tau\left[1 - \bar{\lambda}\right] = \tau\left[1 - \chi \cdot \tilde{\lambda}_{\varepsilon} + C\right] \tag{4.4}$$

where χ refers to the slope of the amplitude strain plot in **Figure 4-8**, $\tilde{\lambda}_{\varepsilon}$ is the amplitude strain, and C is equivalent to y-intercept in **Figure 4-8**. $\bar{\lambda}$ is equal to $\chi \cdot \tilde{\lambda}_{\varepsilon} + C$. This is a simple phenomenological model for determining the stress under ultrasonic assistance. Yao et al. [70] connected the change in shear stress through dislocation storage and dynamic recovery terms based on these equations:

$$\hat{\tau} = \tau_0 + \mu a b\sqrt{\rho} \tag{4.5}$$

$$\frac{d\rho}{d\gamma} = k_1\sqrt{\rho} + k_2\rho \tag{4.6}$$

where τ_0 and α are material parameters, b is the burgers vector, μ is the shear modulus, and ρ is the dislocation density term. k_1 and k_2 are the dislocation storage and recovery terms respectively. In crystal plasticity models, the critical resolve shear stress is similarly modified to represent softening by the shear strain rate equation [73]:

$$\dot{\gamma}^{\alpha} = \dot{\gamma}^{0} sgn(\tau^{\alpha})\left\{\frac{\tau^{\alpha}}{\hat{\tau}^{\alpha} \cdot U_{soft}}\right\}^{n} \tag{4.7}$$

$\dot{\gamma}^0$ is the pre-exponential factor or frequency factor, τ^α is the resolved shear stress on a slip plane, $\hat{\tau}^\alpha$ is the critical resolved shear stress, and U_{soft} is the acoustic softening parameter. Siddiq wt al. [73] represented the U_{soft} by:

$$U_{soft} = (1 - d_{ut} \cdot I_{ultrasonic})^{e_{ut}} \tag{4.8}$$

d_{ut} and e_{ut} are experimentally fit parameters and $I_{ultrasonic}$ is the acoustic intensity (Eq. 2.5). Similarly, U_{soft} can be replaced by $1 - \bar{\lambda}$ to represent the change in critical slip resistance.

Aside from reducing the activation energy required for slip, others have suggested a change in the pre-exponential factor $\dot{\gamma}^0$ or the bypass attempt frequency to be significant in driving the acoustic softening effect [70,80]. Discrete dislocation simulations from Siu and Cheng suggested that during the unloading portion of the vibration, dislocations are allowed to travel in reverse motion spurred by the relief of applied stress and dislocation-dislocation interactions [34,80]. Under combined forward and reverse motion, the dislocations are possibly interacting with complementary dipoles for annihilation or allowed to cross slip in search annihilation sites. Considering this framework of relative strain as the driver of softening magnitude, the necessity of using efficiency and compensation coefficients in more complex ultrasonic assisted forming processes arise from variability in amplitude strain distribution. Press forming and incremental forming, demonstrated by the models from Sedaghat, have inherent strain gradients and a distribution of $\tilde{\lambda}_\varepsilon$ in each element [72]. Further work on modeling deformation processes with a strain and $\tilde{\lambda}_\varepsilon$ distribution is worthwhile.

4.3 Microstructural characterization of UAC samples

In this section, we seek to characterize the microstructure of UAC aluminum samples and compare with the findings in literature. As stated in chapter 3, there are specific challenges in

EBSD of AA2024 material; therefore, this section conducts UAC on commercially pure aluminum 1100-O.

4.3.1 Experimental methods

Compression experiments were again conducted in the Cincinnati HMC 400 EP CNC machine. A Kistler dynamometer 9255A was used to measure the compressive forces during loading at a sampling rate of 40Hz. The ultrasonic horn operated at a frequency of 20kHz and is powered by a Dukane generator. An amplitude of 3.00µm was used in these compression experiments and the strain was calculated by dividing the final, unloaded specimen height by the initial height of 1.60mm. There were three conditions selected for UAC of AL 1100-O. In the first condition, the sample was strained using conventional, quasi-static loading to a set displacement, d. The second condition replicated the quasi-static loading to position d followed by a hold at position d; a vibration amplitude of 3.00µm was applied for a short duration of 30s under this hold position. A longer vibration hold of 60s was performed and no distinct change in force was observed. The third condition consists of quasi-static loading until the final height of the specimen match the UA sample. The measured final height divided by the starting sample height was interpreted as the strain in this experimental work.

In preparation for EBSD, samples were cold mounted in epoxy with the $TD \perp ND$ plane facing outward. Samples were ground from P800, P1200, P2400, P4000 European grits, and polished using 3µm and 1µm diamond suspensions. Final polish was performed using MasterMet2 colloidal silica, 0.02 µm particle solution in the vibratory polisher for 30mins. A Tescan Mira equipped with a EDAX Velocity collector was used to acquired microstructural information. The operating voltage and working distance were set to 25kV and 25mm and the step size was set to 0.5µm. The collected data was later processed in OIM v8 EDAX software using the neighbor

pattern averaging and reindexing (NPAR) function. A post dilation clean-up function was used to associate precipitate pixels to the neighboring grain; this clean up function alters less than 7% of points. Low angle grain boundaries (LAB) were defined as the misorientation between pixels of $2° < \theta < 15°$. High angle grain boundaries included pixels with misorientations $15° < \theta < 180°$.

4.3.2 Results and discussion

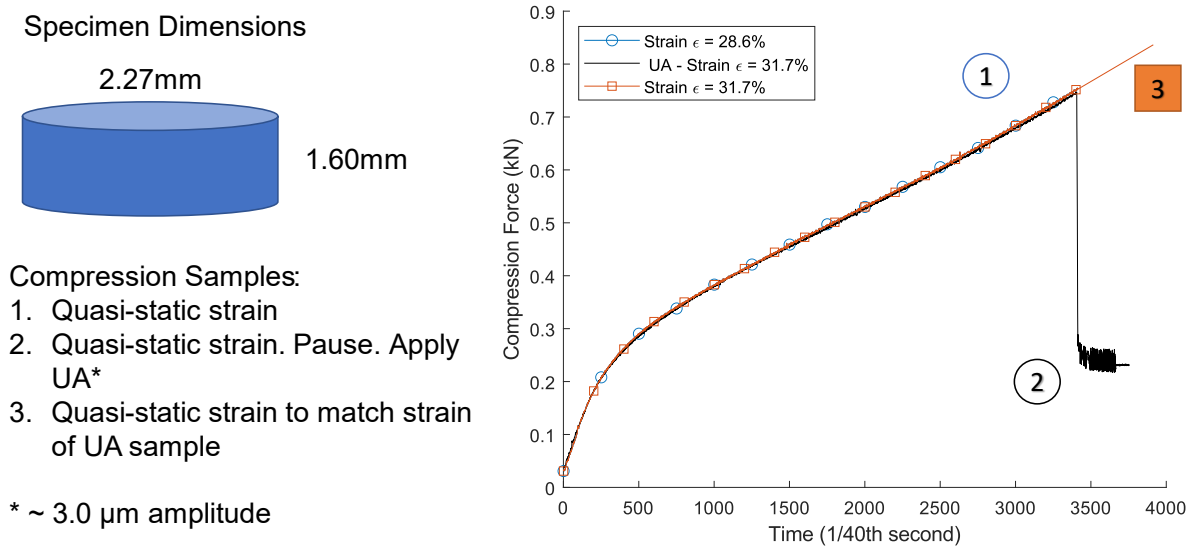

Figure 4-11 Compression forces of AL 1100-O

The force plot of the three conditions is shown in **Figure 4-11**. In each sample, the force vs displacement curves are in close agreement and support the repeatability of the experimental setup. In the UA condition, the applied vibrations led to a large force drop from 747N to 230N which equates to a 69.2% difference. The plastic strain measure after unloading the sample from the 1st condition was 28.6%; the ultrasonic vibrated sample in the 2nd condition increased the plastic strain by 3.1% to 31.7%. This supports the dislocation dynamic (DD) simulations from Siu et al. [78]; they modeled the change in dislocation density based on combinations of static stress and vibration input. Based on their DD simulation, a reduction is possible with a static stress lower than the yield strength of the material. In this 2nd condition, the sample is technically right at the yield point and thus, a much larger drop in force is observed. Once the beneficial softening has

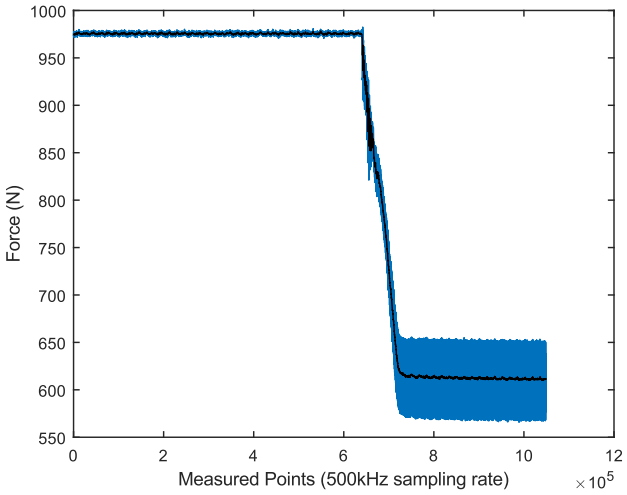

Figure 4-12 High sampling frequency 500kHz of vibrated compression sample

reached a plateau, the vibration of the sample is shown by the sinusoidal response in the compressive force. Although the sample rate here is 40Hz, in a separate experiment, a 500kHz was used to measure the change in force of a loaded sample as shown in **Figure 4-12**. The sinusoidal response, after the softening has stabilized, does not peak at the started force; this suggests a permanent change in the material properties and supports previous journals dismissing the stress-superposition principle as the cause for softening.

The microstructure of the undeformed material, **Figure 4-13**, shows an equiaxed grain structure. After compression, the grains are elongated and compressed in the TD & ND directions respectively. Rotation angle misorientation maps are plotted in **Figure 4-14**. The undeformed microstructure shows well defined grain boundaries with minimal interior grain misorientations; an expected condition for the O-temper aluminum. Comparing the misorientation maps, **Figure 4-14b** and **c**, the UA sample shows a greater LAGB length and fraction compared to the quasi-static strained specimen; this confirms the reports in literature of enhance subgrain formation in aluminum. The kernel average misorientation (KAM) is another microstructural feature that

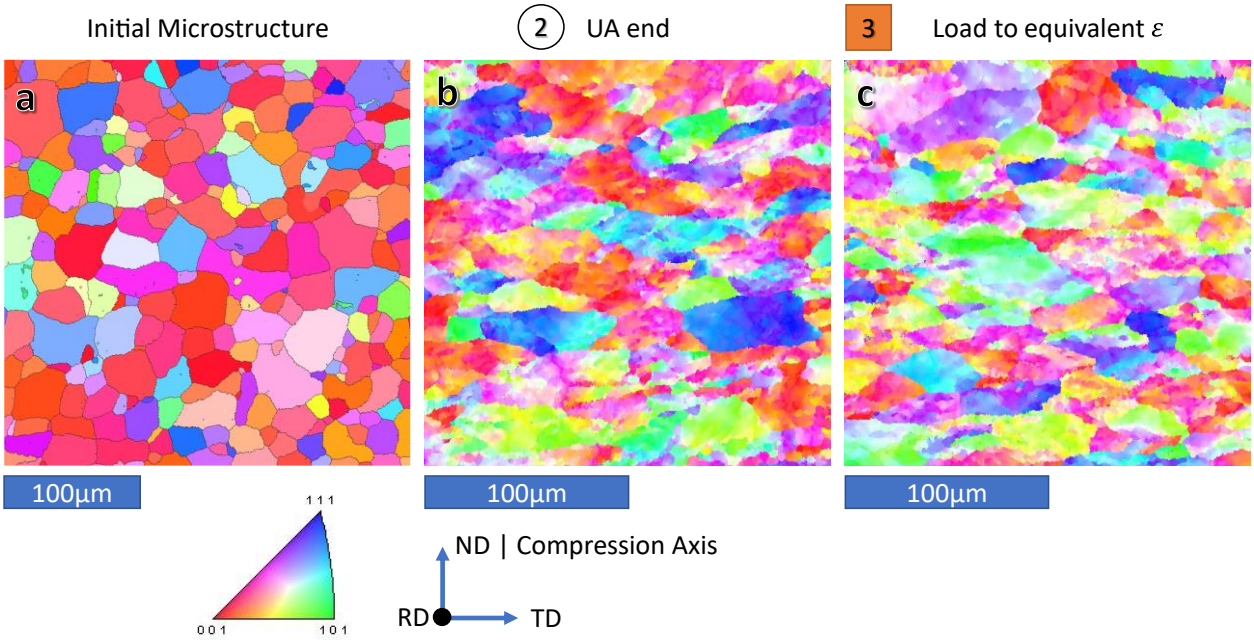

Figure 4-13 Inverse pole figures of AL 1100-O in a) undeformed, b) UA sample, and c) conventional quasi-static load to the same equivalent strain

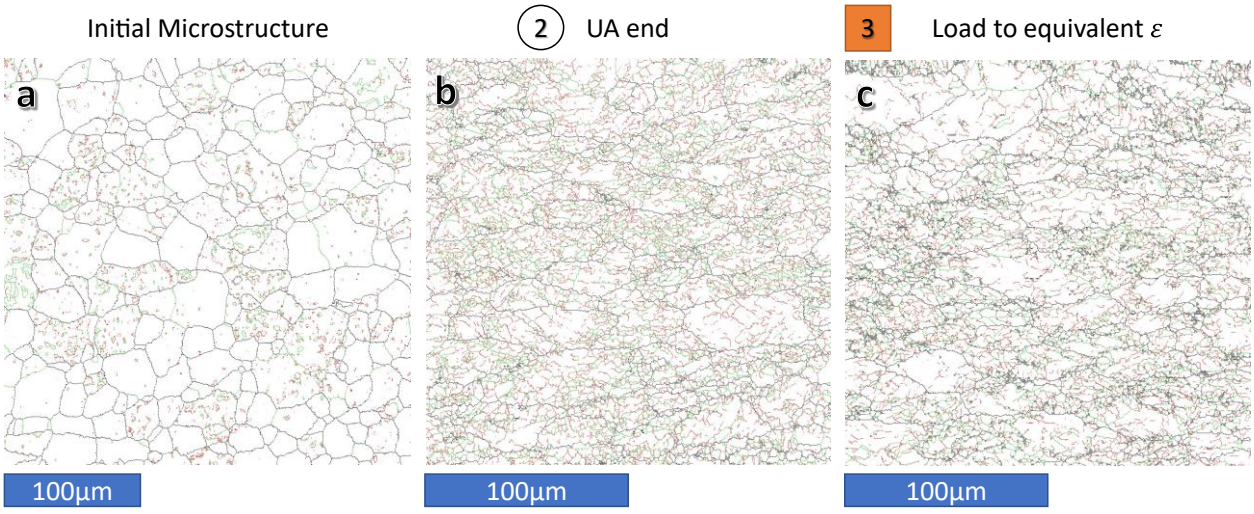

	Min	Max	Fraction	Length (cm)
—	15°	180°	.467	1.08
—	5°	15°	.265	0.610
—	2°	5°	.268	0.622

	Min	Max	Fraction	Length (cm)
—	15°	180°	.243	0.829
—	5°	15°	.348	1.19
—	2°	5°	.409	1.39

	Min	Max	Fraction	Length (cm)
—	15°	180°	.405	1.40
—	5°	15°	.278	0.963
—	2°	5°	.316	1.09

Figure 4-14 Rotation angle misorientation map of AL 1100-O in a) undeformed, b) UA sample, and c) conventional quasi-static load to the same equivalent strain

provides a sense of the misorientation between neighboring pixels; in this analysis, the kernel size was set to nearest neighbors of 1 and the results is plotted in **Figure 4-15**. From KAM, the GNDs can be calculated and is shown in **Figure 4-16**. The greater intensities in the KAM and GND maps support the notion greater subgrain boundaries and GNDs for the UA sample even at the same strains.

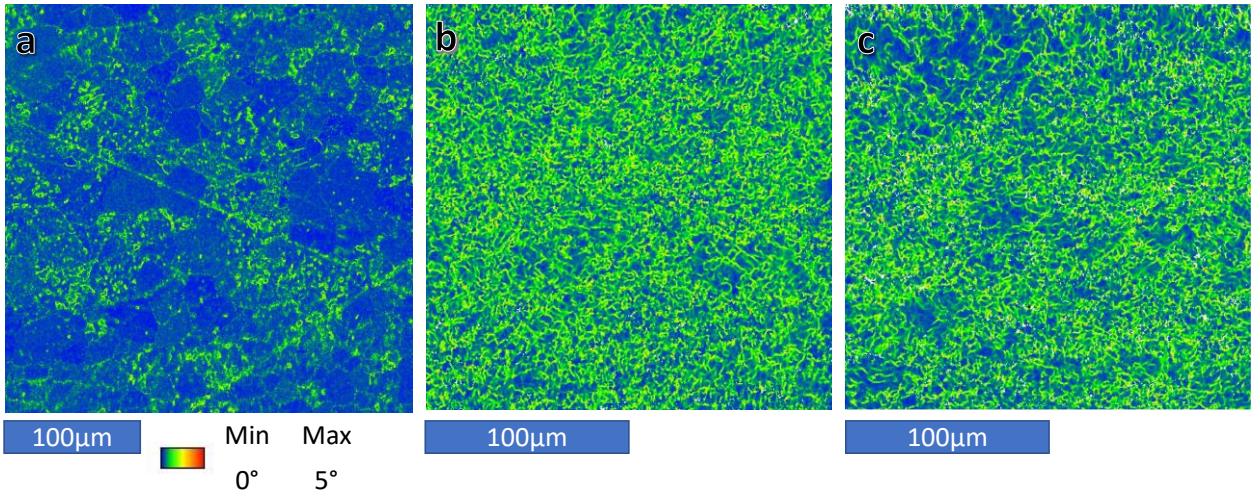

Figure 4-15 KAM maps of AL 1100-O in a) undeformed, b) UA sample, and c) conventional quasi-static load to the same equivalent strain

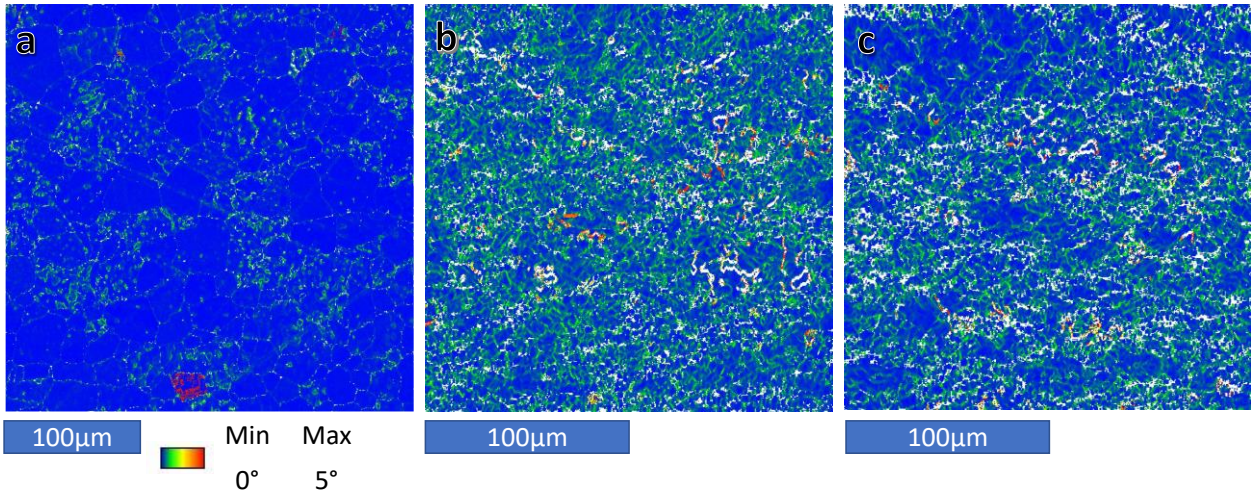

Figure 4-16 GND maps of AL 1100-O in a) undeformed, b) UA sample, and c) conventional quasi-static load to the same equivalent strain

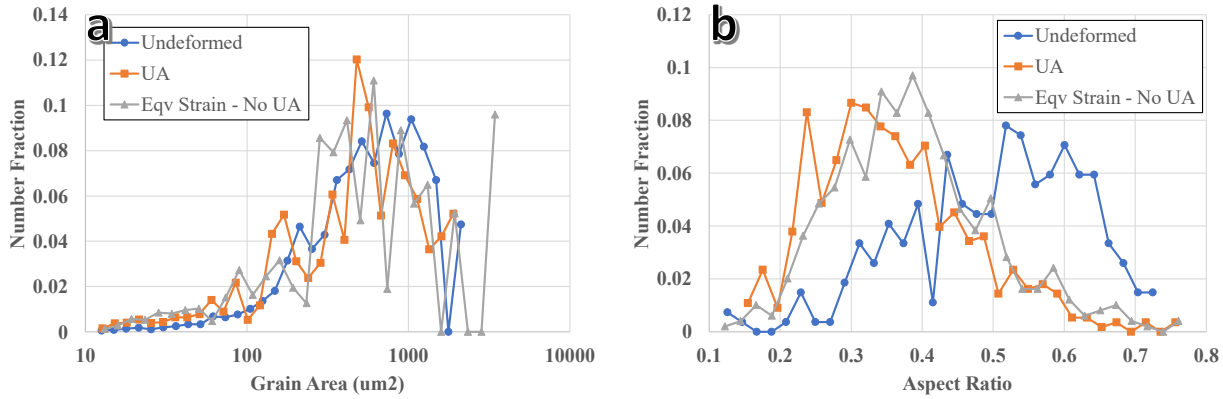

Figure 4-17 Microstructural properties for compression samples a) grain area and b) grain aspect ratio

Recent reports [34,40] cited an increase in the sub-grain size but based on the misorientation maps in **Figure 4-14**, the overall LAGB misorientation density increased for the UA sample, implying a smaller subgrain size. We can also inspect the grain size evolution as shown in **Figure 4-17a**. The grain size distribution is similar to the undeformed material, showing a skewed distribution to larger grain sizes between 500-700μm^2. The overall aspect ratios, **Figure 4-17b**, are similar in both UA and no-UA samples where the grains are flattened due to the compression. All in all, no observation of dynamic recrystallization was found, and the grain size and shape did not vary noticeably by adding UA.

The undeformed specimen pole figure, **Figure 4-18**, starts with a cube like texture $(001)[0\bar{1}0]$. The compressed UA and non-UA samples have a very similar texture evolution; neither resemble the strong fiber textures commonly observed in rolled sheet but a slight $(111)[1\bar{1}0]$ texture can be seen in the UA condition; this texture is common observed in tensile deformation of FCC specimens where the slip plane normal is orientated towards the macro deformation direction. Comparing the intensity between the three samples, the UA condition has the lowest texture intensity. The ODF representation of texture is also included in **Figure 4-19**and the common rolling texture in FCC materials is reference in **Figure 4-20.** Using Euler nomenclature $(\varphi_1, \phi, \varphi_2)$, the cubic texture intensity is observed at (45, 0, 45) with rotated cubic

textures at (0/90, 0, 45) in the starting AL 1100-O sheet material, **Figure 4-19a**. After UA compression, the cubic texture intensity has disappeared while the rotated cubic textures remain, **Figure 4-19b**. The greater intensities near (0, 60, 45) and (45, 60, 45) are indicative of slip plane rotation and a shear texture at (0, 60, 45). The conventionally compressed specimen does not share the similarities of the rotated cube texture nor the shear texture, **Figure 4-19c**. The data presented here coincides with the observations made in Chapter 3; the inclination of the textures at (0, 60, 45) and (0,0,45) should be studied further with larger data sizes. The potential for UA to promote shear texture can be quite beneficial for improving plastic strain ratios and deep drawing capabilities [87,88].

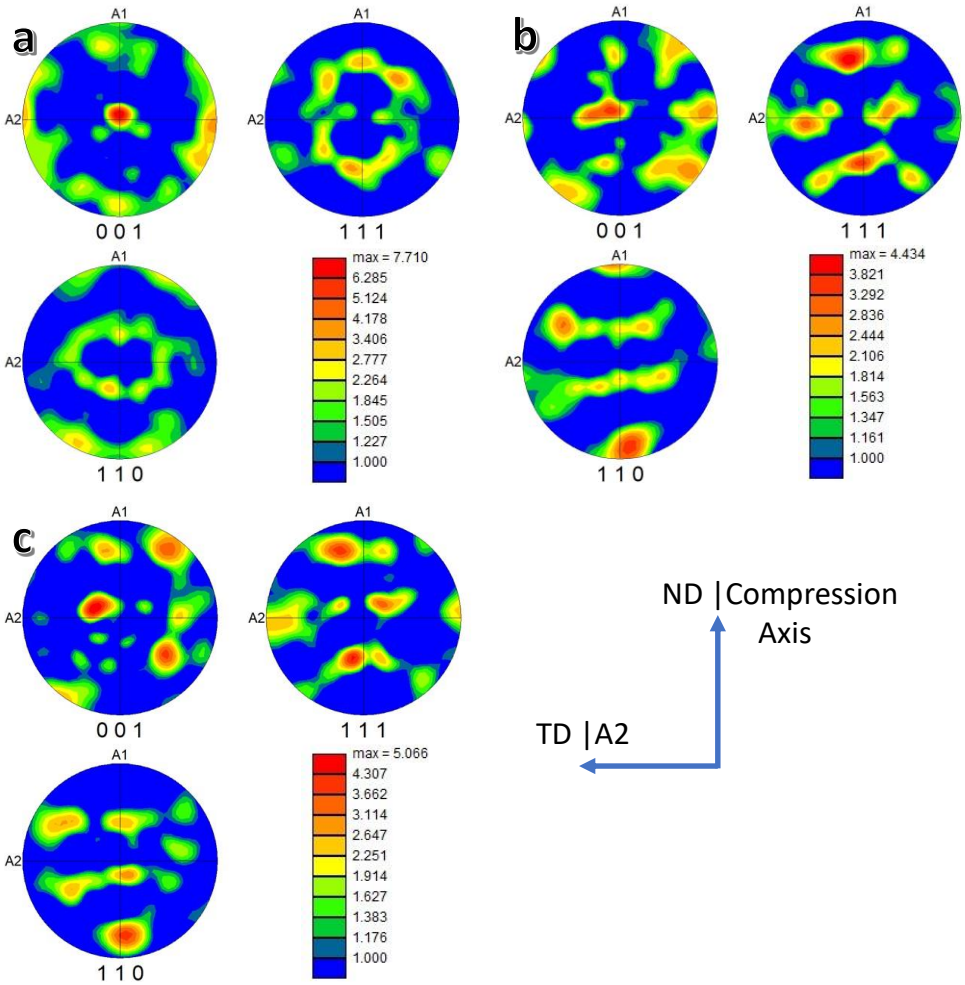

Figure 4-18 Pole figure textures of AL 1100-O in a) undeformed, b) UA sample, and c) conventional quasi-static load to the same equivalent strain

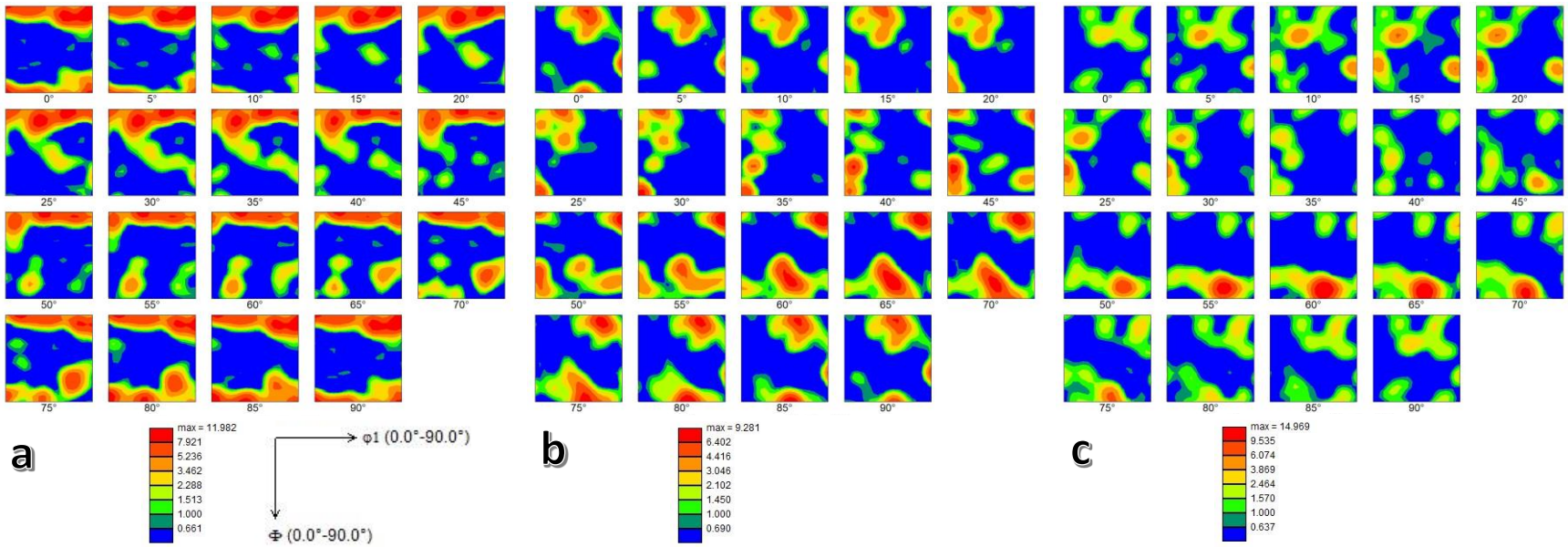

Figure 4-19 Orientation distribution function (ODF) representation of texture. a) undeformed Al 1100-O, b) UA compressed, c) equivalent strain no-UA compressed sample.

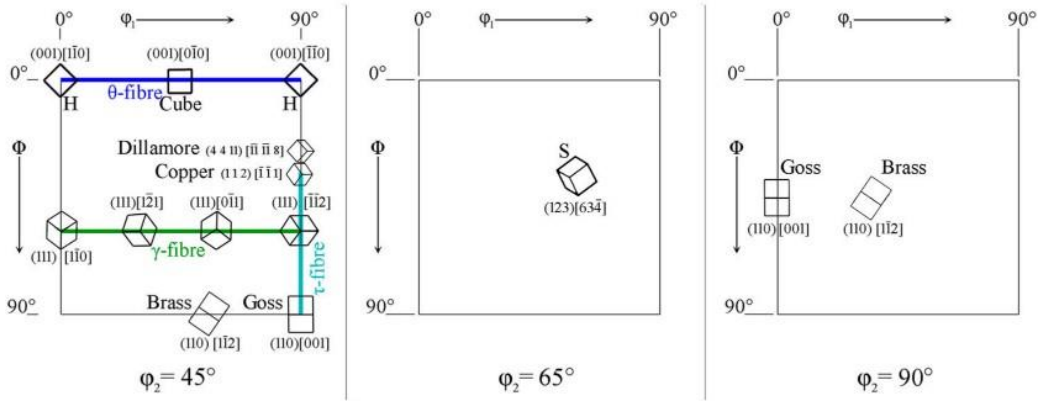

Figure 4-20 ODF reference of common rolling textures found in FCC metals

In summary, the higher fraction of low angle, $2° < \theta < 15°$, misorientations confirms the reports in literature. The KAM and GND maps indicate a greater presence of sub-grains in the microstructure. The texture plot shows a strong cube texture of the starting material and the support of ultrasonic softening to minimize the intensity after deformation. There are of course, limitations to this EBSD characterization. The dislocation density contribution comes from both statistically stored (SSDs) and geometrically necessary dislocations. Using the EBSD technique, only GNDs can be resolved as SSDs have a net zero burger vector over a given area. Electron channeling contrast imaging (ECCI) and transmission electron microscopy (TEM) are more suitable for SSDs analysis.

4.4 Summary and conclusions

In this chapter, we presented a series of ultrasonic assisted compression conditions that shed some light on discrepancies observed in literature. The studies from Zhou et al. [66] provide the initial hypothesis of volume dependent effects. The acoustic softening has a strong correlation to sample volume but using traditional acoustic energy terms failed to account for changes in sample dimensions. The amplitude strain parameter was proposed, and a linear correlation was observed across different sample dimension. The differences in softening for the AA2024-O and AA70705-O samples might be due to the precipitate density or the grain size [33] of the samples

since the sheet thickness differed by almost 2x. The softening response in UAC is much greater than UA-TPIF within the same amplitude window. Given the correlation of amplitude strain and state of strain to acoustic softening, we can hypothesize two potential reasons for difference in UA-TPIF response. First, the tool contact distributes the vibration displacement across the surface; therefore, an effect softening effect need to be considered. Seconds, the state of strain in UA-ISF can limit softening effect. Especially since the material can undergo varying degrees of cyclic strain and strain hardening. We seek to provide an equivalent experimental test case to verify the softening response is unique to the deformation mode and not kinematic artifacts of the ISF process in Chapter 5.

The material microstructure exhibited higher low angle misorientations like those reported in literature. The formation of low angle grain boundaries is a common method to reduce the overall internal defect density. Both KAM and GND maps are analysis methods that support this notion. The addition of UA helps to weaken the texture intensity; in these test samples, the starting material had the highest texture intensity.

CHAPTER 5
Ultrasonic Assisted Indentation and Empirical Analysis of Effective Softening

5.1 Introduction

Ultrasonic assisted compression and TPIF experiments displayed a significant difference in softening response. This muted translation from compression tests to manufacturing processes has been noted by Sedeghat et al. [72] through their simulation of press forming experiments conducted by Aziz and Lucas [75]. They introduced an effective coefficient and activation volume coefficient to calibrate the softening effect for their models. Although the method can lead to more accurate simulation results, the physical reasons are absent from this approach. In this chapter, ultrasonic assisted indentation (UAI) tests are performed on three aluminum grades: CP 1100-O, 2024-O, and 7075-O. The purpose of these indentation tests is to eliminate the tool lateral translation aspects of incremental forming, simplifying the stress state to study the effect of ultrasonic softening. The average softening from the three deformation processes was compared: compression >> indentation > ISF. A key distinction between these processes is the curvature of the rounded end tool; we hypothesize that the effective distribution of vibration around the tool is one key component to the muted effect. Therefore, an empirical model is used to calculate an effective softening value; the inputs to this empirical model were extracted from a FEA simulation of the indentation process.

5.2 Ultrasonic-assisted indentation (UAI)

5.2.1 Experimental methods

Three materials were selected for UAI testing: commercially pure aluminum (CP) 1100-O, AA2024-O, and AA7075-O. The CP aluminum was purchased from McMaster Carr while the two remaining alloys were supplied by the Boeing Company. Small coupons of 25.0mm x 25.0mm x 1.60mm dimensions were cut from 4’ wide sheet. Indentation tests were conducted in a Cincinnati HMC 400 EP CNC machine. The indenter tools used for these experiments are the same tools used in UA-ISF experiments from **Chapter 3** with a hemispherical end and diameters of 12.7mm and 8.00mm. The indenter was programmed to traveled at a constant speed to a depth of 0.40mm; the collective tool & machine compliance was measured to elastically deflect 0.1mm for every 1kN of load. Thus, the effective tool indentation depth is roughly ~0.15mm based on the maximum force observed in these experiments. A Kistler 9255A dynamometer measured the indenting force at a sample rate of 40Hz. Sheet coupons were lubricated using a moly disulfide grease (MoS_2) on both surfaces. The ultrasonic vibration was switch on after the indentation force reached 100-200N.

5.2.2 Results and discussion

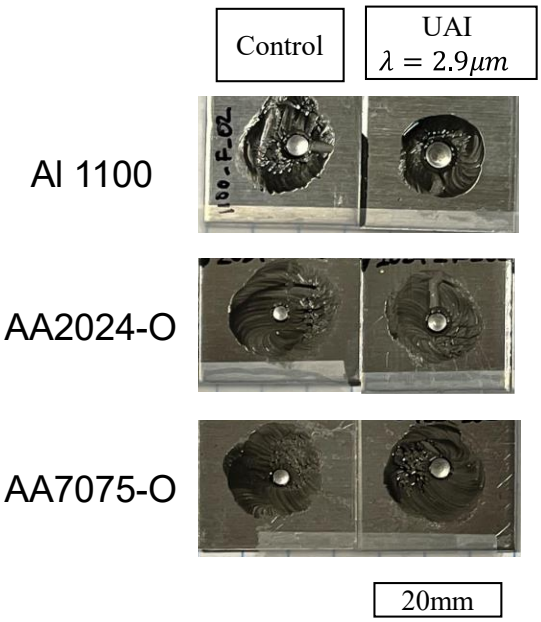

Figure 5-1 Indents of aluminum grades with and without ultrasonic assistance

Macro images of the control and UA indents are shown in **Figure 5-1**. The dark material on specimens is MoS_2 grease. The indent can be seen at the center of the grease area. Comparing the control samples to their respective ultrasonic assisted counterparts, adding the vibration creates a larger deformation zone. Taking the example of the AA2024-O specimen, optical images of these samples are shown in **Figure 5-2**. The diameter and depth increased by 21.2% and 31.0% respectively. Although difficult to see in the 2D image, the cross-sectional profiles, **Figure 5-3**, show a distinct pile-up mound at top edge of the deformation zone for the ultrasonic assisted case. The pile up has been heavily studied in the micro and nanoindentation community as the changes in contact area affects the calculations for elastic modulus and strength; the pile up has been empirically shown to correlate with low strain hardening materials, lower coefficient of friction, and a high young's modulus to yield strength ratio [89-91]. A modification in coefficient of friction and strain hardening is supported by the experimental work in **Chapters 3&4**. Although not investigated in detail in this thesis, a reduction in the tensile yield stress has been demonstrated by

our collaborators at The Ohio State University (Prof. Xun Liu and Dr. Jiarui Kang) and noted in literature [43,67].

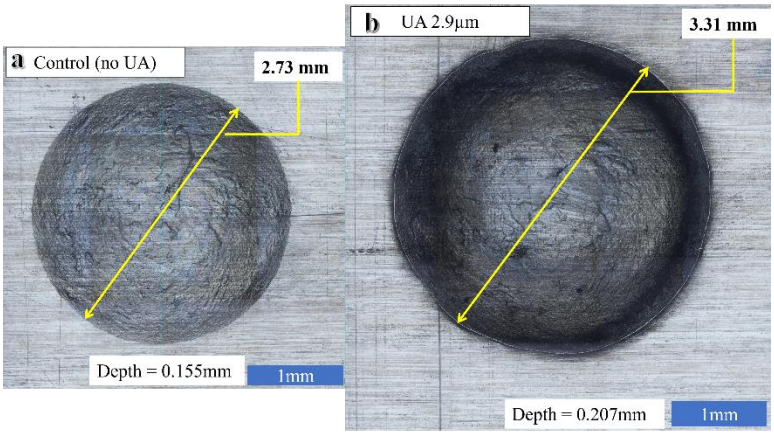

Figure 5-2 AA2024-O a) control indent and b) ultrasonic assisted indent. Pictures are scaled to allow for direction comparison.

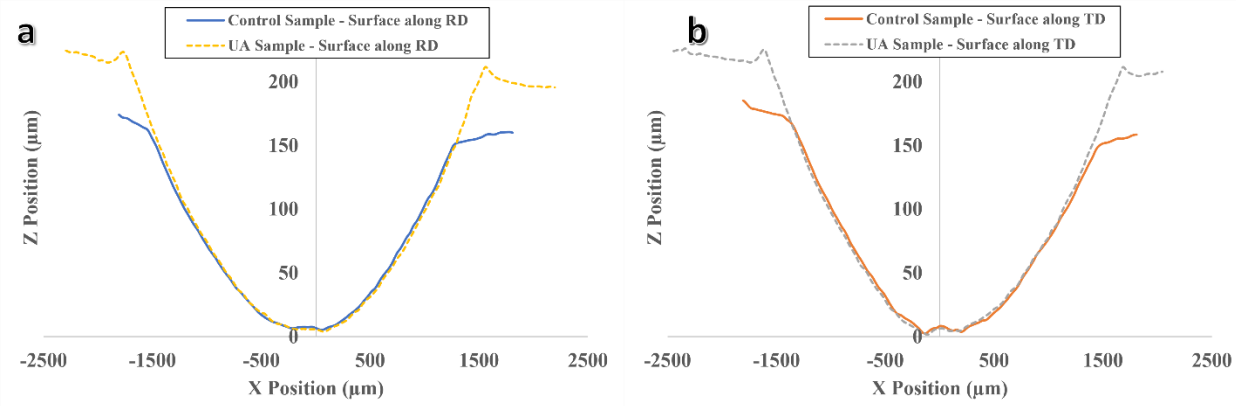

Figure 5-3 Cross sections of the indentation zone for AA2024-O control and ultrasonic assisted sample along a) RD and b) TD directions

The correspond forming force for each material is shown in **Figure 5-4**. The indentation force increases linearly with increasing indentation depth and this load trend is maintained when ultrasonic vibrations are incorporated. The ultrasonic softening is represented by a fraction of the UAI force divided by the force of the control sample. In all three cases, the ultrasonic softening effect diminishes with increasing depth of plunge; this coincides with the results of **Chapter 4** where the softening in compression samples decrease relative to the state of strain. A comparison

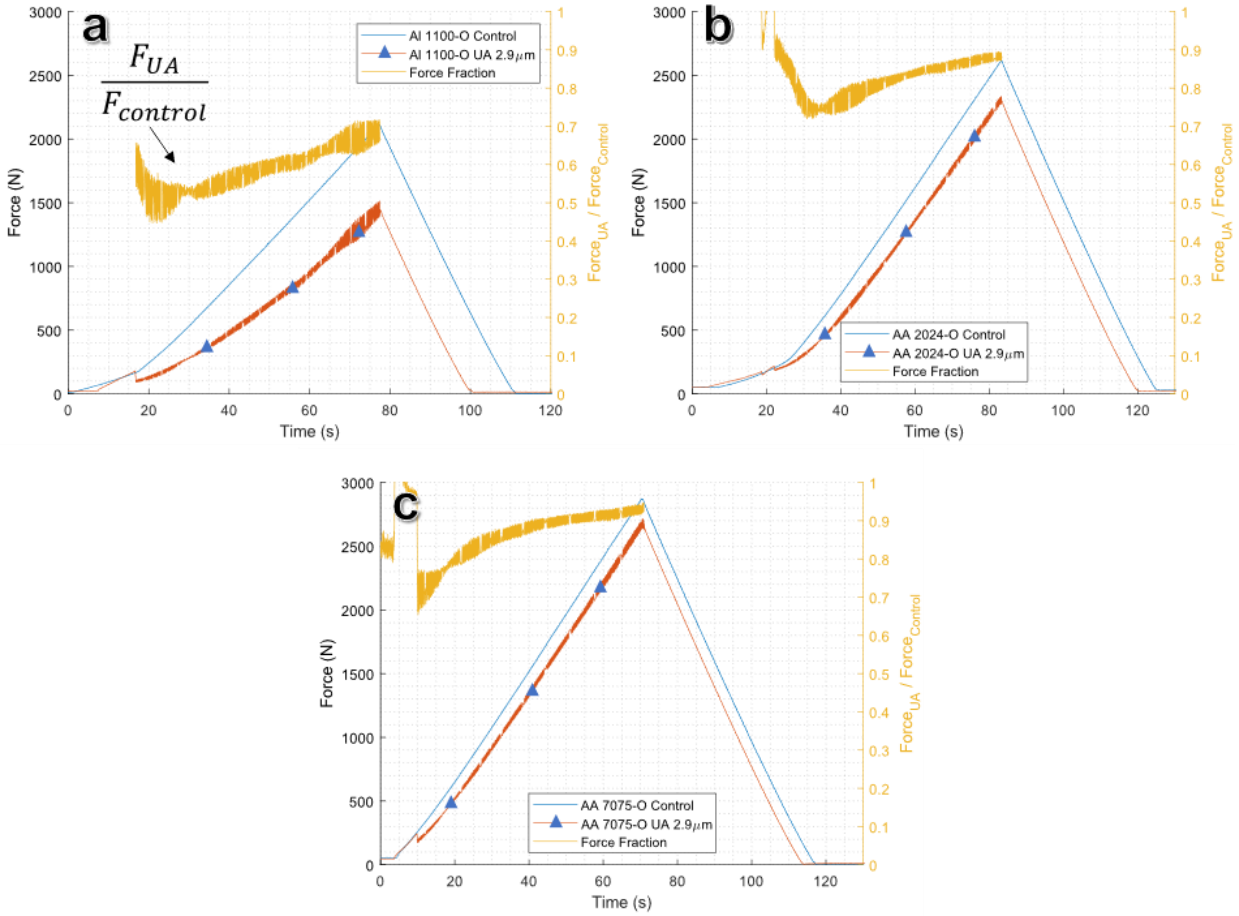

Figure 5-4 Indentation forces with and without ultrasonic assistance. a) Al 1100-O b) AA2024-O, and c) AA7075-O

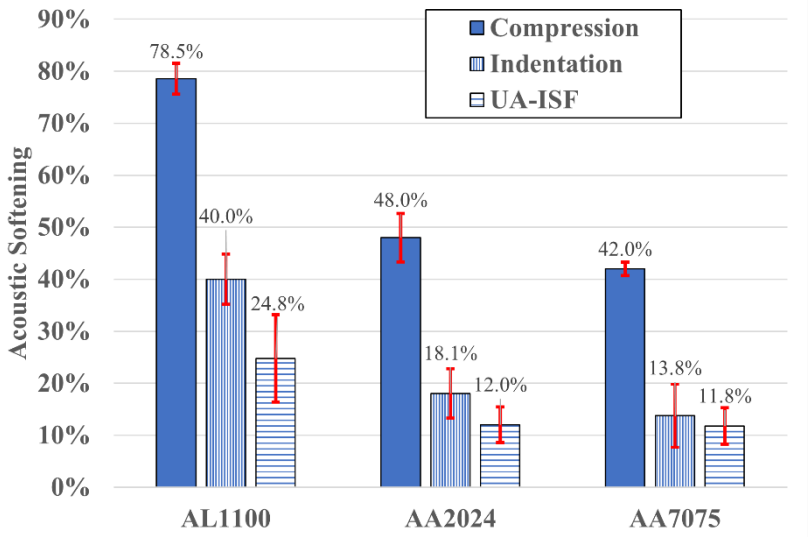

Figure 5-5 Comparison of the average ultrasonic softening across compression, indentation, and TPIF processes. Averages were taken from experiments with the same amplitude of 2.9-3.0μm.

between the three ultrasonic assisted deformation processes, UA-TPIF, UAC, and UAI, are averaged and shown in **Figure 5-5**. The average softening of UAI experiments is closely aligned with UA-TPIF results. As noted in **Chapter 3**, the 8.0mm tool surprisingly displayed a lower softening condition relative to the 12.7mm tool. To provide additional support to the finding, a AA2024-O coupon was indented with the 8.0mm tool and the softening response is compared to the 12.7mm tool in **Figure 5-6**. At 55s, the ultrasonic generator frequency stepped out of its operating range (20kHz ± 1kHz) and triggered a stop. However, the prior softening effect can still be compared and is shown to be less than 12.7mm tool diameter once again.

The mechanism of softening in UAI and UA-TPIF are shown to be closely correlated; therefore, UAI could provide a fast method for approximating the expected softening in incremental forming. Based on this analysis, there are two characteristics that may influence the softening behavior: 1) the displacement of the vibration amplitude is now a distributed due to the rounded contact interface and 2) the deformation modes in ISF and indentation are mixed conditions. Let's elaborate on the first idea. If the through thickness was discretized similar to a finite element mesh, each point through the thickness will radiate outward as the deformation

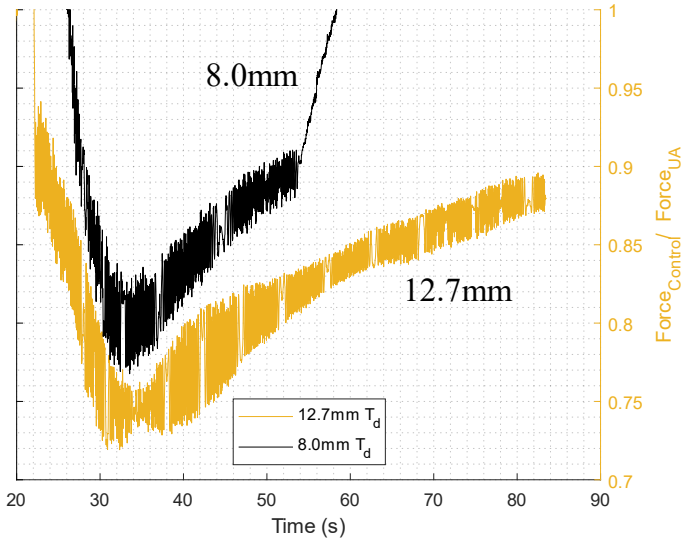

Figure 5-6 Softening fraction between 8.0mm and 12.7mm ultrasonic assisted indentation tests

progresses. In compression, the strain vector coincides with the axis of the vibration. The first hypothesis is to determine an effective amplitude strain distribution by considering only the displacement vectors parallel to the vibration axis. The second idea considers the change in deformation mode. Strain gradients coincide with bending and shearing type deformations which are heavily present in ISF. Similarly, shear strains are also present in indentation. The next section aims to incorporate a finite element method to test the first hypothesis of an effective amplitude strain. We first begin with an empirical equation for ultrasonic softening. Next, an indentation simulation is performed on AA2024-O; the tensile stress strain curve is used for the standard material model and an ultrasonic-assisted material model is presented based on the softening effect observed in **Chapter 4**. Finally, an effective softening scalar is calculated using this approach. Strain distribution micrographs are briefly discussed.

5.3 Ultrasonic softening function

The ultrasonic softening was experimentally observed to be a function of amplitude strain and the strain history based on **Figure 4-4**. The strains in this indentation simulation were found

to be quite small, $\varepsilon_{equivalent} < 0.2$, thus, the lower strain history data points, $\varepsilon = 0.10, 0.15, 0.20$, were taken from **Figure 4-4** and fitted to an empirical equation represented by:

$$\Delta\sigma = a\left[1 - \exp\left(-b * \left(\bar{\lambda}_{\varepsilon} \cdot 10E3\right)^{n_0}\right)\right] \tag{5-1}$$

and shown in **Figure 5-7**. Constants $a = 83.44$, $b = 0.6994$, and $n_0 = 0.90$.

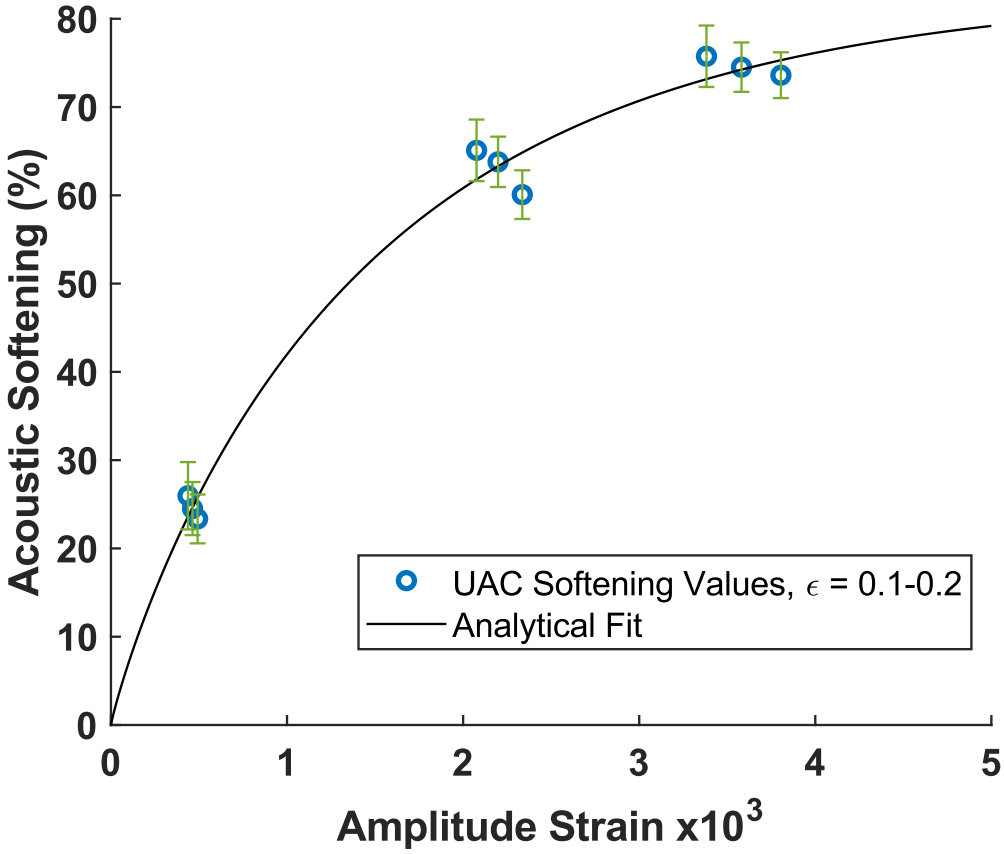

Figure 5-7 Ultrasonic softening function. Empirically fitted using amplitude strain results from Chap 4

5.4 Finite element simulation of an indention

5.4.1 Material model

Aluminum alloy 2024-O was chosen as the material for the indentation simulation. Tensile samples were machined using a water jet to ASTM-B557 standard [92]: 50mm gauge length,

12.7mm width, and rounded fillets of 12.7mm radius. An MTS 810 pulled the specimens at a rate of $0.02[s^{-1}]$. Given the potential anisotropic nature of rolled aluminum, the material model incorporates anisotropic coefficients based on the Hill's 1948 plasticity criteria [93]:

$$\sigma_{Hill} = \sqrt{F(\sigma_{22} - \sigma_{33})^2 + G(\sigma_{33} - \sigma_{11})^2 + H(\sigma_{11} - \sigma_{22})^2 + 2L\sigma_{23}^2 + 2M\sigma_{31}^2 + 2N\sigma_{12}^2} \qquad (5\text{-}2)$$

The parameters F, G, H, L, M, and N are constants obtained by tensile testing the sheet along 0°, 45°, and 90° relative to the rolling direction. Constitutive equations relate the Hill parameters to experimentally measured Lankford coefficients r_0, r_{45}, r_{90}, which represent the relative change of the in-plane strain to the through-thickness strain [94]. For this material, the Lankford coefficients were calculated to be $r_0 = 0.587, r_{45} = 0.739, r_{90} = 0.687$ based on the tensile stress-strain curves shown in **Figure 5-8**; the Hill'48 coefficients can be found in **Table 5-1**. A voce hardening law, $\sigma = k_0 = Q(1 - e^{-\beta\varepsilon})$, was used represent stress-strain curve of the 0° specimen. The mechanical properties and voce coefficients are listed in **Table 5-2**. For the UA material model, the UAC sample with an amplitude of $2.99\mu m$, **Figure 4-4**, was selected as a reference. The softening as a function of strain, $\Delta\sigma(\varepsilon)$, from **Figure 4-4b**, was used to modify the plastic curve; both material models are presented in **Figure 5-9**. The main reason for using the tensile curve as the control is because of the fidelity in measuring true stress-strain. This assumes the softening in compression and tension are equal.

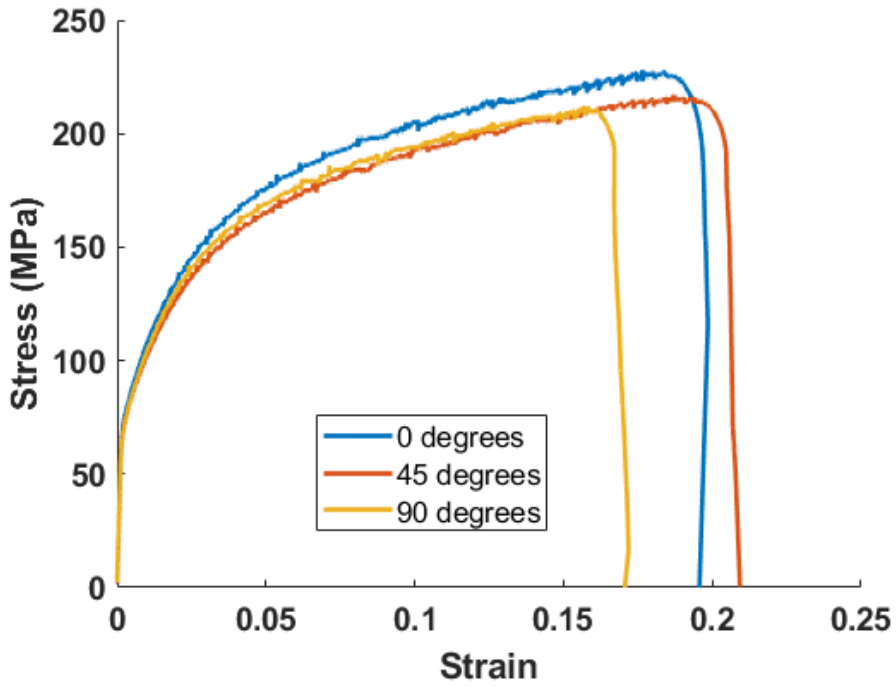

Figure 5-8 AA2024-O stress strain curve

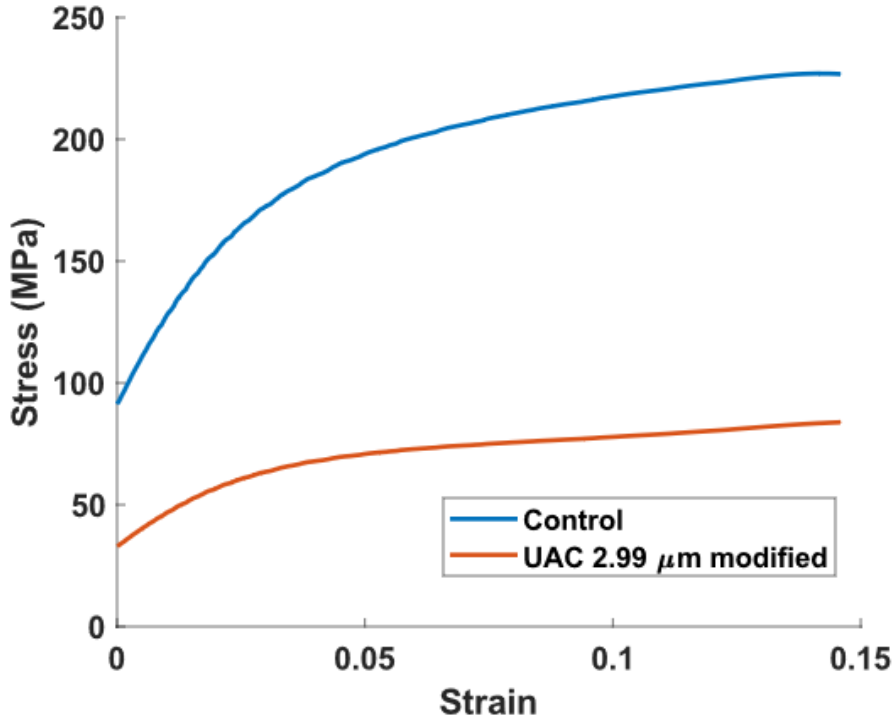

Figure 5-9 FEA material model: control and modified using ultrasonic softening response in UAC experiments

Table 5-1 Anisotropy coefficients for Hill 1948 model

F	G	H	L	M	N
0.538	0.630	0.370	-	-	1.448

Table 5-2 Mechanical properties and Voce hardening coefficients for AA2024-O

Modulus	Density	Poisson's Ratio	k_0	Q	β
69.74Gpa	2810 kg/m^3	0.33	97.52MPa	130.3MPa	-23.14

5.4.2 Finite element model

Mesh sensitivity analysis has been conducted by Dr.Shin [77] in the past on modeling of incremental sheet forming. Based on that work, 5 elements through-thickness was sufficient to resolve stress and strain gradients. In this model, 20 elements through the 1.6mm thickness was selected to increase the resolution of stress-strain gradients. The finer element size also reduces the likelihood of shear locking, an artificial defect in FE simulations known to increase the stiffness and thus overpredict forces. 8-node hexahedral linear solid element with reduced integration (C3D8R) was selected as the element type with hourglass control on default. A visual representation of the meshed aluminum coupon is shown in **Figure 5-10**. A larger meshing strategy was used outside of the 8.48mmm x 8.48mm zone to reduce the computation cost and time; the refined mesh area was sufficiently large to contain the plastic strain zone. A few parameters were adopted from the previous works of [24] and [77] which translate to this simulation: a coefficient of friction of 0.1, an analytical rigid tool with a tool diameter of 12.7mm, and a mass scaling factor of 10E7 to increase the speed of computation. A rigid surface was fixed behind the aluminum coupon instead of directly pinning the sheet itself.

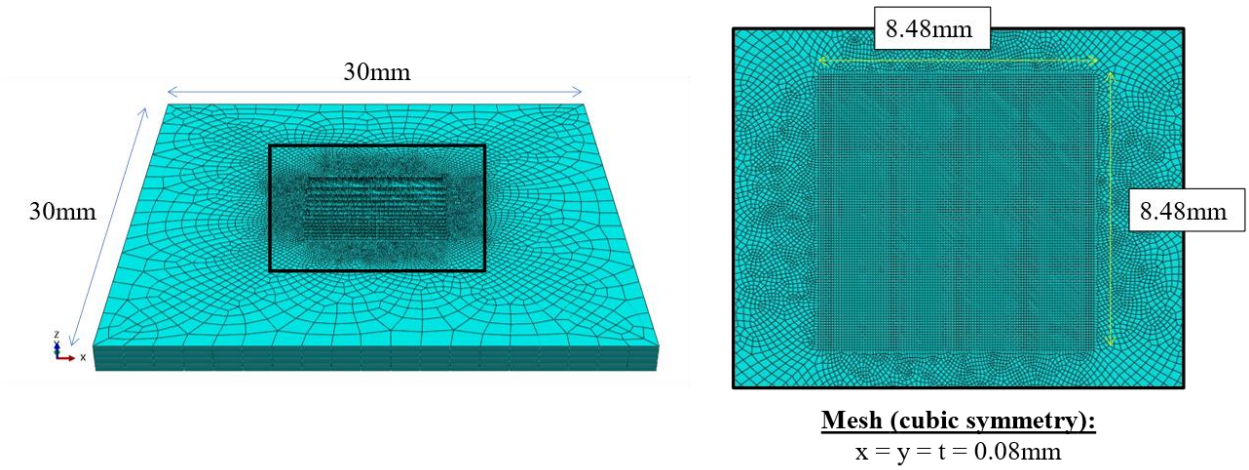

Figure 5-10 Aluminum 2024-O coupon meshed in Abaqus/Explicit

5.4.3 Effective softening

Experimental and simulated indentation forces are shown in **Figure 5-11**. The finite element model slightly over predicts the indentation force as the simulated depth, 0.150mm, is lower than what is experimentally observed, 0.155mm, **Figure 5-2**. Further indentation in the simulation would have push the indentation force higher. However, this model is sufficient for the purposes of this section

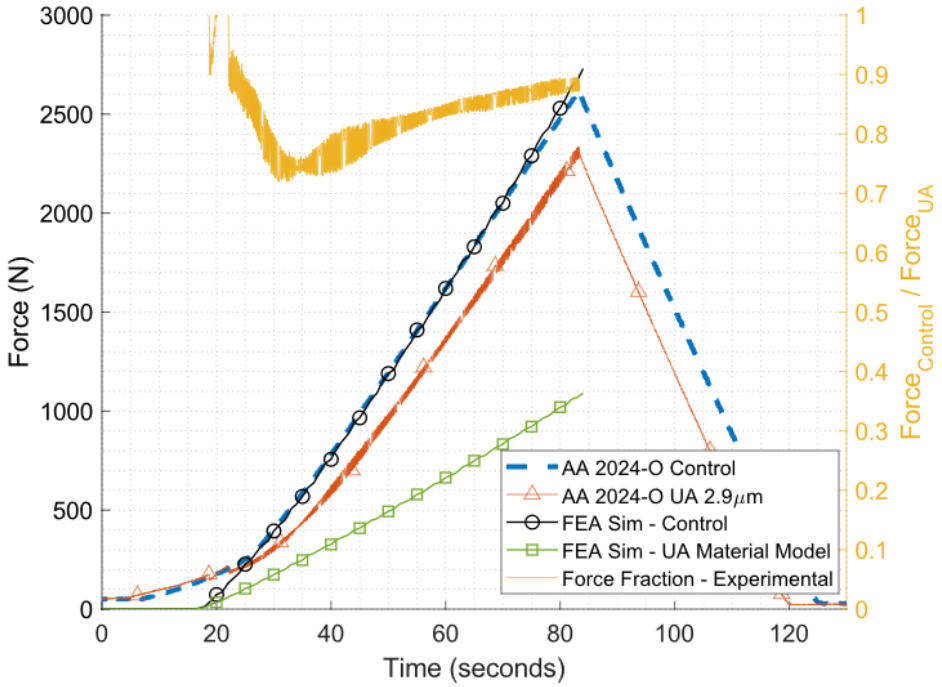

Figure 5-11 Experimental and FEA simulation forces for the indentation of AA2024-O coupon

as the differences in strain would be minor. The modified material model over predicts the softening effect with a 60.1% force reduction calculated at the peak force compared to experimental 18.1%. An equivalent strain cross-section, **Figure 5-12a**, was extracted from the control indent simulation**.** Most of the elemental strains are less than 13% which can partially explain the 60.1% softening as it is greatest at the lower strains. The minimum principle and PE23 strains, **Figure 5-12b&c**, account for the high localization in the PEEQ map. To test the distributed amplitude strain hypothesis, the displacement vectors were extracted at each nodal position near the deformation area as shown in **Figure 5-13a**. The displacement vectors are shown to radiate

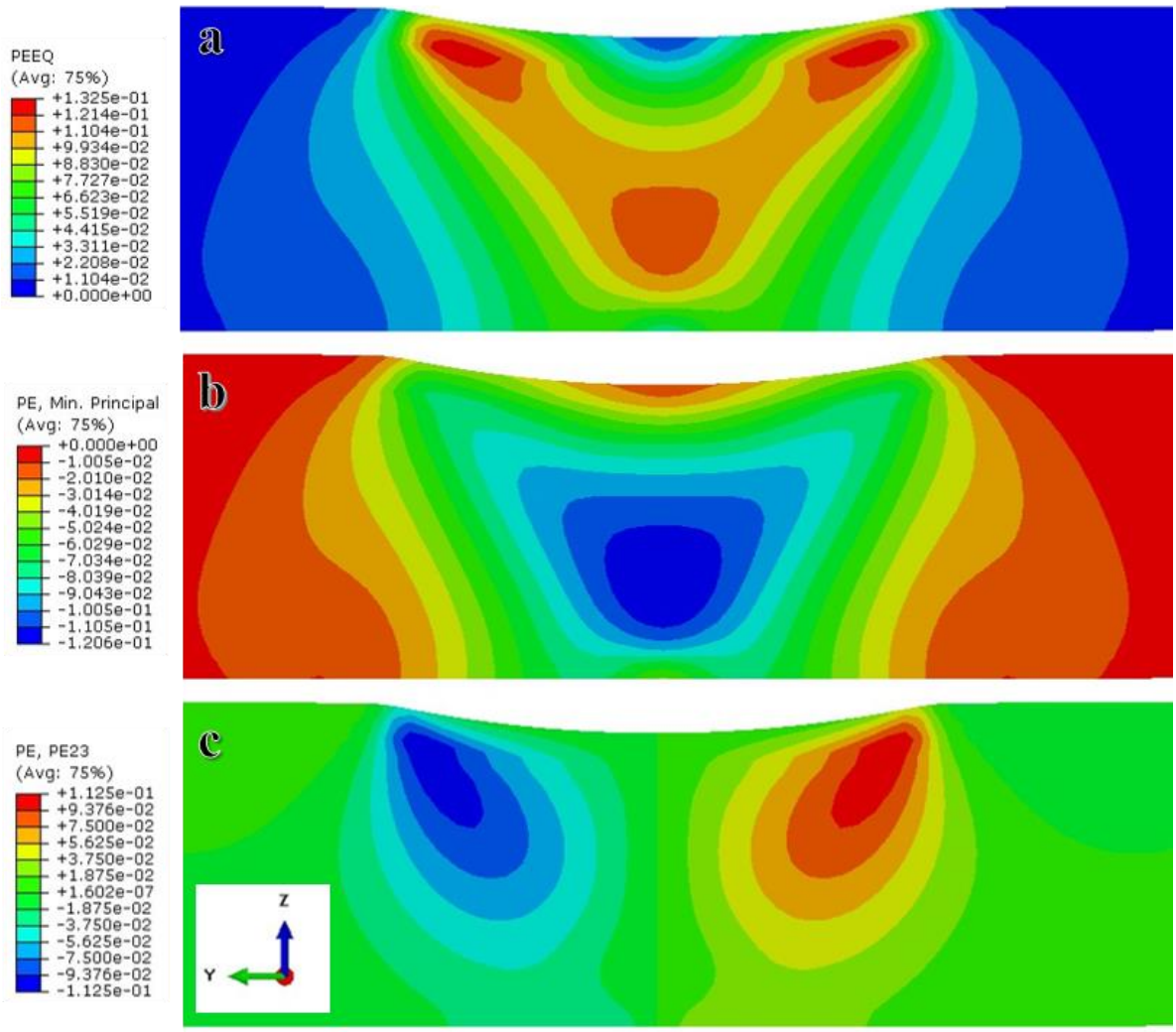

Figure 5-12 Cross section of simulated indentation with different strain components: a) plastic equivalent strain b) minimum principal strain and c) shear strain along the 23 direction (yz)

outwards, normal relative to the tool surface. **Figure 5-13**isolates vectors aligned with the vibration direction. This vector field is normalized to the vibration amplitude and the results were used as inputs into **Eq. (5-1)** as shown in **Figure 5-14.** A histogram of the assigned values is shown in **Figure 5-15** along with common statistical values listed in **Table 5-3**. This effective amplitude strain method corrects the over-approximation of softening from 60.1% to 31.5% and brings it closer to the experiment average of 18.1%. Based on **Figure 5-16**, the node with the largest effect is located right underneath the indenter tool. The points furthest from the contact interface experience the least vibration displacement and have low values of plastic strain. Although this method does not completely answer the question of why softening is muted in these experiments, it does provide some relevant insights.

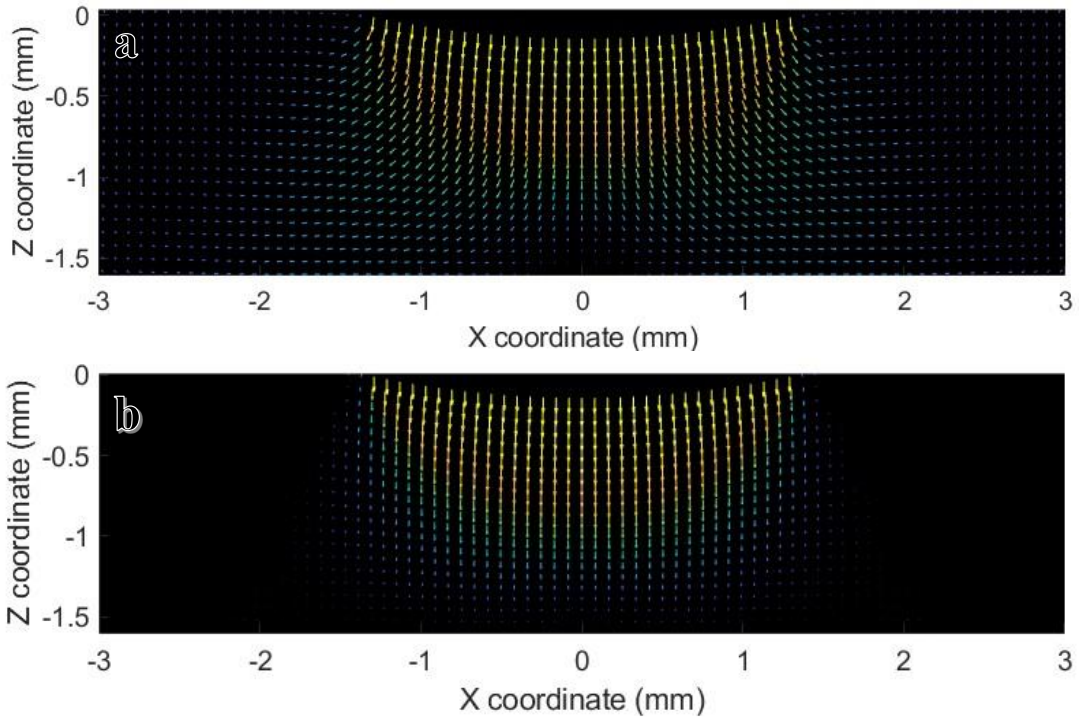

Figure 5-13 Displacement vector field of each node near the tool indentation area. a) net vector displacement and b) Z-vector only. The displacement scalar correlates to the size of the vector and color (small to large, blue to yellow)

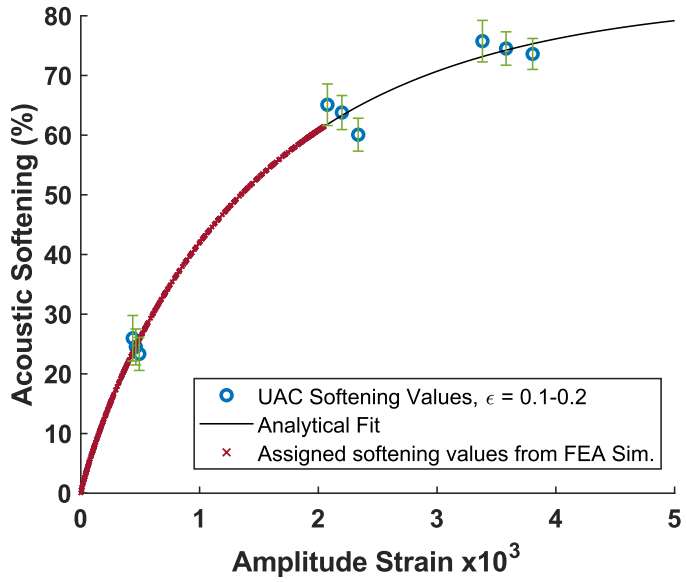

Figure 5-14 Assigned softening values based on nodal displacement vectors

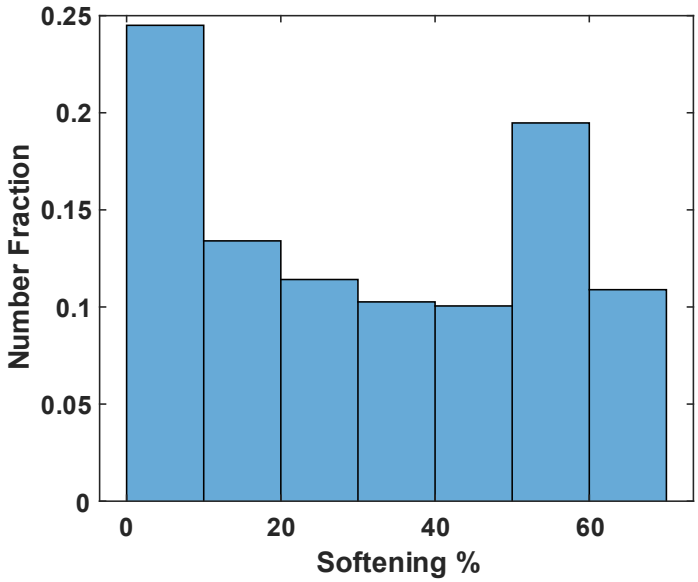

Figure 5-15 Distribution of assigned points using ultrasonic softening empirical function

Table 5-3 Common statistic representing the calculated effective softening in ultrasonic assisted indentation

Max	Min	Mean	Median	Standard Deviation
61.5%	0.07%	31.5%	30.5%	21.6%

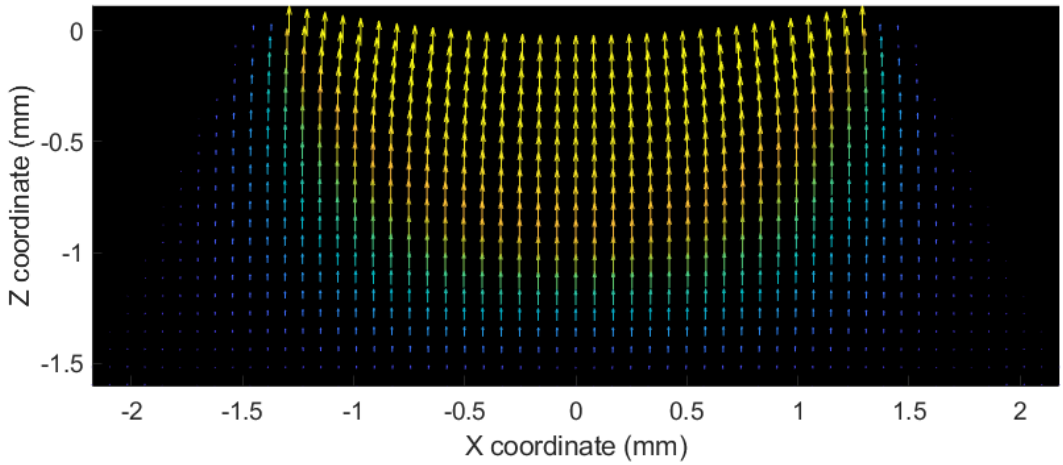

Figure 5-16 Softening value at each node around the indentation area. The softening magnitude correlates to the size of the vector and color (small to large, blue to yellow)

5.4.4 Discussion of assumptions and considerations

The method we used is simplistic for determining the effective softening and makes a few assumptions. First, this procedure assumed the tensile and compression response under ultrasonic assistance would be equivalent. Our collaborators from The Ohio State University (Prof. Xun Liu and Dr. Jiarui Kang) have conducted ultrasonic tensile tests on the same AA2024-O material and their experimental results show a lower softening within the same amplitude window. With that said, their samples were cut to 1-2mm in gauge length and 0.3mm in width so the differences could be attributed to the limit number of grains through thickness; grain size effects have been noted in literature [64,69].

Second, this method only accounts for contributions parallel to the vibration axis. The softening response may vary when the vibration is applied perpendicular to the tool motion. Experiments conducted by Dutta et al. [39] incorporated a transverse vibration in tensile tests, however, their emphasis was on microstructural analysis and further descriptions of flow properties were not discussed. The introduction of shear-based behavior under ultrasonic

assistance should be a key area for future work. A variety of shear-based specimens [96] have been designed to fit in tensile rigs and the results could contribute to a more complete description of ultrasonic softening.

5.5 Summary and conclusions

This chapter introduced a simplified indentation test coupled with ultrasonic vibrations. The purpose was to get closer to the deformation mode of incremental sheet forming and isolate the conditions which may be similar such as contact and deformation mode. In addition, an indentation process was simulated in Abaqus/Explicit and the strain distributions were used to calculate an effective softening percent. The major take aways from this chapter are as follows:

- The average softening results indicate the conditions in indentation are more in-line with incremental forming rather than compression. Ultrasonic assisted forces reduction is compression >> indentation > UA-TPIF.
- The commercially pure material consistently has higher softening effects relative to the precipitation hardenable alloys: 2024-O and 7075-O
- Incorporating the softening effect from a UAC test into the material model correlates directly to the indentation force
- UA compression data from Chapter 4 were used to create an empirical softening model. The assignment of softening values based on nodal displacement corrected the softening effect from 60.1% to 31.5%. Further research, defined in the discussion section, is required to improve and identify physical reasons for the muted effects in indentation and UA-TPIF.

CHAPTER 6
Summary and Future Work

6.1 Dissertation Summary

With the increasing demand for agile fabrication processes, incremental sheet forming (ISF) is a suitable solution to meet shorter turnaround times and low initial capital investments. However, the unique aspects of ISF also present unique challenges that need to be addressed before full adoption in industry. This dissertation identified major challenges collected from a literature survey as such: (a) inferior surface finish; (b) machine compliance; (c) stored residual stresses; and (d) assisted ISF processes to address low ductility material. The implementation of vibrations to ISF was highlighted as a potential method for addressing these challenges. Ultrasonic-assisted ISF (UA-ISF) of benchmark parts was investigated in detail and fundamental compression and indentation experiments were conducted to further explore the ultrasonic softening behavior of aluminum and its alloys. A summary of the conclusion in each chapter are listed below:

Chapter 3: An ultrasonic transducer was integrated into a CNC machine and UA-SPIF and UA-TPIF configuration were studied in detail. The part outcomes were characterized and the ultrasonic softening sensitivity to process parameters is identified. The results of this chapter are as follows:

- Adding vibration in the SPIF configuration shows minute changes in forming force and no additional improvement of formability for the AA7075-O material. It was proposed that part resonance led to ineffective used of acoustic energy into plastic deformation; large dips in forming forces during UA-SPIF support the idea of sheet resonance.

- Preliminary results in UA-TPIF showed force reductions between 11-18% which were further increased in the parametric study to a maximum of 27%. The added support die eliminated excessive elastic vibrations of the sheet.
- ISF process parameters, feed rate and programmed squeeze, had a minimal influence on the softening behavior, only varying 1-2%. The step-size and tool diameter have greater influence on the softening effect, demonstrating a 5-15% change in this work. The influence was initially hypothesized to be based on acoustic energy input, but experimental evidence supports the notion of highly localized deformation to be the key factor.
- The softening effect was also observed in the reduction of sheet thickness. With an applied amplitude of 3.3µm, the material was softening and further squeezed, reducing the thickness by an additional 150µm. At larger step sizes, the reduction in forming force may be recorded but changes in thickness are not implied; this is because the step size can limit the push of material.
- Surface roughness improvements were shown in UA-TPIF samples that did not exhibit material flow. Roughness parameters (mean, RMS, valley, peak, and peak-valley) showed improvement when added vibration. Changes in the kurtosis and skewness indicated a transition from a surface skewed towards pits to a more normalized texture. At high amplitudes, greater material flows along the surface; this worsens the surface roughness relative to a conventional part and leads to a bulge defect.
- Microstructural analysis of UA-TPIF of AL 1100-O, showed an increase subgrain formation, coinciding with reports in literature for AL. The initial cubic texture was still present in both conventional and UA-TPIF however, the UA texture intensity was broader and showed a minor rotation towards the shear texture: Bunge angle (0,60,45).

Chapter 4: Comparing the UA-TPIF softening behavior with UA compression/tension, two questions were raised: 1) why are there discrepancies in reported softening in literature and 2) why is softening in UA-TPIF distinctly lower compared to UAC softening? This chapter conducted a series of UAC experiments to gather an expect softening range for AA2024-O material and to explore the notion of sample volume dependence. The conclusion are as follows:

- Vibrations were applied to the compression of AA2024-O around a strain of 0.20 with increasingly higher vibration amplitudes. The correlation between softening and amplitude was found to be linear. The strain of the samples increased accordingly, suggesting minimal springback when vibrations are applied.
- Ultrasonic softening results indicate a much greater effect in compression than TPIF. At a vibration amplitude of 4μm, a 55% reduction is observed in UAC and only and 18% reduction in UA-TPIF.
- Full-UAC tests showed a change in softening and strain hardening behavior. The results would suggest the sample strain history can influence the degree of softening and the reverse statement can be made.
- The volume dependency experiment showed an inverse correlation to softening. Under changing sample dimensions, the acoustic parameters commonly used in literature to model ultrasonic softening were shown to be invariant; thus they are not presentative of the added work from ultrasonic vibrations
- An amplitude strain parameter was introduced and shown to correlate well with AA2024-O and AA7075-O softening responses across various dimension. This is logically valid as the work performed by the vibration should be proportional to the displacement and force.

- For the microstructural analysis, two samples were compressed to the same displacement and one of them received ultrasonic excitation at this hold position. The microstructure again validates the results shown in Chapter 3.

Chapter 5: Noting the significant difference in ultrasonic response between compression and TPIF, ultrasonic indentation test were performed to remove the kinematic aspects in TPIF. The conclusion of this chapter are as follows:

- UAI tests correspond well with UA-TPIF results suggesting the contact mechanics and deformation behavior are likely the cause for muted softening. The lower softening effect is also observed in UAI when changing the tool form 12.7mm to 8.0mm.
- Modifying the material model using the softening response in UAC showed a direct correlation to the change in reaction force of the FE model. A distributed amplitude strain method was proposed which shifted the 60.1% force reduction from the UAC modified FE simulation to 31.5%.
- The proposed method did not fully account for the lower softening behavior in UAI tests but is likely one contributing factor. The strain maps extracted from the FE simulation show a heavy dependence on shear strain which has not been investigated in literature.

6.2 Proposed future work

Chapter 3*:* the experimental investigation in Chapter 3 provides a good basis for expected outcome in UA-TPIF. The change in tool diameters can be further explored to identify the trend in softening and changes in surface finish. The use of large tool diameters has been reported in literature to smoothen wavey scallop features and achieve automotive grade surfaces when a small step size is used. Increasing the tool diameter changes the deformation mechanics towards a stretching type deformation; this possibly shift the expect softening range closer toward UAC and UAT responses.

The application of UA in this chapter was strictly focused on assisted the deformation during forming. However, ultrasonic vibrations could also be used as a last pass method to capture the benefits improving the surface finish and reduce the stored residual stress in the formed geometry. ***Chapter 4****:* the work in this chapter confirmed the ultrasonic softening phenomenon based on changes in material strain, springback, and microstructure. These are of course macro-observations, but he proposed theory for ultrasonic softening revolve around dislocation annihilation and the reduction of stored strain energy through subgrain formation. The microstructural investigation using EBSD can only resolve contributions toward geometrically necessary dislocations (GNDs) coalescing into subgrains and lack information on changes in the statistically stored dislocation (SSDs) density. Characterization of dislocation density are typically imaged using transmission electron microscopy, however, the addition of a vibration grip or indenter, at ultrasonic frequencies, does not exist to the best of my knowledge. A method that can potentially capture changes in SSDs is electron channeling contrast imaging (ECCI); combining this technique with an in-situ UA tensile experiment, the evolution of both SSDs and GNDs can be determined. Using just EBSD characterization, an area of future work is characterizing the texture evolution at various points along a UAC test.

Residual hardening and softening has also been observed in literature but no physical aspects have been confirmed through experiments; most justifications are based on empirical modeling. Microstructural characterization at three specific points in a UAC are of interest: 1) after vibrations have been switch off, 2) loading period of the specimen after UA (high strain hardening), and 3) after the material strain hardening has stabilized and shows a residual hardening or softening effect.

Chapter 5: the amplitude strain distribution is likely one factor influencing the muted softening effect. The assumptions presented in Chapter 4 guides the future work towards UA tensile testing. UAT provides the relationship between sample texture and yielding; the collected information can be incorporated into known plasticity models and used in simulations. In addition, characterizing the shearing behavior with UA would be insightful as the shear strain contribution was significant in the FE modeling of indentation test.

References

1. Silva, M. B., Bay, N. & Martins, P. A. F. in Sustainable Manufacturing (ed. Davim, J. P.) (2010).
2. J. Cao, Y. Huang, N. Reddy, R. Malhotra, and Y. Wang, "Incremental sheet metal forming: advances and challenges," *Int. Conf.* vol. 3, no. c, pp. 1–16, (2008).
3. N. V. Reddy, R. Lingam, and J. Cao, "Incremental Metal Forming Process in Manufacturing," pp. 411–449, (2015).
4. Nimbalkar, D. H. & Nandedkar, V. M. Review of Incremental Forming of Sheet Metal Components. Int. J. Eng. Res. Appl. 3, 39–51 (2013).
5. Scheffler, S. et al. Incremental sheet metal forming on the example of car exterior skin parts. Procedia Manuf. 29, 105–111 (2019).
6. Echrif, Salah B.M. and Meftah Hrairi. Significant Parameters for the Surface Roughness in Incremental Forming Process. Materials and Manufacturing Process, 29:697-703 (2014).
7. Azevedo NG, Farias JS, Bastos RP, Teixeira P, Davim JP, Alves de Sousa RJ. Lubrication aspects during Single Point Incremental Forming for steel and aluminum materials. Int. J. Precis. Eng. Manuf. 16(3):589-595 (2015).
8. Benmessaod, R., et al. Tool, lubricant and process parameters investigation to for an AA 3003-H12 sheet by single point incremental forming process. Int. J. Sci. Eng. Res., 7(11), 950-960 (2016).
9. Hagan, E. and J. Jeswiet. Analysis of surface roughness for parts formed by computer numerical controlled incremental forming. Proc. Instn. Mech. Engrs. Vol 218, Part B: J . Engineering Manufacture (2004)
10. Dakhli, M. et al. Optimization of processing parameters and surface roughness of metallic sheets plastically deformed by incremental forming process. Int. J. Adv. Manuf. Technol. 102:977-990 (2019).
11. Wei, Hongyu. et al. Surface roughness as a function of friction indicator and an important parameters-combination having controlling influence on the roughness: recent results in incremental forming. Int. J. Adv. Manuf. Technol. 101:2533-2545 (2019).
12. Kumar, Ajay et al. Effects of Process Parameters on Surface Roughness in Incremental Sheet Forming. Materials Today: Proceedings 5, 28026-28032 (2018).
13. Kumar, Ajay and Vishal Gulati. Experimental investigation and optimization of surface roughness in negative incremental forming. Measurement, 131:419-430 (2019).
14. Jawale, Kishore et al. Lubrication study for Single Point Incremental Forming of Copper. J. Phys. Conf. Ser. 734 (2016).

15. Jawale, Kishore et al. Microstructural investigation and lubrication study for single point incremental forming of copper. Int. J. Solids. Struct. 151: 145-151 (2018)

16. Eyckens, P. et al. Strain evolution in the single point incremental forming process: Digital image correlation measurement and finite element prediction. International Journal of Material Forming, 4, 1, 55-71 (2010). 74 [27]

17. Jackson, K. & Allwood, J. The mechanics of incremental sheet forming. J. Mater. Process. Technol. 209, 1158–1174 (2009). [28]

18. Malhotra, R., Xue, L., Belytschko, T. & Cao, J. Mechanics of fracture in single point incremental forming. J. Mater. Process. Technol. 212, 1573–1590 (2012). [29]

19. Smith, J., Malhotra, R., Liu, W. K. & Cao, J. Deformation mechanics in single-point and accumulative double-sided incremental forming. Int. J. Adv. Manuf. Technol. 69, 1185– 1201 (2013). [30]

20. Seong, D. Y., Haque, M. Z., Kim, J. B., Stoughton, T. B. & Yoon, J. W. Suppression of necking in incremental sheet forming. Int. J. Solids Struct. 51, 2840–2849 (2014).

21. Emmens, W. C., & van den Boogaard, A. H. (2009). An overview of stabilizing deformation mechanisms in incremental sheet forming. Journal of Materials Processing Technology, 209(8), 3688–3695.

22. Tanaka, S., Nakamura, T., Hayakawa, K., Nakamura, H., & Motomura, K. (2007). Residual stress in sheet metal parts made by incremental forming process. AIP Conference Proceedings, 908(May 2007), 775–780.

23. Maaß, F., Gies, S., Dobecki, M., Brömmelhoff, K., Tekkaya, A. E., & Reimers, W. Analysis of residual stress state in sheet metal parts processed by single point incremental forming. AIP Conference Proceedings. (2018).

24. Bansal, A. Experimental and Numerical Investigation of Part Fabrication by Incremental Sheet Forming. Ph.D. dissertation. Dept. Mech. Eng. University of Michigan. Ann Arbor, MI. (2021)

25. Allwood, J. M., Music, O., Raithathna, A., & Duncan, S. R. Closed-loop feedback control of product properties in flexible metal forming processes with mobile tools. CIRP Annals - Manufacturing Technology, 58(1), 287–290. (2009).

26. Duflou, J. R., Callebaut, B., Verbert, J., & De Baerdemaeker, H. Laser Assisted Incremental Forming: Formability and Accuracy Improvement. CIRP Annals, 56(1), 273–276. (2007).

27. Xu, D. *et al.* A Comparative Study on Process Potentials for Frictional Stir- and Electric Hot-assisted Incremental Sheet Forming. *Procedia Eng.* **81**, 2324–2329 (2014).

28. Vahdati, M., Mahdavinejad, R., & Amini, S. Investigation of the ultrasonic vibration effect in incremental sheet metal forming process. Proceedings of the Institution of Mechanical Engineers, Part B: Journal of Engineering Manufacture. (2017).

29. Amini, S., Hosseinpour Gollo, A. & Paktinat, H. An investigation of conventional and ultrasonic-assisted incremental forming of annealed AA1050 sheet. *Int. J. Adv. Manuf. Technol.* (2017)

30. Li, Y., Chen, X., Sun, J., Li, J. & Zhao, G. Effects of ultrasonic vibration on deformation mechanism of incremental point-forming process. *Procedia Eng.* **207**, 777–782 (2017).

31. Langenecker, B. Work-softening of metal crystals by alternating the rate of glide strain. *Acta Metall.* **9**, 937–940 (1961).

32. Amini, S., Hosseinpour Gollo, A. & Paktinat, H. An investigation of conventional and ultrasonic-assisted incremental forming of annealed AA1050 sheet. *Int. J. Adv. Manuf. Technol.* (2017) doi:10.1007/s00170-016-9458-7.

33. Aziz, A. (2012). Characterizing the effective material softening in ultrasonic forming of metals. Ph.D. dissertation. College of Eng. University of Glasgow. Scotland, UK. (2012)

34. Cheng, B., Leung, H. S. & Ngan, A. H. W. Strength of metals under vibrations - Dislocation-density-function dynamics simulations. *Philos. Mag.* **95**, (2015).

35. Cheng, Z., Li, Y., Li, J., Li, F. & Meehan, P. A. Ultrasonic assisted incremental sheet forming: Constitutive modeling and deformation analysis. *J. Mater. Process. Technol.* **299**, (2022).

36. Daud, Y., Lucas, M. & Huang, Z. Y. Ultrasonic Compression Tests on Aluminium. *Appl. Mech. Mater.* **3**–**4**, 99–104 (2005).

37. Daud, Y., Lucas, M. & Huang, Z. Superimposed ultrasonic oscillations in compression tests of aluminium. *Ultrasonics* **44**, e511–e515 (2006).

38. Daud, Y., Lucas, M. & Huang, Z. Modelling the effects of superimposed ultrasonic vibrations on tension and compression tests of aluminium. *J. Mater. Process. Technol.* **186**, 179–190 (2007).

39. Deshpande, A. & Hsu, K. Acoustic energy enabled dynamic recovery in aluminium and its effects on stress evolution and post-deformation microstructure. *Mater. Sci. Eng. A* **711**, 62–68 (2018).

40. Deshpande, A., Tofangchi, A. & Hsu, K. Microstructure evolution of Al6061 and copper during ultrasonic energy assisted compression. *Mater. Charact.* **153**, 240–250 (2019).

41. Dutta, R. K. *et al.* The effect of tensile deformation by in situ ultrasonic treatment on the microstructure of low-carbon steel. *Acta Mater.* **61**, 1592–1602 (2013).

42. Dutta, R. K., Petrov, R. H., Hermans, M. J. M. & Richardson, I. M. Accommodation of Plastic Deformation by Ultrasound-Induced Grain Rotation. *Metall. Mater. Trans. A Phys. Metall. Mater. Sci.* **46**, 3414–3422 (2015).

43. Fartashvand, V., Abdullah, A. & Sadough Vanini, S. A. Investigation of Ti-6Al-4V alloy acoustic softening. *Ultrason. Sonochem.* **38**, 744–749 (2017).

44. Hu, J., Shimizu, T., Yoshino, T., Shiratori, T. & Yang, M. Ultrasonic dynamic impact effect on deformation of aluminum during micro-compression tests. *J. Mater. Process. Technol.* **258**, 144–154 (2018).

45. R. Pohlman, E. Influence of ultrasonic vibration on metallic friction. Ultrasonics, 4 (1966), pp. 176-185

46. Sasome, D., Ibrahim, I. An experimental study of the mechanics of ultrasonic tube-bending (Vol. 39, Issue 1). Ultrasonics International 83: Halifax, Canada. (1977)

47. Dong, S. Friction and Wear Reduction via Ultrasonic Lubrication. PhD Dissertation. Dept. of Mech. Eng. The Ohio State University. Columbus, OH (2015).

48. Littmann, W., Storck, H., and Wallaschek, J., "Sliding friction in the presence of ultrasonic oscillations: superposition of longitudinal oscillations," Archive of Applied Mechanics, 71, 549–554, 2001.

49. Kumar, V. and Hutchings, I. "Reduction of the sliding friction of metals by the application of longitudinal or transverse ultrasonic vibration," Tribology International, 37, 833–840, 2004.

50. Teidelt, E., Starcevic, J, and Popov, V., "Influence of ultrasonic oscillation on static and sliding friction," Tribology Letters, 1, 51–62, 2012.

51. Dong, S., Dapino, M. Experiments on Ultrasonic Lubrication Using a Piezoelectrically-assisted Tribometer and Optical Profilometer. Journal of Visualized Experiments, 103. (2015)

52. Rozner, A. G. Effect of Ultrasonic Vibration on Coefficient of Friction during Strip Drawing. The Journal of the Acoustical Society of America, 49(5A), 1368–1371. (1971)

53. Winsper, C. E., Sansome, D. H. A Review of the Application of Oscillatory Energy To Metals Deforming Plastically. In Advances in Machine Tool Design and Research 1967. Pergamon Press Ltd. (1968)

54. Siegert, K. & Ulmer, J. Influencing the friction in metal forming processes by superimposing ultrasonic waves. *CIRP Ann. - Manuf. Technol.* **50**, 195–200 (2001).

55. Silva, M. B., & Martins, P. A. F. (2013). Two-point incremental forming with partial die: Theory and experimentation. JMEPEG 22:1018–1027 (2013).

56. Skjoedt, M., Bay, N., Endelt, B., & Ingarao, G. Multi stage strategies for single point incremental forming of a cup. International Journal of Material Forming, 1(SUPPL. 1), 1199–1202. (2008).

57. Bambach, M. A geometrical model of the kinematics of incremental sheet forming for

the prediction of membrane strains and sheet thickness. J. Mater. Process. Technol. 210, 1562–1573 (2010).

58. Nath, M. Microstructure and Surface Characterization of Incrementally Formed AA 7075. Ph.D. dissertation. Dept. Material Science & Eng. University of Michigan. Ann Arbor, MI. (2019)

59. Bansal, A., Cheng, R., Banu, M., Taub, A., & Ni, J. Experimental Analysis of Material Squeeze Factor in Two-Point Incremental Forming of AL 7075-O. Proceedings of the ASME 2020 15th International Manufacturing Science and Engineering Conference. Volume 2. September 3, 2020. (2020)

60. Filice, L., Fratini, L., & Micari, F. Analysis of material formability in incremental forming. CIRP Annals - Manufacturing Technology, 51(1), 199–202. (2002).

61. Salem, E., Shin, J., Nath, M., Banu, M., & Taub, A. I. (2016). Investigation of Thickness Variation in Single Point Incremental Forming. Procedia Manufacturing, 5, 828–837.

62. Radu, C., et al. Anaylsis of the Surface Quality of Parts Processed by Single Point Incremental Forming. J. Eng. Stds. Res. 19 (2013)

63. Maaß, F., Gies, S., Dobecki, M., Brömmelhoff, K., Tekkaya, A. E., & Reimers, W. Analysis of residual stress state in sheet metal parts processed by single point incremental forming. AIP Conference Proceedings. (2018).

64. Ahmadi, F., Farzin, M., & Mandegari, M. Effect of grain size on ultrasonic softening of pure aluminum. Ultrasonics, 63, 111–117. (2015).

65. Blaha F., Langenecker B., Tensile deformation of zinc crystal under ultrasonic vibration, Naturwissenschaften 42 (1955) 1-10.

66. Zhou, H., Cui, H., & Qin, Q. H. (2018). Influence of ultrasonic vibration on the plasticity of metals during compression process. Journal of Materials Processing Technology, 251(November 2016), 146–159.

67. Lin, J., Li, J., Liu, T., Xie, Z., Zhu, L., Wang, Y., & Guan, Y. (2020). Investigation on ultrasonic vibration effects on plastic flow behavior of pure titanium: Constitutive modeling. Journal of Materials Research and Technology.

68. Kang, J., Liu, X., & Xu, M. (2020). Plastic deformation of pure copper in ultrasonic assisted micro-tensile test. Materials Science and Engineering A, 785(April), 139364.

69. Wang, C. J., Liu, Y., Guo, B., Shan, D. B. & Zhang, B. Acoustic softening and stress superposition in ultrasonic vibration assisted uniaxial tension of copper foil: Experiments and modeling. Mater. Des. 112, 246–253 (2016).

70. Yao, Z. et al. Acoustic softening and residual hardening in aluminum: Modeling and experiments. Int. J. Plast. 39, 75–87 (2012).

71. Kang, J., Liu, X. & Niezgoda, S. R. Crystal plasticity modeling of ultrasonic softening effect considering anisotropy in the softening of slip systems. Int. J. Plast. 156, 103343 (2022).

72. Sedaghat, H., Xu, W. & Zhang, L. Ultrasonic vibration-assisted metal forming: Constitutive modelling of acoustoplasticity and applications. J. Mater. Process. Technol. 265, 122–129 (2019).

73. Siddiq, A. & Sayed, T. El. A thermomechanical crystal plasticity constitutive model for ultrasonic consolidation. Comput. Mater. Sci. 51, 241–251 (2012).

74. Lin, J. et al. Investigation on ultrasonic vibration effects on plastic flow behavior of pure titanium: Constitutive modeling. J. Mater. Res. Technol. (2020)

75. Abdul Aziz, S. & Lucas, M. The effect of ultrasonic excitation in metal forming tests. Appl. Mech. Mater. 24–25, 311–316 (2010).

76. Meng, B., Cao, B. N., Wan, M., Wang, C. J. & Shan, D. B. Constitutive behavior and microstructural evolution in ultrasonic vibration assisted deformation of ultrathin superalloy sheet. Int. J. Mech. Sci. 157–158, 609–618 (2019).

77. Shin, J. Investigation of Incremental Sheet Forming (ISF) using Advanced Numerical and Analytical Approaches. Ph.D. dissertation. Dept. Mech. Eng. University of Michigan. Ann Arbor, MI. (2021)

78. Cheng, R., Wiley, N., Short, M., Liu, X. & Taub, A. Applying ultrasonic vibration during single-point and two-point incremental sheet forming. Procedia Manuf. 34, 186–192 (2019).

79. Website: olympus-ims.com/en/metrology/surface-roughness-measurement-portal/evaluating-parameters/

80. Siu, K. W., Ngan, A. H. W. & Jones, I. P. New insight on acoustoplasticity – Ultrasonic irradiation enhances subgrain formation during deformation. Int. J. Plast. 27, 788–800 (2011).

81. Lum, I. et al. Effects of superimposed ultrasound on deformation of gold. J. Appl. Phys. (2009)

82. Bansal, A., Lingam, R., Yadav, S. K. & Venkata Reddy, N. Prediction of forming forces in single point incremental forming. J. Manuf. Process. 28, 486–493 (2017).

83. Isidore, B. L., Hussain, G., Shamchi, S. P., & Khan, W. A. (2016). Prediction and control of pillow defect in single point incremental forming using numerical simulations. J. Mech. Sci. Tech., 30(5), 2151-2161.

84. Shin, J. et al. Prediction of Negative Bulge in Two Point Incremental Forming of an Asymmetric Shape Part. J. Phys. Conf. Ser. 1063, (2018).

85. Cheng, R., Bansal, A., Kang, J., Liu, X. & Taub, A. The Effect of Ultrasonic Vibration on Material Movement in Incremental Sheet Forming. in 383–394 (2021). doi:10.1007/978-3-030-75381-8_32.

86. Shin, J. Investigation of Incremental Sheet Forming (ISF) using Advanced Numerical and Analytical Approaches. Ph.D. dissertation. Dept. Mech. Eng. University of Michigan. Ann Arbor, MI. (2021)

87. Kim, S. H., Ryu, J. H., Kim, K. H. & Lee, D. N. The evolution of shear deformation texture and grain refinement in asymmetrically rolled aluminum sheets. Mater. Sci. Res. Int. 8, 20–25 (2002).

88. Choi, C. H., Kim, K. H. & Lee, D. N. The effect of shear texture development on the formability in rolled aluminum alloy sheets. Mater. Sci. Forum 273–275, 391–396 (1998).

89. Karthik, V. et al. Finite element analysis of spherical indentation to study pile-up/sink-in phenomena in steels and experimental validation. Int. J. Mech. Sci. 54, 74–83 (2012).

90. Liu, Y. et al. Combined numerical simulation and nanoindentation for determining mechanical properties of single crystal copper at mesoscale. J. Mech. Phys. Solids 53, 2718–2741 (2005).

91. Kværndrup, F. B. *et al.* Area determination with pile-up and sink-in in nanoindentation of oxygen containing titanium. *Mater. Today Commun.* 30, (2022).

92. ASTM B55-7. Tension Testing Wrought and Cast Aluminum- and Magnesium-Alloy Products

93. Hill, R. A theory of the yielding and plastic flow of anisotropic metals. Amer. J. Math vol. 67 (1924).

94. Nasri, W., Gavrus, A., Kouadri-david, A. & Sai, K. Experimental and numerical study concerning the anisotropic behavior of an AA2024-T351 thick sheet using the unified formalism , a multi-mechanism model and a polycrystalline approach Abstract : (2015).

95. Holmes, J., Das, R., Stachurski, Z., Compston, P. & Kalyanasundaram, S. Development of an S-specimen geometry for shear testing of woven thermoplastic composites. Compos. Part B Eng. 203, 108485 (2020).